ANL-HEP-PR-95-64

np Elastic Scattering Spin-Spin Correlation Parameter Measurements Between 500 and 800 MeV

III. Mixtures of C_{SS}, C_{LS}, C_{LL}, and C_{NN}

V. Carlson[a], R. Garnett[b], D. Hill, K. F. Johnson[b], D. Lopiano[c], Y. Ohashi[d], T. Shima[e], H. Spinka, R. Stanek, D. Underwood, and A. Yokosawa
Argonne National Laboratory, Argonne, Illinois 60439

M. Beddo, G. Burleson, J. A. Faucett[b] G. Kyle, and M. Rawool-Sullivan[f]
New Mexico State University, Las Cruces, New Mexico 88003

H. Shimizu[g]
Tokyo Institute of Technology, Oh-Okayama, Meguro, Tokyo 152, Japan

G. Glass[h], S. Nath[b], and L. C. Northcliffe†
Texas A&M University, College Station, Texas 77843

J. J. Jarmer
Los Alamos National Laboratory, Los Alamos, New Mexico 87545

R. H. Jeppesen
University of Montana, Missoula, Montana 59801

G. E. Tripard
Washington State University, Pullman, Washington 99164

27 September 1995

Abstract

Measurements are presented for several mixtures of the spin observables C_{SS}, $C_{SL} = C_{LS}$, C_{LL}, and C_{NN} for neutron-proton elastic scattering. These data were obtained with a free polarized neutron beam, a polarized proton target, and a large magnetic spectrometer for the outgoing proton. The neutron beam kinetic energies were 484, 567, 634, 720, and 788 MeV. Combining these results with earlier measurements allows the determination of the pure spin observables C_{SS}, C_{LS}, and C_{LL} at 484, 634, and 788 MeV for c.m. angles $25° \leq \theta_{c.m.} \leq 180°$ and at 720 MeV for $35° \leq \theta_{c.m.} \leq 80°$. These data make a significant contribution to the knowledge of the isospin-0 nucleon-nucleon scattering amplitudes.

I. Introduction

In an attempt to better understand the nucleon-nucleon (NN) interaction in the intermediate energy region (up to $T_{lab} \sim 1$ GeV), polarization phenomena have been studied in great detail over the past several decades. The study of the spin dependence of the nucleon-nucleon interaction has been used to remove ambiguities among various otherwise acceptable sets of nucleon-nucleon phase shifts.

An unambiguous determination of the five isospin-one (I=1) and five isospin-zero (I=0) elastic-scattering amplitudes requires a large number of measurements of different spin parameters at each energy and scattering angle. In general, a minimum of nine observables in both the proton-proton (pp) and neutron-proton (np) systems are required to determine an unambiguous set of amplitudes above the pion production threshold. The I=1 elastic-scattering amplitudes are fairly well known to above 1 GeV from pp elastic-scattering experiments.[1-3] By contrast, the I=0 amplitudes have been

poorly known until recently. The np elastic and inelastic interaction data base has been particularly sparse above 500 MeV.[4-5] Significant numbers of np differential cross-section and polarization measurements have existed for some time, but only a few measurements of other spin observables were available until the last few years. The data described in this paper will contribute 155 new points to the existing np data base.

Phase-shift predictions of unmeasured spin observables have generally not fit the pp data very well until a model-independent amplitude (MIA) analysis of the existing data could be performed. It is likely that this will also be true for the np data. An MIA analysis is able to determine the amplitudes at angles where sufficient measurements have been made without assumptions about high partial waves and inelasticities, which are needed by the phase-shift analyses. The data discussed here are part of an ongoing program of measurements, at LAMPF and other laboratories, which should allow MIA analyses to determine the I=0 nucleon-nucleon amplitudes at several energies in the near future.

Various phase-shift predictions for measured spin parameters have indicated the possibility of resonance-like behavior in certain partial waves. This behavior has been attributed to the possible existence of dibaryon resonances. Evidence for these resonances has been seen in pp (I=1) scattering experiments.[6] The interpretation of the observed behavior of the $^1D_2$, $^3F_3$, and possibly the $^3P_2$ partial waves in pp elastic scattering seen in the various phase-shift analyses of VPI[3], Japan[2], Saclay-Geneva[1,4], and Queen Mary College[7] are clouded by the presence of the $pp \rightarrow N\Delta$ and $pp \rightarrow \pi d$ inelastic channels. It has been proposed that the opening of inelastic channels such as these may be responsible for the observed energy-dependent structures.[8-11] For this reason, a comparison between the I=1 and I=0 amplitudes should be very interesting because these inelastic channels do not contribute to the I=0 amplitudes. Because of the basic nature of the nucleon-nucleon interaction, it is important to know whether such resonances exist. This question is crucial to the further development of QCD descriptions of

the NN interaction, for example. A number of QCD inspired models predict rich resonance structures in the nucleon-nucleon channel with invariant mass above 2180 MeV/c^2.[12-15] These investigations suggest that large spin effects may occur because of the presence of dibaryon resonances, which are related to the composite, or quark, nature of the nucleon.

This paper describes the measurement of three spin-spin correlation parameters for free np elastic scattering at 484, 634, and 788 MeV beam kinetic energy. In addition, one spin-spin correlation parameter was measured at 567 and 720 MeV. The spin directions are defined as $\vec{N}$ (up) normal to the horizontal scattering plane, $\vec{L}$ (longitudinal) along the incident beam direction, and $\vec{S} = \vec{N} \times \vec{L}$ (see Fig. 1). Polarized $\vec{S}$-type and $\vec{L}$-type neutron beams were scattered from $\vec{S}$-type and $\vec{L}$-type polarized targets. The pure spin parameters determined from our measurements were C_{SS}, C_{LS}, C_{LL}, and C_{NN}, where

$$C_{ij} = \frac{\frac{d\sigma}{d\Omega}(++) + \frac{d\sigma}{d\Omega}(--) - \frac{d\sigma}{d\Omega}(+-) - \frac{d\sigma}{d\Omega}(-+)}{\frac{d\sigma}{d\Omega}(++) + \frac{d\sigma}{d\Omega}(--) + \frac{d\sigma}{d\Omega}(+-) + \frac{d\sigma}{d\Omega}(-+)}.$$

The first index refers to the beam and the second to the target polarization directions. The + and - refer to spins parallel and antiparallel, respectively, to the N, S, or L directions for the beam and target. The recoil proton was detected in a magnetic spectrometer in one of three angular ranges: θ_{lab} = 0-25°, 21-46°, or 43-76°. Interference with the polarized-target magnet coils generally prevented detection of the scattered neutron in coincidence. Measurements of C_{LL} and C_{SL} at 634 MeV and one spectrometer setting (35°) were made as a cross-check with our previously measured data.[16]

The experimental apparatus is described in Sec. II. Only modifications to the original experimental apparatus as described in previous papers will be discussed in detail (see Refs. 16-17). Two additional chambers were added to the spectrometer to improve both the resolution and track-reconstruction efficiency. The data analysis is described in Sec. III. The results and a comparison to various phase-shift and meson-exchange predictions are presented in Sec. IV. Conclusions are given in Sec. V. Preliminary results of this experiment have been presented in a short paper.[18] These measurements were also the basis of a thesis,[19] where additional details may be found. This paper contains additional measurements not previously presented in Refs. 16-19.

Recently, there has been evidence that the neutron-beam polarization was different from that believed earlier. The evidence is summarized in Sec. II, and additional calculations are presented. Revised values of spin-spin correlation parameters measured in earlier experiments with this same apparatus are also given.

II. Experimental Apparatus

These measurements were performed at the Clinton P. Anderson Meson Physics Facility in Los Alamos (LAMPF). Most of the experimental apparatus was identical to that described in our previous papers[16,17,20] with some modifications. The major differences included different readout electronics for one drift chamber (P_3), and different angles of the target polarization with respect to the beam direction.

A. The Polarized Neutron Beam

A polarized neutron beam was produced by single-charge-exchange and polarization transfer of polarized protons scattered at 0° by a liquid-deuterium target. The neutron beam entered the experimental area (Fig. 2) after passing through a 2.54-cm diameter lead and steel collimator and a 3.8-cm thick lead plug to convert γ's in the beam. The beam then passed through an intensity monitor, two spin precessing magnets (LORRAINE and CASTOR), a relative neutron polarimeter (JPAN, normally the

JPAN target was removed during data collection), and finally the polarized proton target. The beam intensity was typically a few thousand polarized neutrons per second from the $^2H(\vec{p},\vec{n})pp$ reaction.

The ratio of the neutron beam polarization to the proton beam polarization was determined previously[21-22] in this same beamline. This ratio is K_{LL} for longitudinally polarized beams and K_{NN} for transverse polarizations. More recently, a new measurement,[23] using a different experimental procedure, gave significantly different results. However, there were two minor differences in the beamline configuration used in the new K_{LL} and K_{NN} measurements and in the spin-spin correlation parameter experiments, namely collimator diameter and the use of a lead converter for γs in the beam.

The early measurements of Riley et al.[21] were performed with 800-MeV kinetic energy protons and a 5.08 cm diameter collimator. The measurements of Chalmers et al.[22] used 497, 647, and 800 MeV proton beams, and collimator diameters of 5.08, 5.08, and 2.54 cm, respectively. The neutron beam momentum spectrum at two energies is shown in Refs. 24 and 25. In both cases, the neutron beam was scattered from a liquid hydrogen target, and the recoil protons were detected in a magnetic spectrometer located at $\theta_{lab} = 30°$ (center of mass angle $\theta_{c.m.} \simeq 112°$). The measured asymmetry ε_b for opposite beam spin directions is related to K_{LL} and K_{NN} by

$$K_{jj} = \frac{\varepsilon_b}{P_p\, A_{np}},$$

where P_p is the proton beam polarization, A_{np} is the np elastic-scattering analyzing power or polarization parameter measured in other experiments, and

$$\varepsilon_b = \frac{\text{Rate}(+) - \text{Rate}(-)}{\text{Rate}(+) + \text{Rate}(-)}.$$

The results at all three proton beam energies showed that K_{LL} was much larger in magnitude than K_{NN}. With the same set of data determining A_{np} for the two measurements, the K_{LL} results of Riley[21] and Chalmers[22] at 800 MeV with the two different collimator diameters were consistent (K_{LL} = -0.640 ± 0.014 and = -0.604 ± 0.016, respectively). Figure 3a shows values of A_{np} (30° lab) found from fits with up to third order polynomials in cos $\theta_{c.m.}$ to most of the world's data[26-36] in the angular range 80° ≤ $\theta_{c.m.}$ ≤ 140°; both statistical and combined statistical and systematic errors are shown. A few sets of data with relatively large errors have been excluded.

The measurements of McNaughton et al.[23] were performed by scattering the polarized neutron beam from a second liquid deuterium target. Outgoing protons near 0° to the neutron beam direction were detected in a magnetic spectrometer. The spin of these protons was precessed in the field of the spectrometer magnet and measured in a carbon polarimeter. The collimator diameter was 5.08 cm at incident proton beam energies of 318, 497, 647, 733, and 798 MeV, and in addition was also 7.62 and 15.24 cm at 798 MeV. The values of K_{LL} were derived from

$$K_{LL}^2 = \frac{\varepsilon_b'}{P_p A_{pC} \sin\theta_p}$$

where ε_b' is the asymmetry measured in the carbon polarimeter, A_{pC} is the analyzing power for this polarimeter,[37,38] and θ_p is the angle of the outgoing proton spin precession in the spectrometer magnet. The resulting values of K_{LL} are 8 to 19% larger than measured by the earlier experiments. Also, the three values of K_{LL} from the different collimator diameters at 798 MeV were consistent (K_{LL} = -0.720 ± 0.017, -0.720 ± 0.017, and -0.719 ± 0.017 for diameters of 5.1, 7.6, and 15.2 cm, respectively).

Whereas the agreement between measurements of A_{pC} at various laboratories is good to ~ 2% over a wide range of proton energies,[23] there are differences of approximately 10-15% among various A_{np} results at many angles and beam energies. These differences are somewhat beyond quoted statistical and systematic uncertainties. In

addition, it has been suggested by Bugg,[7] based on a phase-shift analysis of np elastic-scattering data, that the measured values of ε_b/P_p by Riley et al.[21] and Chalmers et al.[22] are consistent with other results in the np data base, while the $K_{LL} = \varepsilon_b/P_p\, A_{np}$ values are inconsistent.

As noted above, one of the differences between this experiment and the recent K_{LL} measurements is the presence of a lead converter for γs in the beam. Measurements of the change in beam polarization by the presence of a 3.81-cm lead converter gave a drop in beam polarization of $(0.6 \pm 1.1\%)$.[34] As a result, no correction to our data has been made for this effect.

It is also possible that scattering of some beam neutrons from the collimator walls would result in a slight difference in the magnitude of the beam polarization at the polarized target. The only K_{LL} value measured with the same collimator diameter as in this experiment is the 800-MeV result of Chalmers et al.[22] However, this K_{LL} value is about $(6 \pm 3)\%$ smaller in magnitude than the Riley et al.[21] results which had a larger diameter collimator. Monte-Carlo studies were performed for scattering in the collimator walls, taking into account the proton beam width at the liquid deuterium target, a single elastic scattering in the collimator walls, and attenuation of the neutrons. The Monte Carlo results suggest that any difference in the beam polarization would be less than 1% given the results of the measurements by McNaughton et al.[23] with collimator diameters of 5.1 to 15.2 cm.

The adopted K_{LL} and K_{NN} values were derived as follows. The older results of Riley et al.[21] and Chalmers et al.[22] were normalized using A_{np} values from Newsom et al.[32] The Newsom measurements were acquired with a white, unpolarized neutron beam incident on a polarized proton target. It has been suggested[7,23] that the target polarization in Ref. 32 should be renormalized by a constant factor, resulting in smaller A_{np} magnitudes. The A_{np} renormalization factor was estimated by comparing the Newsom et al. data[32] to recent TRIUMF results,[33] and to new measurements at

LAMPF[34] which include the recent K_{LL} data of Ref. 23. Over the range $80° \leq \theta_{c.m.} \leq 140°$, the derived ratio to Newsom was 0.856 ± 0.006 with $\chi^2/d.f. = 1.8$. If the comparison was restricted to $\pm 8°$ of the c.m. angle corresponding to $\theta_{lab} = 30°$, which approximates the acceptance of Ref. 22, the factor becomes 0.878 ± 0.011 with $\chi^2/d.f. = 1.9$. The adopted ratio is 0.88, in agreement with the recommendation of Ref. 23.

However, it should be noted that the A_{np} renormalization factor derived in this way does not seem to be independent of energy. The ratios at ~ 425, 480, 630, and 780 MeV for $80° \leq \theta_{c.m.} \leq 140°$ are 0.914 ± 0.018, 0.884 ± 0.009, 0.831 ± 0.013, and 0.805 ± 0.011, respectively, with $\chi^2/d.f.$ ranging from 0.4 to 1.3. We do not understand this variation. Furthermore, the published Newsom et al. data seem to agree with data from Saclay.[30,31,35,36] Some of these results are from quasielastic scattering with a polarized deuteron beam while others used a free neutron beam. The pp quasielastic measurements from the same Saclay experiment agree well with free pp polarization data.

The renormalized Newsom et al. results[32] and other A_{np} data[26-31,33-36] in this energy range were then fit for $80° \leq \theta_{c.m.} \leq 140°$ as described before, and weighted by the product of the cross section and acceptance given in Ref. 22. The results are shown in Fig. 3b. The systematic uncertainty in the renormalized data for Ref. 32 was taken to be $\pm 3\%$. Two fits to these data were performed using polynomials in T_{lab}, the laboratory kinetic energy. The first fit used the data shown in Fig. 3b. The second fit used the same data except the Newsom results were unnormalized with a systematic uncertainty of $\pm 7\%$ as quoted in Ref. 32. The r.m.s. deviations per degree of freedom were 3.6 and 3.7, respectively. The adopted A_{np} values were taken from the first fit; see Table 1 and Fig. 3b. The adopted uncertainty was the computed statistical error, increased by $\sqrt{\chi^2/d.f.}$, in quadrature with the difference between the two fits.

The revised K_{LL} values from Ref. 22 are also shown in Table 1. No corrections have been applied for the combined effects of scattering in the collimator walls and the lead converter. These are expected to be small compared to the quoted uncertainties on

K_{LL} as mentioned above. Note that the revised K_{LL} values agree closely with the measurements of Ref. 23. The adopted K_{LL} values are weighted averages of data from Ref. 23 and the revised results from Ref. 22. An interpolated value is used at 581 MeV, and the measurement of Ref. 23 is assumed at 733 MeV. The ratio of K_{NN}/K_{LL} from Ref. 22 was assumed correct, and was adopted for the data in this paper. The average beam polarizations for protons and neutrons for each measurement are given in Table 2.

B. The Polarized Target

The polarized proton target (PPT) was continuously polarizing, utilizing the technique of dynamic nuclear polarization.[39] It consisted of a magnet, a ^{3}He refrigerator, a microwave system, and a nuclear magnetic resonance (NMR) system. The superconducting magnet (HERA) and refrigerator were constructed at CEN - Saclay[40-41] and were modified at LAMPF.[42]

The magnet produced a 2.5-T central field, uniform to within 0.45 mT in a sphere of 5.0 cm in diameter. In order to allow for the detection of scattered particles, the magnet provided a free, unobstructed cone of 90° opening angle with respect to the polarization direction. For nearly pure C_{LL} measurements ($C_{\lambda L}$), the magnet was positioned with the field (polarization) direction along the beam. For nearly pure C_{SL} measurements ($C_{\sigma L}$) the field was also along the beam, causing a precession of the beam spin. At a different time, the magnet was rotated at an angle of 37.5° with respect to the beam to allow measurement of a linear combination of correlation parameters, denoted by $C_{\sigma\sigma}$ ($C_{\lambda\sigma}$ for $\vec{L}$-type beam), from which C_{SS} (C_{LS}) can be derived. This was done because the coil geometry of the magnet prevented a configuration which would allow measurement of pure C_{SS} for laboratory scattering angles smaller that $\theta_{lab} = 45°$. In order to determine C_{LL} in the angular range $43° \leq \theta_{lab} \leq 76°$, the target was rotated at an angle of 25° with respect to the beam and a mixture of parameters denoted by $C_{\lambda\lambda}$ was also measured.

The HERA field precessed the spin of the incoming neutron when the field was not along the neutron's incident spin direction. Additionally, the scattering plane was rotated since the target field bends the trajectory of the outgoing recoil proton. Calculations of these effects were made for all the data presented in this paper.

The target had a diameter of 3.7 cm and a length of 5.5 cm. Two types of target material were used in the experiment. During the $C_{\lambda L}$ and $C_{\sigma L}$ data taking, the target material consisted of 85 wt. % ethylamine (C_2NH_7) and 15 wt. % borane ammonia (BH_3NH_3). The atomic composition by weight, was as follows: 45.3% carbon, 5.3% boron, 33.2% nitrogen, and 16.1% hydrogen. For the $C_{\sigma\sigma}$, $C_{\lambda\sigma}$, and $C_{\lambda\lambda}$ measurements, a similar material was used which had a larger percentage by weight of hydrogen (16.8%) and contained the following percentages of other atoms: 23.8% carbon, 4.3% boron, and 54.6% nitrogen. Both target materials were doped with Cr^V radical for polarization transfer. The materials were prepared in ~ 1-mm diameter beads in order to improve thermal contact with the ^3He bath and to improve dissipation of the heat produced from the absorbed microwave radiation. The average target polarization and the number of target polarization reversals for each of the measurements are given in Table 2.

Scattering from a carbon target was also performed at essentially every incident neutron beam kinetic energy and spectrometer setting to provide information for background subtraction, as discussed later. A study of the effective bound-nucleon polarization arising from the polarized background nuclei (^{13}C, ^{14}N, ^9B, ^{10}B) of this target material was performed.[43] It was estimated that this effect contributes negligibly to the total nucleon polarization.

C. *The Magnetic Spectrometer*

Charged particles were detected in a large acceptance (~ 100 msr) magnetic spectrometer (see Fig. 2), in which the momentum of the recoil proton was measured. Kinematical constraints, which included the recoil angle of the proton, were used to

determine the missing-mass of the scattered neutron. The momentum resolution was found to be approximately ± 1.5% at 800 MeV.

The various detectors were rigidly mounted on frames attached to the spectrometer magnet (SCM105). This made it possible to move the spectrometer as a single unit. The spectrometer magnet was moved to three positions on air pads for data taking. With respect to the beam direction, the center of the SCM105 was located at 10.0°, 35.0°, and 57.5°.

For all energies (484, 634, and 788 MeV) where the spectrometer angle was 10° or 35°, the SCM105 was operated at 2000 Amps which gave a central field integral of ~ 763 kG-cm. For data taken at a spectrometer angle of 57.5°, the magnet was operated at 1200 Amps (~ 458 kG-cm). The SCM105 magnetic field was mapped at both currents; see Refs. 16 and 44.

The detector S1 consisted of two 25.5-cm wide by 28-cm high plastic scintillators placed next to each other to produce a 51-cm wide by 28-cm high scintillator plane. A photomultiplier (PM) tube was mounted at each end of each scintillator in the vertical plane. The two signals from each scintillator were discriminated and the time-average was formed. The OR of the signals from the two S1 counters was used as the start pulse for the time-of-flight (TOF) measurements between S1 and S2.

The hodoscope S2 consisted of 25 scintillation counters, each 112-cm high, 14.0-cm wide, and 1.27-cm thick, with a PM tube mounted on the top and bottom. The center of the hodoscope was displaced horizontally by 56 cm from the SCM105 center line to compensate for the bend of the particle trajectories in the magnetic field. The time average of the top and bottom PM signals for each counter was formed, and the time relative to S1 measured. The S1-S2 relative time was corrected for cable lengths, etc., as well as the bend in the SCM105, in order to derive the TOF. A fast coincidence between S1 and the OR of the S2 counters was used for charged particle identification and as the fast trigger for the spectrometer.

Three multiwire proportional chambers (MWPC's) were used to obtain position information of a particle before it entered the spectrometer magnet. P0 was located between the trigger scintillators (S1) and the small drift chamber (P1), and it was added[17] to improve the track reconstruction efficiency of the upstream portion of the spectrometer compared to Ref. 16. P2 consisted of two chambers P2L and P2R located upstream of the SCM105 magnet, and displaced by approximately 10 cm in the direction (z) from the target to the magnet center. The frames of P2L and P2R overlapped, resulting in a dead region in the spectrometer acceptance. Operating conditions, wire spacing, and construction details were essentially identical for P0, P2L, and P2R.[16,17] The chamber efficiencies can be defined as the ratio of the reconstructable events in the chamber to the total number of analyzed events. Typical chamber efficiencies for P0 and P2 were 84% and 92%, respectively.

The P1 drift chamber, described in Ref. 16, was used upstream of the SCM105 magnet. During this experiment, this chamber had an operating efficiency of approximately 84-87%.

Two identical drift chambers P3 and P4,[20] with four planes each (X,X',U,V) and active areas 3×1 m^2, were used for particle tracking behind the SCM105 magnet. Chamber P3 was added[17] to improve the reconstruction efficiency and the momentum resolution compared to Ref. 16. The readout system for P3 consisted of the LRS 4290 Time Digitizing System operating in the Common Stop mode. Amplifier boards with 16 channels of amplification and discrimination (one TDC for each signal wire in a 16 wire group) were used. The Autotrim feature of the 4290 system was used to determine the pedestals for the TDC's. The readout system for P4 was based on the technique where the determination of which wires were hit was found from differences of propagation times along a delay line coupled to the wires.[20] For P4, each group of 16 wires was connected to a delay-line board. This limited multiplicities to one hit per 16 wires. Typical chamber efficiencies were 97% and 79-83% for P3 and P4, respectively.

A detailed study of the resolution of both P3 and P4 was conducted (see Ref. 20) using some of the 634 MeV, 35°, $C_{\lambda L}$ data. To measure the chamber resolution, a residual, $\Delta x'_j$, was calculated:

$$\Delta x'_j = x_{calc} - x = x' + (m \times s) - x,$$

where x and x' are the measured (horizontal) coordinates at the X and X' planes, s is the distance between the planes, m is the xz-slope, computed with information from P4 and P3, and j is the chamber number. The chamber resolution was obtained by converting the FWHM to a standard deviation, corrected for contributions from both the X and X' planes. This method gave calculated resolutions of ± 180 μm and ± 285 μm for P3 and P4, respectively.

D. Data Acquisition

The data acquisition was accomplished by using a CAMAC system interfaced to a PDP 11/60 computer via a microprogrammable branch driver (MBD).[45] The software to control the MBD and computer was written using the LAMPF "Q-System"[46], a general data analysis and acquisition system, based on the DEC RSX11-M operating system. A special CAMAC unit called the LAMPF trigger module (LTM) was used to signal the MBD that a certain type of event had occurred. The MBD read in a specific set of CAMAC registers, ADC's, and TDC's and transferred the data to the computer when a signal for a particular event type was received. The raw data were then written to tape. The computer was operated in the "may process" mode during data taking, giving first priority to writing the raw data to tape, and analyzed only a subset of the events. For the off-line analysis, the analyzer program was run in the "must process" mode, which required all events to be processed.

The event trigger logic was used to define and trigger LTM events. It was separated into two parts, the spin-gated run control logic (SGRC) and the EVENT 9 logic.

The SGRC logic was needed to trigger LTM EVENTS 7 and 8, as well as to monitor the status of the run and beam, and to define a number of CAMAC scaler inhibits. These signals were provided by a pair of LAMPF gate generators (LGG1, LGG2). EVENT 7 read in and cleared the CAMAC scalers at every beam spin change or at the end of a run. EVENT 8 read the target polarization every 10 seconds, as the signal was sent from the polarized target monitor/control computer. A schematic diagram of the SGRC logic is given in Fig. 4. The beam gate (BG) signal, sent from the accelerator central control room, was held true throughout the duration of each accelerator macropulse. The polarized beam gate (POL) was held "true" for polarized beam and "false" when the proton beam was in the quench mode; this signal came from the ion source. The LGG1 run gate (RG) was set true by a signal sent from the data acquisition computer at the start of a run and set false at the end. LGG2 was also reset at this time. Two additional signals, N = NOR and R = REV, were also sent from the ion source to indicate whether the polarization direction was normal (N) or reverse (R) with respect to the beam momentum. Both N and R were false when a spin change was in progress, indicated by the signal $SC = \overline{N} \bullet \overline{R} \bullet \overline{\overline{POL}}$. When the N and R signals changed, during a spin change, a noise signal was generated. A 10-sec monostable (one shot) pulse was added in order to prevent multiple EVENT 7 triggers by this noise. After being inverted several times, the N and R signals were routed to the LGG2 start and stop inputs, respectively. These states were read through a Kinetic Systems 3420 input gate and used to identify the spin state of an event and of the scalers. A logical AND of the N signal and a 10-KHz clock, and of R with the clock, were made to generate normal and reverse clock signals which were required in order to compute the beam polarization via the quench ratio method.[47] These gated clock signals were also used to determine the polarization of the beam for each read of the scalers.

A fast coincidence between one of the S1 scintillator signals and one of the S2 counter signals was defined as FTRG; see Ref. 16. The signal FTRG in coincidence with

$P = POL \bullet RG \bullet BG \bullet \overline{SC}$ from the SGRC logic was used to trigger an LTM EVENT 9. Starts for the time-to-digital converters for the P1 and P4 drift chambers and the S2 hodoscope counters, and the common stop for the P3 drift chamber electronics were also initiated with FTRG. If a signal was received from P2 (P2L or P2R), the master trigger MTRG was generated; otherwise the TDC information was cleared and the EVENT and readout aborted. Additional details and a logic diagram for the fast logic are given in Ref. 16.

A number of scalers were recorded separately for N or R beam polarization as well as quenched beam periods. These scalers were gated with either P, which corresponded to polarized beam, $Q = \overline{POL} \bullet BG \bullet RG \bullet \overline{SC}$ for quenched beam, or $I = P \bullet (\overline{\text{COMPUTER BUSY}})$ to take into account computer dead time. Scaler reads (EVENT 7) were also triggered by $\overline{RG \bullet \overline{SC}}$, which corresponded to a run terminated or suspended.

III. Data Analysis

A. *Particle Tracking*

The off-line data analysis was also performed using the LAMPF Q-system. The experiment-dependent software used for these measurements (LAMPF E-770) was a modified version of that used for LAMPF experiment E-665, which was discussed in Ref. 16. Only changes in the E-665 software to accommodate the additional chambers P0 and P3 will be discussed in this section. The MWPC P0 was added in the front close to P1, and the large drift chamber P3 was added in the rear, as discussed earlier. This allowed for additional chamber combinations which could be used to determine a track both in front of and behind the SCM105 magnet. As a result, it was not necessary for all chambers to have good position information in order for events to be reconstructed.

The minimum requirement in the software to determine the bend angle in the spectrometer was good x position information from chambers P_4, P_0 or P_1, and P_2 or P_3.

For the case when there was insufficient data from P_2 to determine the x coordinate, the two chambers in the rear were used to project to a point at the center-plane of the spectrometer magnet. This point and the coordinate(s) in either P0 and/or P1 were then used to construct a track in the front.

When there was not enough information in P3 to construct a coordinate, the tracking scheme incorporated in E-665 was used: the front chambers P0 and/or P1, and P2 were used to construct a track in the front and to project to a point at the center-plane of the magnet. This point and the coordinate in P4 were then used to construct a track in the rear. If there was "good" chamber information in all three chambers in the front, then a least-squares fit to the three points was done to determine the slopes.

Good chamber information required a unique hit reconstructed in the chamber. In the horizontal or x direction, this could mean several adjacent wires with signals in the MWPC's, with the centroids for the X and X' planes within 4 mm. At least three planes in P4 or P3 with a uniquely reconstructed position were required to be able to obtain both x and y information from these chambers. Additional details on these requirements are given in Ref. 16.

The x and y tracking were done independently in the front. This meant different chamber combinations could be used to determine the xz- and yz-slopes. The tracking scheme in the rear used wire position and drift-time information from P3 and P4 to determine a track for a given event. For the case where both P3 and P4 were "good", the information in these two chambers was sufficient to determine both the rear xz- and yz-slopes as well as the position at the midpoint of each chamber.

The algorithm used to determine the position for each plane in P3 and P4 is similar to the one described in Ref. 16. In that case, the point at the center plane of the SCM105 magnet was used to constrain the fit in P4, instead of P3. For the situation with information available from both P_3 and P_4, a maximum of four wires with signals were allowed for each plane. The proper combination of wires, one from each plane, was

chosen to be the one with the minimum r.m.s. deviation χ_{wire} from a least squares fit to a straight line. In addition, it was required that $\chi_{wire} \leq 5$ mm to eliminate fits with a wire that may have been triggered by noise. In the case that no fit satisfied the constraint on χ_{wire}, a plane was discarded, one at a time, and the fitting procedure repeated until a good χ_{wire} was obtained. Information from a plane could not be discarded if there was no data in at least one other plane of that chamber. Finally, the chosen wire combination together with the drift time for each wire, were used in another iterative fitting procedure to resolve the left-right ambiguities in each plane. For this second iteration, the r.m.s. deviation χ_{drift} was also minimized, and it was required that $\chi_{drift} \leq \sqrt{2}$ mm.

The tracks in the front and rear were used to calculate the bend angle in the spectrometer and hence the particle momentum. The $\int B_y d\ell$ for the SCM105 magnet was determined event-by-event using a table look-up parameterization of the SCM105 magnetic field which was generated by a Monte-Carlo program[16,44] that traced elastically scattered protons through the field.

With the additional allowed chamber combinations it was possible to attain a typical track reconstruction efficiency 75 - 83%, as compared to about 60 - 65% for E-665.[16] The reconstruction efficiency was calculated by taking the ratio of the number of events passing the tests above to the total number analyzed. By allowing additional chamber combinations the overall resolution of the spectrometer was also improved.

B. The Data Summary Tape (DST)

Because of the extensive computer CPU time required to decode all the raw chamber information and do the particle tracking, the data analysis was carried out in two stages. The first stage consisted of making a data summary tape (DST) from a raw data tape.

In order to make a DST, the raw chamber information was decoded and the particle tracking done. A software test was applied which required both good front and

rear tracking in addition to good TOF information. The beam and target polarizations, time-of-flight, chamber coordinates, and the front and rear slopes were then written to the DST event-by-event. No kinematic or other cuts were required to be passed in order for an event to be written to the DST, other than the χ_{wire} and χ_{drift} requirements for the P3-P4 tracking discussed earlier.

C. *Final Pass Data Analysis*

After having initially reduced the raw data to DST form, the final pass analysis was done to calculate the spin-spin correlation parameters. Cuts were applied to various kinematic and other quantities. The cuts were varied and the analysis repeated.

Using the "Q" test package, software tests were set up to allow binning of the data by both c.m. scattering angle and spin orientation of the target and beam. Figure 5 shows a c.m. scattering angle distribution of the recoil protons for 634 MeV data taken with a spectrometer angle of $\theta_{lab} = 35°$. The data were binned in 5° c.m. bins. The "hole" in the distribution is caused by the overlap region of the two halves of the detector P2. The measured laboratory scattering angle was corrected for the target magnetic field effects and survey information, before the c.m. angle was calculated.

A software test which required beam and target spins to be either "parallel" (++ or --) or "antiparallel" (+- or -+) was made on the data. Histograms for events parallel or antiparallel were made for each angle bin and these were added or subtracted appropriately to calculate C_{ij}.

D. *Cuts on the Data*

Cuts were placed on various calculated quantities for the final pass data analysis. These quantities included the x- and y-target projections, the magnet center-plane matching (DXTT, DYTT), and the particle mass as determined by the TOF and momentum measurements. Chambers P0, P1, and P2 were used to obtain the target projections in the x and y directions at z corresponding to the target center. Straight lines fit to chambers upstream and downstream of the SCM105 magnet were also projected to the

center of the SCM105 magnet; the difference in projected x and y positions are DXTT and DYTT, respectively. The purpose of placing cuts on the target projections was to reject events which did not originate from the target. It was found that using a cut on the z-target projection had no effect and therefore was not used. Figure 6 shows the final cut placed on the x-target projection for 634-MeV, 35°, $C_{\lambda L}$ and $C_{\sigma L}$ data. Events outside the markers were rejected.

For the $C_{\sigma\sigma}$ and $C_{\lambda\lambda}$ data where the target was rotated with respect to the incident beam direction, the target projections were even more important. Figure 7a shows the x-target projection for the 634 MeV, $C_{\sigma\sigma}$ data, for a 35° spectrometer angle. Events originating from the magnet coils and cryostat can easily be picked out as the smaller peak on the right side of the large peak near x = 0. The final cuts which were used are also shown.

For the case of a rotated target and a 10° spectrometer angle (Fig. 7b) the x-target projection looked somewhat different. Rather than having events which originated from the magnet coils (or cryostat) clearly separated from those originating in the target, the distribution was continuous with a long tail on the large-x side of the peak. Furthermore, because the angular acceptance of the spectrometer at θ_{lab} = 10° was so large, the unscattered portion of the beam went through the spectrometer and also contributed to the tail of the x-target projection distribution.

Figure 8 gives the x-target distribution and cuts for the 634 MeV $C_{\lambda\lambda}$ data. The polarized target is rotated 25° from L-type, and the spectrometer angle is 57.5°.

In order to separate the desired events from those originating from the magnet coils and cryostat, a pair of two-dimensional histograms were used. Figure 9 shows one of these two-dimensional histograms where the x-target projection is plotted against the x-position in P1. It can be seen that there is a large band of uncorrelated events (zero slope), which are assumed to originate from or near the target. There is also a band of events with large non-zero slope. These events were assumed to come primarily from

the unscattered part of the beam and the target cryostat. Shown in the figure are boxes which are two-dimensional cuts on the data. Events outside the boxes were rejected. A similar "box-cut" was made for the x-target projection and the P0 x-position. A logical OR between the two sets of box-cuts was required so as not to eliminate an event which missed the P0 acceptance but was reconstructed using only P1.

Cuts on the magnet center-plane matching were made in a fashion identical to that discussed for the target projections. The quantity DXTT is the difference in x of the lines fitted to chamber data in front and behind the SCM105 projected to the center of the magnet; DYTT is defined analogously for the y coordinate. Figure 10 shows the cuts on DXTT and DYTT used for the 634 MeV, $C_{\lambda\lambda}$ data with a spectrometer angle of 57.5°.

Loose cuts were placed on the particle mass as determined from the momentum and TOF. The limits for these were placed with a minimum at 500 MeV/c^2 and a maximum at 1300-1500 MeV/c^2 for all sets of data analyzed (see Fig. 14 in Ref. 16). These values were chosen so as to eliminate the deuteron background, but keep all protons (background included). Pion backgrounds were negligible, since their momentum was too low to be in the spectrometer acceptance.

E. *Calculation of the Correlation Parameters*

The spin-spin correlation parameters were calculated bin-by-bin as follows:

$$C_{ij} = \frac{1}{P_B P_T} \frac{P - \alpha A}{P + \alpha A - fC}$$

where P is the total elastic plus background counts from the sum of the pertinent runs, in the missing-mass (MM) for parallel spins, and A is the total counts for antiparallel beam and target spins. The quantity fC is the normalized carbon background described below. P_B and P_T are the average beam and target polarizations, respectively, and α is the ratio of total beam for parallel spins to the total beam for antiparallel spins from the beam intensity monitor FMON.[16]

For each 5° c.m. angle bin, the missing mass distribution for the carbon runs was compared to that for the polarized target runs. The coefficients of the linear function f(MM) were determined so that fC matched the polarized target distribution on each side of the elastic peak. After subtraction, the elastic events were clearly distinguished, and C_{ij}(MM) could be computed for each missing mass channel. The final value of C_{ij} was the weighted average over the missing mass channels in the elastic peak. Additional details may be found in Fig. 16 of Ref. 16 and the accompanying text.

The values of C_{ij} for individual runs were computed using a similar procedure. The weighted average and r.m.s. deviation χ_{run} were computed from the pertinent set of runs. Less than 1% of the total runs were rejected on the basis of large contributions to χ_{run} for several c.m. angle bins. The weighted average C_{ij} agreed to within one standard deviation with the value computed from the summed runs.

The procedure described above was used for all data in this paper with spectrometer angles of θ_{lab} = 10° and 35°. In addition to missing mass, a different quantity was also used for the $C_{\lambda\lambda}$ results at θ_{lab} = 57.5° in order to more accurately estimate the contribution from background. This quantity was $\eta = p_{lab} + A\,\theta_{lab} + B$,[17] where the momentum measured in the spectrometer is p_{lab}, and the constants A and B were chosen to make η approximately perpendicular to n + p elastic scattering kinematics in the p_{lab} - θ_{lab} plane. Histograms of η for two c.m. angle bins and for polarized target and carbon background runs are given in Fig. 11. Results for $C_{\lambda\lambda}$ were computed from the η distributions in a manner analogous to the missing mass histograms.

F. *Comparison of Background Shapes*

Quasielastic scattering from bound nucleons in the helium, boron, carbon, and nitrogen nuclei in the polarized target was a major contribution to the background observed in this experiment. In order to determine how accurately the carbon missing mass or η distribution represented the true background shape, measurements were made by using dummy targets of various materials, such as liquid nitrogen, boron

nitride, and carbon. The η distributions for the carbon measurements and two c.m. angle bins are shown in Fig. 12. Ratios of boron nitride to carbon and nitrogen to carbon are also shown; these ratios are constant near $\eta = 0$ where the np elastic events occur. To compare the various background shapes quantitatively, a chi-square test for binned data was performed between ratios of different pairs of the distributions. It was found that all the shapes agreed at the two standard deviation level. Comparisons were also made between "normal" and "reverse" distributions for each material with similar results, indicating that these nuclei were, in fact, effectively unpolarized.

Additionally, for the 484 MeV $C_{\lambda\lambda}$ data, the correlation parameters were calculated using each of these three materials as a source for the background shape. The computed values of $C_{\lambda\lambda}$ with carbon, boron nitride, and liquid nitrogen background agreed within one standard deviation at all angles. It is concluded that the carbon measurements provided an adequate representation of the background shape.

G. *Corrections for Mixed Spin Effects*

It was necessary to correct the data for the presence of undesirable spin components in both the beam and the target.

A detailed study of the neutron beam spin as measured by the relative polarimeter JPAN was performed.[16,48] Using information on the proton beam polarization direction just upstream of the liquid deuterium target, and by making polynomial fits to the magnet sweeps with JPAN to set the LORRAINE and CASTOR magnet currents, it was possible to determine the neutron beam spin components to within $\pm 3°$. The revised K_{LL} and K_{NN} values from Table 1 were used in these calculations.

For the measurements with the pure L-type polarized target, the quantities actually measured ($C_{\sigma L}$ and $C_{\lambda L}$) are linear combinations of C_{LL} and C_{SL},

$$C_{\sigma L} = AC_{LL} + BC_{SL}$$
$$C_{\lambda L} = DC_{LL} + EC_{SL} \qquad (1)$$

where $A = \cos\theta_1$, $D = \cos\theta_2$, and θ_1 and θ_2 are the angles of the beam spin with respect to the $\hat{L}$-direction for the two cases, respectively. The coefficients B and E must include additional corrections for the precession of the neutron beam spin and the rotation of the effective scattering plane because of the effects of the HERA magnetic field. Define the net rotation/precession angle as $\theta_{net} = \theta_p - \theta_R$, where θ_p is the angle of precession (in the N-S plane) of the neutron beam spin in the HERA field to the center of the polarized target, and θ_R is the scattering plane rotation angle (also in the N-S plane for the beam). Then $B = \sin\theta_1 \cos\theta_{net}$ and $E = \sin\theta_2 \cos\theta_{net}$. The angle θ_{net} was typically on the order of 10-15° and was dependent on the c.m. scattering angle. The measured values of $C_{\sigma L}$ and $C_{\lambda L}$, and the coefficients B or E (b), and A or D (e, see Eq. 2 below) are given in Table 3.

For the $C_{\sigma\sigma}$, $C_{\lambda\sigma}$, and $C_{\lambda\lambda}$ measurements, the situation was complicated further because the target was rotated with respect to the + $\hat{L}$-direction. This rotation and the effects of the HERA magnetic field caused the measured quantities $C_{\sigma\sigma}$, $C_{\lambda\sigma}$, and $C_{\lambda\lambda}$ to be linear combinations of the four pure spin-spin correlation parameters. The expression for $C_{\sigma\sigma}$ (or $C_{\lambda\sigma}$ or $C_{\lambda\lambda}$) can be written as

$$C_{\sigma\sigma} = aC_{SS} + bC_{SL} + dC_{NN} + eC_{LL} \qquad (2)$$

and

$$\begin{aligned} a &= -\sin\theta_T \cos\theta_R[-\cos\theta_R \cos\theta_p \cos\theta_T \sin(\theta_B - \theta_T) \\ &- \cos\theta_R \sin\theta_T \cos(\theta_B - \theta_T) + \sin\theta_R \sin\theta_p \sin(\theta_B - \theta_T)] \\ b &= -\sin\theta_T \cos\theta_R [-\cos\theta_p \sin\theta_T \sin(\theta_B - \theta_T) + \cos\theta_T \cos(\theta_B - \theta_T)] \\ &+ \cos\theta_T[-\cos\theta_R \cos\theta_p \cos\theta_T \sin(\theta_B - \theta_T) - \cos\theta_R \sin\theta_T \cos(\theta_B - \theta_T) \\ &+ \sin\theta_R \sin\theta_p \sin(\theta_B - \theta_T)]. \end{aligned}$$

$$d = -\sin\theta_T \sin\theta_R[-\sin\theta_R \cos\theta_p \cos\theta_T \sin(\theta_B - \theta_T)$$
$$- \sin\theta_R \sin\theta_T \cos(\theta_B - \theta_T) - \cos\theta_R \sin\theta_p \sin(\theta_B - \theta_T)]$$
$$e = \cos\theta_T[-\cos\theta_p \sin\theta_T \sin(\theta_B - \theta_T) + \cos\theta_T \cos(\theta_B - \theta_T)].$$

The subscripts on the angles are as follows: T for target rotation angle (in the target L-S plane, measured from the +L direction), R for rotation angle of the scattering plane due to HERA, p for the neutron spin precession angle, and B for the initial angle of the beam spin in the L-S plane with respect to the $\hat{L}$-direction. Table 4 gives the measured values of $C_{\sigma\sigma}$ (and $C_{\lambda\sigma}$) and the spin component admixture coefficients at three energies and for $C_{\lambda\lambda}$ at five energies. The small proton laboratory angle $C_{\sigma\sigma}$ results at 484 MeV and 634 MeV were also sorted into 30° bins in ϕ, as well as $\theta_{c.m.}$, and the results are given in Table 5.

IV. Results

The results of the spin-spin correlation measurements are presented in Figs. 13-15 as a function of the neutron c.m. scattering angle ($\theta_{c.m.}$). The error bars on the data reflect the statistical uncertainty and include an estimate of the uncertainty in the background-fitting procedure. The latter uncertainty was generally small and was estimated by comparing various background fits. The uncertainties in the beam and target polarizations were estimated to be ± 2.0% and ± 3.3%, respectively. Combination of these in quadrature gives an overall systematic error of ± 4% in the normalization of the data. This normalization uncertainty applies to each set of data in Tables 3-5. The typical uncertainty on the absolute angle is estimated to be $\delta\theta_{lab} \sim \pm 0.3°$ for all data in this paper and Refs. 16 and 17 (not $\delta\theta_{cm} \sim \pm 0.25°$ as given in Ref. 16). There are no other known angle dependent systematic errors, such as may occur in measurements of outgoing proton spin with carbon polarimeters.

Pure C_{LL} and C_{SL} values were derived from the data in Table 3. These are given in Figs. 16a and 16b. Also shown are the results from Ref. 16 corrected for the revised K_{LL} values in Table 1. Essentially all the C_{LL} and C_{SL} data agree to within two standard deviations with the earlier measurements. In addition, a weighted average was calculated for C_{SL} over the angular range $80° \leq \theta_{c.m.} \leq 125°$. For the measurements in this paper $\langle C_{SL} \rangle = + 0.002 \pm 0.027$, and for the earlier results, $\langle C_{SL} \rangle = + 0.119 \pm 0.053$. Both sets of data are consistent within two standard deviations of each other and consistent with $C_{SL} = 0$ in this angular range.

Pure C_{LL}, C_{SL}, and C_{SS} np elastic-scattering spin observables have been derived from the data in Tables 3-5 and in Refs. 16 and 17. The corrections for the revised spin transfer parameters K_{LL} and K_{NN} have been applied to the results in Refs. 16 and 17. The main changes occurred in the C_{LL} values. The results are presented in Table 6 and Figs. 17-19. Values of C_{NN} from the VPI phase shifts[3] were used to correct for the presence of this observable in some of the mixed spin observable data; the C_{NN} correction was usually very small[17] but was sizable for $155° \leq \theta_{c.m.} \leq 180°$. At angles near $\theta_{c.m.} = 180°$, values of C_{NN} could be extracted from the ϕ distributions in Table 5. These are given in Table 6 and compared to other data in Fig. 20.

Tests of consistency between various pp and np data at 90° c.m. have been suggested.[55] One such test was conducted in Ref. 16; the results suggested a possible problem with the normalization of C_{LL}. This test was based on the relation:[55]

$$C_{LL}(np) = 1/2[1 - C_{NN}(np)] + 1/8\,[C_{NN}(pp) - 1 + 2\,C_{LL}(pp)]\,\frac{d\sigma / d\Omega(pp)}{d\sigma / d\Omega(np)}\,. \qquad (3)$$

Experimental values for the differential cross sections, $C_{NN}(pp)$, $C_{LL}(pp)$, and $C_{NN}(np)$ were taken from the literature; see Table V in Ref. 16. This test has been repeated with the revised data of Ref. 16 plus the new measurements reported in this paper. The

results are given in Table 7, and there is now satisfactory agreement. A similar relation was derived for C_{SS}:[55]

$$C_{SS}(np) = 1/2[1 - C_{NN}(np)] + 1/8\,[3\,C_{NN}(pp) - 3 - 2\,C_{LL}(pp)]\,\frac{d\sigma / d\Omega(pp)}{d\sigma / d\Omega(np)}\,. \qquad (4)$$

A comparison using this relation is also given in Table 7, and again there is good agreement.

The pure C_{LS}, C_{LL} and C_{NN} np elastic-scattering results are compared to other measurements in Figs. 18-20. Quasielastic-scattering data with polarized deuteron beams and polarized proton targets at 744 and 794 MeV[31] equivalent kinetic energy, and free np elastic-scattering measurements at 800 MeV[52] are compared to the 720 and 788 MeV C_{LS} data from this experiment in Fig. 18. The agreement is quite good, except at 788 MeV near 60° c.m., where the Saclay data are closer to zero. Free np C_{LL} measurements at 630 MeV[53] and 800 MeV[52] are shown in Fig. 19; the Saclay results agree with the data from this paper. Finally, LAMPF C_{NN} data at 465 and 665 MeV[54] are shown in Fig. 20. The two sets of experimental results appear consistent in the angular regions where they overlap.

Values of the mixed spin-spin parameters are compared to some phase-shift analysis (PSA) predictions in Figs. 13-15. The Kyoto[2] and Saclay-Geneva[4] (and Queen Mary College [7,50]) analyses contained some preliminary results from Ref. 16 and this experiment in their data bases, but with an incorrect beam polarization as discussed before. The Virginia Polytechnic Institute (VPI) PSA[49] includes all the results of this paper in its data base, and there is quite good agreement with the measured values. The other two sets of predictions and the differences between them in Figs. 13-15 illustrate the magnitude of the uncertainties in the phase-shift solutions when the new data from this paper and from Refs. 23, 34-36, 52 and 56 are not included.

The final pure spin-spin observables are similarly compared to the recent VPI[49] and Queen Mary College[7,50] phase-shift analysis predictions in Figs. 17-20. The meson-exchange model predictions of Lee et al.[51] are also shown in these figures. It can be seen that all three give a fair representation of the data, except for the Lee et al. predictions for C_{NN}. Table 8 contains the reduced chi-squared (χ^2/d.f.) value at each energy for these predictions compared to the pure spin-spin observables in this paper. The values of χ^2/d.f. are typically 2-3 at 484, 634, and 788 MeV. None of the PSA solutions or models has the best prediction at all energies.

Values of pure I = 0 and of interference between I = 0 and I = 1 quantities for C_{SS}, C_{LS}, and C_{LL} can be obtained using expressions in Ref. 55:

$$(C_{\alpha\alpha}\, d\sigma/d\Omega)_{I=0} = 2(C_{\alpha\alpha}\, d\sigma/d\Omega)_{np}(\theta) + 2(C_{\alpha\alpha}\, d\sigma/d\Omega)_{np}(\pi-\theta) - (C_{\alpha\alpha}\, d\sigma/d\Omega)_{pp}(\theta)$$

$$(C_{LS}\, d\sigma/d\Omega)_{I=0} = 2(C_{LS}\, d\sigma/d\Omega)_{np}(\theta) - 2(C_{LS}\, d\sigma/d\Omega)_{np}(\pi-\theta) - (C_{LS}\, d\sigma/d\Omega)_{pp}(\theta)$$

$$(C_{\alpha\alpha}\, d\sigma/d\Omega)_{Int} = 2(C_{\alpha\alpha}\, d\sigma/d\Omega)_{np}(\theta) - 2(C_{\alpha\alpha}\, d\sigma/d\Omega)_{np}(\pi-\theta)$$

$$(C_{LS}\, d\sigma/d\Omega)_{Int} = 2(C_{LS}\, d\sigma/d\Omega)_{np}(\theta) + 2(C_{LS}\, d\sigma/d\Omega)_{np}(\pi-\theta),$$

with α = L or S. The experimental values of these quantities, using recent VPI PSA[49] values for the pp observables and for $(d\sigma/d\Omega)$np, are shown in Figs. 21-23. PSA predictions of the VPI,[49] Kyoto,[2] and Saclay-Geneva[4] groups are shown for comparison; the VPI predictions seem to fit best. These quantities are important for a model-independent amplitude determination, as described in Ref. 55.

The experimental results for C_{LL}, C_{SS}, and C_{NN} from this paper and from other groups, plus the np elastic-scattering differential cross sections, can be used to estimate $\Delta\sigma_L$ (np, elastic) and $\Delta\sigma_T$ (np, elastic). The quantity $\Delta\sigma_L$ (elastic) is the elastic scattering contribution to the total cross-section difference between antiparallel and parallel longitudinal spin states for a polarized beam incident on a polarized target. Similarly, $\Delta\sigma_T$ (elastic) is the elastic total cross-section difference for transversely polarized beam and target. These quantities can be obtained from:

$$\Delta\sigma_L(\text{elastic}) \equiv \sigma_{el}\left(\rightleftarrows\right) - \sigma_{el}\left(\rightrightarrows\right) = -\int (2\,C_{LL})\,\frac{d\sigma}{d\Omega}\,d\Omega$$

$$\Delta\sigma_T(\text{elastic}) \equiv \sigma_{el}\left(\uparrow\downarrow\right) - \sigma_{el}\left(\uparrow\uparrow\right) = -\int (C_{SS} + C_{NN})\,\frac{d\sigma}{d\Omega}\,d\Omega. \qquad (5)$$

Unfortunately, the data do not extend over the full angular range. A numerical integration for $\Delta\sigma_L$(np, elastic) using np differential cross sections from the recent Arndt et al.[49] PSA solution, and C_{LL} results from Table 6 and from Ref. 52 at 800 MeV was performed. The results and the c.m. angular region are given in Table 9. Similarly, for $\Delta\sigma_T$ (np, elastic), the same differential cross sections were used and the C_{SS} results were taken from Table 6. The values of C_{NN} at 484 and 634 MeV were obtained from Table 6 and from Ref. 54 (465, 665 MeV). At 788 MeV, the C_{NN} data of Nath et al. [57] and of Ball et al.[58] were used. The computed values of $\Delta\sigma_T$ (np, elastic) and the c.m. angular range are also included in Table 9.

The data for C_{LL} $d\sigma/d\Omega$, C_{NN} $d\sigma/d\Omega$, and C_{SS} $d\sigma/d\Omega$ were fit with Legendre polynomials in order to estimate the integrals in Eq. 5 over the full c.m. angular range. However, the fits gave unphysical results $\left(|C_{ij}| > 1\right)$ at small angles in many cases. As a result, these quantities were estimated at 0° from PSA predictions,[2,4,49,50] and the 0° values (see Table 9) were added to the measured data set for the fits. The uncertainties in the 0° results were estimated from the spread in the PSA predictions. The revised fits

did not exceed $d\sigma/d\Omega$ in magnitude, and the values of $\Delta\sigma_L$ (np, elastic) and $\Delta\sigma_T$ (np, elastic) derived from these fits are presented in Table 9 and Fig. 24. Measured values of $\Delta\sigma_L$ (np, total) and $\Delta\sigma_T$ (np, total)[59-63] and predictions of the VPI PSA[49] are also given in Fig. 24 for comparison.

The I = 0 quantities $\Delta\sigma_L$ (I = 0, elastic) and $\Delta\sigma_T$ (I = 0, elastic) can be determined from:

$$\Delta\sigma_L \text{ (I = 0, elastic)} = 2\ \Delta\sigma_L \text{ (np, elastic)} - \Delta\sigma_L \text{ (pp, elastic)}$$

and similarly for $\Delta\sigma_T$. The pp quantities were obtained from the VPI PSA.[49] The results are listed in Table 9 and shown in Fig. 25, along with experimental values of $\Delta\sigma_L$ (I = 0, total) and $\Delta\sigma_T$ (I = 0, total) from Refs. 59-63. It can be seen that the I = 0 elastic and total results are equal within errors, except perhaps at 788 MeV. This is expected since the inelastic I = 0 cross section is small at these energies.

Finally, there is a rapid change in C_{NN}, C_{SS} and C_{LL} at $\theta_{c.m.} \simeq$ 150-180°, caused by an interference of the one pion exchange amplitudes[64] with other amplitudes. For example, C_{LL} goes from large positive values near 150° to large negative values near 180°, crossing zero at a 4-momentum transfer squared $u \simeq -1.5\ m_\pi^2 \approx -0.03\ GeV^2/c^2$. Pure one pion exchange amplitudes would give $C_{SS} = 0 = C_{NN} = C_{LL} = C_{LS} = P$, which is not observed in the data. Models at higher energy, such as those of Chia[65] and Berger et al.[66], predict large negative C_{LL} near 180° but do not reproduce C_{NN} or C_{SS}. The model of Chia has also been compared to other np spin observables in Ref. 67, where good agreement is observed for some and poor agreement for other observables.

V. Conclusions

New experimental results are presented for the np elastic-scattering spin observables C_{LL}, C_{LS}, and C_{SS} at 484, 634, 720, and 788 MeV (Figs. 17-19 and Table 6), for C_{NN} at 484 and 634 MeV (Fig. 20 and Table 6), and for a mixture of spin observables at 567

MeV (Fig. 15 and Table 4). Corrections have been applied for revised neutron beam polarizations for these data and earlier measurements using the same apparatus. In addition, values for pure I = 0 and for interference of I = 0 and I = 1 spin parameters C_{SS}, C_{LS}, and C_{LL} have been derived at 484, 634, and 788 MeV (Figs. 21-23), as well as the elastic total cross-section differences $\Delta\sigma_L$ (np, elastic), $\Delta\sigma_T$ (np, elastic), $\Delta\sigma_L$ (I = 0, elastic) and $\Delta\sigma_T$ (I = 0, elastic) (Figs. 24 and 25 and Table 9). When combined with other recent data from LAMPF and SATURNE II, and expected results from PSI, it is anticipated that knowledge of the I = 0 nucleon-nucleon amplitudes will be greatly improved compared to several years ago.

ACKNOWLEDGMENTS

We gratefully acknowledge L. Rosen and the LAMPF staff for assistance with all aspects of this experiment. In particular, we thank D. Hagerman, O. van Dyck, M. McNaughton, K. Jones, and the operations staff for help with the polarized proton beam; J. Novak, N. Hoffman and the cryogenics staff for assistance with the LD_2 target, superconducting solenoid, and helium liquifier; L. Agnew, R. Werbeck, J. Gomez, and the experimental facilities staff for help with construction and operation of the experimental apparatus; G. Gonzales, G. Suazo, and the machine shop staff for assistance with construction of detector and magnet supports; R. Harrison, J. Cordova, and E. Weiler for surveying the apparatus; J. Harrison, T. Kozlowski, M. Oothoudt, and the staff of the LAMPF Data Analysis Center for assistance with on-line and off-line computing; W. Haberichter and A. Rask for help with the MWPC's; F. Montoya and A. Rask for assistance with the scintillation counters; T. Hunter for help with mapping the SCM-105 magnetic field; R. Sena, R. Richardson, and the LEEP staff for assistance with repairs of various electronic components and modules; N. Hill, L. Kocenko, A. Rask, and J. Tobin for mechanical design and construction of the large drift chambers; and J. Dawson,

L. Chan, and C. Leonard for design and construction of some of the drift chamber read-out electronics. We are especially indebted to R. Damjanovich for help with many aspects of the mechanical design of the experimental apparatus; T. Kasprzyk, J. Vaninetti, J. Estes, W. Coulter, K. Graham, and D. Yeamans for assistance with the polarized target operation; M. McNaughton for help with measurements of the beam spin components and polarization; and R. Arndt, D. Bugg, N. Hoshizaki, T.S.H. Lee, F. Lehar and I. Strakovsky for information of their phase shift analysis results and model predictions. This experiment was supported in part by the U.S. Department of Energy, Contracts W-31-109-ENG-38 and DE-AS05-76ER-04449 and Grants DE-FG05-88ER-40399 and DE-FG04-88ER-40403, and by Associated Western Universities. R. Garnett, R. Jeppesen, M. Rawool-Sullivan, and G. Tripard express gratitude to the Argonne Division of Educational Programs for support during a part of this research.

References

† Deceased.

(a) Present address:

(b) Present address: AOT Division, Los Alamos National Laboratory, Los Alamos, New Mexico 87545.

(c) Present address: 2482 Forrest Drive, Woodridge, IL 60517.

(d) Present address: Japan Synchrotron Radiation Research Institute, Ako, Hyogo 678-12, Japan.

(e) Present address: Kyoto Academy of International Culture, 24 Kamihato-Chyo, Kitashirakawa, Sakyo-ku, Kyoto, Japan.

(f) Present address: NIS Division, Los Alamos National Laboratory, Los Alamos, New Mexico 87545.

(g) Present address: Department of Physics, Yamagata University, Yamagata, Japan.

(h) Present address: 3218C Walnut, Los Alamos, New Mexico 87544-2060.

1) J. Bystricky, C. Lechanoine-Leluc , and F. Lehar, J. Phys. (Paris) 51, 2747 (1990).

2) Y. Higuchi, N. Hoshizaki, H. Masuda, and H. Nakao, Prog. Theor. Phys. 86, 17 (1991); N. Hoshizaki and T. Watanabe, ibid. 86, 321 (1991); 86, 327 (1991).

3) R. A. Arndt, L. D. Roper, R. L. Workman, and M. W. McNaughton, Phys. Rev. D45, 3995 (1992).

4) J. Bystricky, C. Lechanoine-Leluc, and F. Lehar, J. Phys. (Paris) 48, 199 (1987); C. Lechanoine-Leluc, F. Lehar, P. Winternitz, and J. Bystricky, *ibid.* 48, 985 (1987).

5) R. A. Arndt, Phys. Rev. D37, 2665 (1988).

6) For example, M. P. Locher, M. E. Sainio, and A. Svarc, Adv. Nucl. Phys. 17, 47 (1986); A. Yokosawa, J. Phys. Soc. Jpn. Suppl. 55, 251 (1986).

7) D. V. Bugg, Phys. Rev. C41, 2708 (1990).

8) D. V. Bugg, J. Phys. G5, 1349 (1979).

9) C. E. Waltham, R. Shypit, D. A. Axen, F. Entezami, M. Comyn, D. Healey, G. A. Ludgate, G. D. Wait, D. V. Bugg, J. A. Edgington, and N. R. Stevenson, Nucl. Phys. A433, 649 (1985).

10) A. B. Wicklund, M. W. Arenton, D. S. Ayres, R. Diebold, E. N. May, L. J. Nodulman, J. R. Sauer, E. C. Swallow, M. M. Calkin, M. D. Corcoran, J. Hoftiezer, H. E. Miettinen, and G. S. Mutchler, Phys. Rev. D35, 2670 (1987).

11) R. L. Shypit, D. V. Bugg, D. M. Lee, M. W. McNaughton, R. R. Silbar, N. M. Stewart, A. S. Clough, C. L. Hollas, K. H. McNaughton, P. Riley, and C. A. Davis, Phys. Rev. Lett. 60, 901 (1988); 61, 2385 (1988); R. L. Shypit, D. V. Bugg, A. H. Sanjari, D. M. Lee, M. W. McNaughton, R. R. Silbar, C. L. Hollas, K. H. McNaughton, P. Riley and C. A. Davis, Phys. Rev. C40, 2203 (1989).

12) P. J. G. Mulders, A. Th. M. Aerts, and J. J. deSwart, Phys. Rev. Lett. 40, 1543 (1978); A. Th. M. Aerts, P. J. G. Mulders, and J. J. deSwart, Phys. Rev. D17, 260 (1978).

13) E. L. Lomon in Proceedings of the Tenth International Conference on Particles and Nuclei, Heidelberg, Germany, 1984, edited by B. Povh and G. Zu Putlitz, [Nucl. Phys. A434, 139C (1985)].

14) T. Goldman, K. Maltman, G. J. Stephenson, K. E. Schmidt, and F. Wang, Phys. Rev. C39, 1889 (1989).

15) N. Konno, H. Nakamura, and H. Noya, Phys. Rev. D35, 239 (1987).

16) W. R. Ditzler, D. Hill, J. Hoftiezer, K. F. Johnson, D. Lopiano, T. Shima, H. Shimizu, H. Spinka, R. Stanek, D. Underwood, R. G. Wagner, A. Yokosawa, G. R. Burleson, J. A. Faucett, C. A. Fontenla, R. W. Garnett, C. Luchini, M. W. Rawool-Sullivan, T. S. Bhatia, G. Glass, J. C. Hiebert, R. A. Kenefick, S. Nath, L. C. Northcliffe, R. Damjanovich, J. J. Jarmer, J. Vaninetti, R. H. Jeppesen, and G. E. Tripard, Phys. Rev. D46, 2792 (1992).

17) T. Shima, D. Hill, K. F. Johnson, H. Shimizu, H. Spinka, R. Stanek, D. Underwood, A. Yokosawa, G. Glass, J. C. Hiebert, R. A .Kenefick, S. Nath, L. C. Northcliffe, G. R. Burleson, R. W. Garnett, J. A. Faucett, M. W. Rawool-Sullivan, R. Damjanovich, J. J. Jarmer, R. H. Jeppesen, and G. E. Tripard, Phys. Rev. D47, 29 (1993).

18) R. Garnett, M. Rawool, V. Carlson, D. Hill, K. F. Johnson, D. Lopiano, Y. Ohashi, T. Shima, H. Spinka, R. Stanek. D. Underwood, A. Yokosawa, M. Beddo, G. Burleson, J. A. Faucett, G. Kyle, H. Shimizu, G. Glass, S. Nath, L. C. Northcliffe, J. J. Jarmer, R. H. Jeppesen, and G. E. Tripard, Phys. Rev. D40, 1708 (1989).

19) R. W. Garnett, thesis, New Mexico State University, 1988 and Los Alamos National Laboratory Report No. LA-11491-T (1989), unpublished.

20) W. Haberichter, T. Kasprzyk, H. Shimizu, H. Spinka, R. Stanek, G. Burleson, R. Garnett, and J. Tobin, Nucl. Instrum. Methods in Phys. Res. A270, 361 (1988).

21) P. J. Riley, C. L. Hollas, C. R. Newsom, R. D. Ransome, B. E. Bonner, J. E. Simmons, T. S. Bhatia, G. Glass, J. C. Hiebert, L. C. Northcliffe, and W. B. Tippens, Phys. Lett. 103B, 313 (1981).

22) J. S. Chalmers, W. R. Ditzler, T. Shima, H. Shimizu, H. Spinka, R. Stanek, D. Underwood, R. Wagner, A. Yokosawa, J. E. Simmons, G. Burleson, C. Fontenla, T. S. Bhatia, G. Glass, and L. C. Northcliffe, Phys. Lett. 153B, 235 (1985).

23) M. W. McNaughton, K. Koch, I. Supek, N. Tanaka, K. H. McNaughton, P. J. Riley, D. A. Ambrose, J. D. Johnson, A. Smith, G. Glass, J. C. Hiebert, L. C. Northcliffe, A. J. Simon, D. L. Adams, R. D. Ransome, D. B. Clayton, H. M. Spinka, R. H. Jeppesen, and G. E. Tripard, Phys. Rev. C44, 2267 (1991); M. W. McNaughton, K. Koch, I. Supek, N. Tanaka, D. A. Ambrose, P. Coffey, K. Johnston, K. H. McNaughton, P. J. Riley, G. Glass, J. C. Hiebert, L. C. Northcliffe, A. J. Simon, D. J. Mercer, D. L. Adams, H. Spinka, R. H. Jeppesen, G. E. Tripard, and H. Woolverton, *ibid.* 45, 2564 (1992).

24) C. W. Bjork, P. J. Riley, B. E. Bonner, J. E. Simmons, K. D. Williamson, M. L. Evans, G. Glass, J. C. Hiebert, M. Jain, R. A. Kenefick, L. C. Northcliffe, C. G. Cassapakis, H. C. Bryant, B. D. Dieterle, C. P. Leavitt, D. M. Wolfe, and D. W. Werren, Phys. Lett. 63B, 31 (1976).

25) C. W. Bjork, thesis, University of Texas at Austin, 1975, and Los Alamos National Laboratory Report LA-6192-T (unpublished).

26) D. Cheng, B. MacDonald, J. A. Helland, and P. M. Ogden, Phys. Rev. 163, 1470 (1967).

27) A. S. Clough, D. R. Gibson, D. Axen, R. Dubois, L. Felawka, R. Keeler, G. A. Ludgate, C. J. Oram, C. Amsler, D. V. Bugg, J. A. Edgington, L. P. Robertson, N. M. Stewart, J. Beveridge, and J. R. Richardson, Phys. Rev. C21, 988 (1980).

28) The A_{np} data were collected in the same experiment described in Ref. 54. Numerical values were obtained from the data base of Arndt et al. in Ref. 49.

29) M. Sakuda, S. Isagawa, S. Ishimoto, S. Kabe, A. Masaike, K. Morimoto, K. Ogawa, M. Suetake, F. Takasaki, Y. Watase, N. Kim, S. Kobayashi, A. Murakami, A. deLesquen, K. Nakajima, S. Nakada, T. Wada, and I. Yamauchi, Phys. Rev. D25, 2004 (1982).

30) J. Ball, V. Ghazikhanian, J. Gordon, F. Lehar, A. de Lesquen, F. Perrot, and L. van Rossum, Nucl. Phys. B286, 635 (1987).

31) A. de Lesquen, F. Lehar, L. van Rossum, P. Chaumette, J. Derégel, J. Fabre, J. M. Fontaine, F. Perrot, P. Bach, R. Hess, Ph. Sormani, J. Ball, C. D. Lac, D. Adams, J. Bystricky, V. Ghazikhanian, and C. A. Whitten, Nucl. Phys. B304, 673 (1988).

32) C. R. Newsom, C. L. Hollas, R. D. Ransome, P. J. Riley, B. E. Bonner, J. G. J. Boissevain, J. J. Jarmer, M. W. McNaughton, J. E. Simmons, T. S. Bhatia, G. Glass, J. C. Hiebert, L. C. Northcliffe, and W. B. Tippens, Phys. Rev. C39, 965 (1989).

33) D. Bandyopadhyay, R. Abegg, M. Ahmad, J. Birchall, K. Chantziantoniou, C. A. Davis, N. E. Davison, P. P. J. Delheij, P. W. Green, L. G. Greeniaus, D. C. Healey, C. Lapointe, W. J. McDonald, C. A. Miller, G. A. Moss, S. A. Page, W. D. Ramsay, N. L. Rodning, G. Roy, W. T. H. van Oers, G. D. Wait, J. W. Watson, and Y. Ye, Phys. Rev. C40, 2684 (1989).

34) M. W. McNaughton, K. Johnston, D. R. Swenson, D. Tupa, R. L. York, D. A. Ambrose, P. Coffey, K. H. McNaughton, P. J. Riley, G. Glass, J. C. Hiebert, R. H. Jeppesen, H. Spinka, I. Supek, G. E. Tripard, and H. Woolverton, Phys. Rev. C48, 256 (1993).

35) J. Ball, Ph. Chesny, M. Combet, J. M. Fontaine, R. Kunne, M. C. Lemaire, J. L. Sans, J. Bystricky, C. D. Lac, F. Lehar, A. de Lesquen, M. de Mali, F. Perrot-Kunne, L. van Rossum, P. Bach, Ph. Demiérre, G. Gaillard, R. Hess, D. Rapin, Ph. Sormani, J. P. Goudour, R. Binz, A. Klett, E. Rössle, H. Schmitt, L. S. Barabash, Z. Janout, B. A. Khachaturov, Yu. A. Usov, D. Lopiano, and H. Spinka, Nucl. Phys. A559, 477 (1993).

36) J. Ball, Ph. Chesny, M. Combet, J. M. Fontaine, C. D. Lac, J. L. Sans, J. Bystricky, F. Lehar, A. de Lesquen, M. de Mali, F. Perrot-Kunne, L. van Rossum, A. Ahmidouch, P. Bach, Ph. Demiérre, G. Gaillard, R. Hess, R. Kunne, D. Rapin, Ph. Sormani, J. P. Goudour, R. Binz, A. Klett, E. Rössle, H. Schmitt, D. Lopiano, and H. Spinka, Nucl. Phys. A559, 489 (1993).

37) R. D. Ransome, C. L. Hollas, P. J. Riley, B. E. Bonner, W. D. Cornelius, O. B. van Dyck, E. W. Hoffman, W. M. McNaughton, R. L. York, S. A. Wood, and K. Toshioka, Nucl. Instrum. Meth. 201, 315 (1982).

38) M. W. McNaughton, B. E. Bonner, H. Ohnuma, O. B. van Dyck, S. Tsu-Hsun, C. L. Hollas, D. J. Cremans, K. H. McNaughton, P. J. Riley, R. F. Rodebaugh, S.-W. Xu, S. E. Turpin, B. Aas, and G. S. Weston, Nucl. Instrum. Meth. A241, 435 (1985).

39) A. Abragam and M. Goldman, Nuclear Magnetism: Order and Disorder, Clarendon Press, Oxford (1982); Rep. Prog. Phys. 41, 395 (1978).

40) P. Autones, J. C. Brisson, A. Boucherie, G. Cozzika, J. Deregel, J. P. Duthil, H. Desportes, Y. Ducros, A. Katz, A. de Lesquen, J. P. Merlo, J. F. Mougel, J. Movchet, J. C. Raoul, B. Tsai, L. van Rossum, B. Amblard, J. M. Fontaine, M. Hansroul, and J. M. Rieubland, Nucl. Instrum. Methods 103, 211 (1972).

41) J. C. Raoul, P. Autones, R. Auzolle, C. Bruneton, J. Bystricky, G. Cozzika, J. Deregel, Y. Ducros, A. Gaidot, A. Katz, F. Khantine-Langlois, F. Lehar, A. de Lesquen, J. P. Merlo, S. Miyashita, J. Movchet, J. Pierrard, M. Ramadier, P. Roubeau, G. Souchère, L. van Rossum, A. A. Derevschikov, N. I. Golovnya, Yu. S. Khoderev, Yu. A. Matulenko, A. P. Meschanin, S. B. Nurushev, A. I. Saraykin, V. S. Seleznev, V. V. Siskin, E. V. Smirnov, V. L. Solovyanov, V. N. Zapolsky, Yu. M. Kazarinov, M. Yu. Kazarinov, B. A. Khatchaturov, I. K. Potashnikova, and V. P. Kanavets, Nucl. Instrum. Methods 125, 585 (1975).

42) I. P. Auer, W. R. Ditzler, D. Hill, K. Imai, H. Spinka, R. Stanek, K. Toshioka, D. Underwood, R. Wagner, A. Yokosawa, E. W. Hoffman, J. J. Jarmer, G. R. Burleson, W. B. Cottingame, S. J. Greene, and S. Stuart, Phys. Rev. D29, 2435 (1984).

43) D. Hill and H. Spinka, unpublished note in Ref. 19.

44) R. W. Garnett and G. R. Burleson, Nucl. Instrum. Methods A313, 501 (1992).

45) L. R. Biswell and R. E. Rajala, Los Alamos National Laboratory report LA-4916-MS (1972), unpublished.

46) J. F. Harrison, T. Kozlowski, R. A. Floyd, J. F. Amann, G. T. Anderson, M. A. Oothoudt, and D. G. Perry, IEEE Trans. Nucl. Sci. NS-28, 3724 (1981); D. G. Perry, IEEE Trans. Nucl. Sci. NS-26, 4494 (1979); and M. Kellogg, M. M. Minor, S. Shlaer, N. Spencer, R. F. Thomas, and H. van der Beken, Los Alamos National Laboratory report LA-7001-M, 1978 (unpublished).

47) M. W. McNaughton, P. R. Bevington, H. B. Willard, E. Winkelmann, E. P. Chamberlin, F. H. Cverna, N. S. P. King, and H. Willmes, Phys. Rev. C23, 1128 (1981).

48) H. Spinka, Argonne National Laboratory report ANL-HEP-TR-88-14, 1988 (unpublished).

49) The PSA predictions were obtained by the SAID computer program by R. A. Arndt et al., available at Virginia Polytechnic Institute and State University. The SP95 solutions are used in the plots. Note that the spin observable A_{zx} calculated in the SAID program is $-C_{LS} = -C_{SL}$ as defined in this paper.

50) M. McNaughton and D. V. Bugg, private communication.

51) T. S. H. Lee (private communication) and M. Betz and T.-S. H. Lee, Phys. Rev. C23, 375 (1981); T.-S. H. Lee, Phys. Rev. Lett. 50, 1571 (1983); Phys. Rev. C29, 195 (1984); T.-S. H. Lee and A. Matsuyama, Phys. Rev. C32, 1986 (1985); 36, 1459 (1987).

52) J. Ball, Ph. Chesny, M. Combet, J. M. Fontaine, C. D. Lac, J. L. Sans, J. Bystricky, F. Lehar, A. de Lesquen, M. de Mali, F. Perrot-Kunne, L. van Rossum, P. Bach. Ph. Demierre, G. Gaillard, R. Hess, R. Kunne, D. Rapin, Ph. Sormani, J. P. Goudour, R. Binz, A. Klett, R. Peschina-Klett, E. Rössle, and H. Schmitt, Nucl. Phys. A574, 697 (1994).

53) J. Ball, C. D. Lac, F. Lehar, A. de Lesquen, L. van Rossum, P. Chaumette, J. Derégel, J. Fabre, M. de Mali, J. M. Fontaine, F. Perrot, P. Bach, G. Gaillard, R. Hess, D. Rapin, Ph. Sormani, V. Ghazikhanian, C. A. Whitten, R. Peschina, and E. Rössle, Z. Phys. C40, 193 (1988).

54) T. S. Bhatia, G. Glass, J. C. Hiebert, L. C. Northcliffe, W. B. Tippens, B. E. Bonner, J. E. Simmons, C. L. Hollas, C. R. Newsom, R. D. Ramsome, and P. J. Riley, in Polarization Phenomena in Nuclear Physics - 1980 (Fifth International Symposium, Santa Fe) Proceedings of the Fifth International Sympoisum on Polarization Phenomena in Nuclear Physics, edited by G. G. Ohlsen, R. E. Brown, N. Jarmie, M. W. McNaughton, and G. M. Hale, AIP Conf. Proc. No. 69 (AIP, New York, 1981), p. 123. Numerical values were obtained from the SAID data base, Ref. 3.

55) H. Spinka, Phys. Rev. D30, 1461 (1984).

56) K. H. McNaughton, D. A. Ambrose, P. Coffey, K. Johnston, P. J. Riley, M. W. McNaughton, K. Koch, I. Supek, N. Tanaka, G. Glass, J. C. Hiebert, L. C. Northcliffe, A. J. Simon, D. J. Mercer, D. L. Adams, H. Spinka, R. H. Jeppesen, G. E. Tripard, and H. Woolverton, Phys. Rev. C46, 47 (1992).

57) S. Nath, G. Glass, J. C. Hiebert, J. A. Holt, R. A. Kenefick, L. C. Northcliffe, D. P. Grosnick, D. Lopiano, Y. Ohashi, T. Shima, H. M. Spinka, R. Stanek, T. S. Bhatia, J. J. Jarmer, P. J. Riley, S. Sen, J. A. Faucett, G. Kyle, R. H. Jeppesen, and G. E. Tripard, Phys. Rev. D39, 3520 (1989).

58) J. Ball, Ph. Chesny, M. Combet, J. M. Fontaine, C. D. Lac, M. C. Lemaire, J. L. Sans, J. Bystricky, F. Lehar, A. de Lesquen, M. de Mali, F. Perrot-Kunne, L. van Rossum, P. Bach, Ph. Demierre, G. Gaillard, R. Hess, R. Kunne, D. Rapin, Ph. Sormani, B. Vuaridel, J. P. Goudour, R. Binz, A. Klett, E. Rössle, H. Schmitt, L. S. Barabash, Z. Janout, B. A. Khachaturov, Yu. A. Usov, D. Lopiano, and H. Spinka, Nucl. Phys. A559, 511 (1993).

59) F. Lehar, A. de Lesquen, L. van Rossum, P. Chaumette, J. Derégel, J. Fabre, M. de Mali, J. M. Fontaine, D. Legrand, F. Perrot, J. Ball, C. D. Lac, P. Bach, G. Gaillard, R. Hess, Ph. Sormani, V. Ghazikhanian, C. A. Whitten, R. Peschina, and E. Rössle, Phys. Lett. B189, 241 (1987).

60) J. M. Fontaine, F. Perrot-Kunne, J. Bystricky, F. Lehar, A. de Lesquen, M. de Mali, L. van Rossum, J. Ball, Ph. Chesny, C. D. Lac, J. L. Sans, J. P. Goudour, P. Bach, G. Gaillard, R. Hess, R. Kunne, D. Rapin, Ph. Sormani, R. Binz, A. Klett, R. Peschina, E. Rössle, and H. Schmitt, Nucl. Phys. B358, 297 (1991).

61) R. Binz, B. van den Brandt, R. Büchle, M. Daum, Ph. Demierre, J. Franz, G. Gaillard, N. Hamann, R. Hess, J. A. Konter, F. Lehar, C. Lechanoine-Leluc, S. Mango, R. Peschina, F. Perrot-Kunne, D. Rapin, E. Rössle, P. A. Schmelzbach, H. Schmitt, and R. Todenhagen, Nucl. Phys. A533, 601 (1991).

62) J. Ball, L. S. Barabash, R. Binz, J. Bystricky, Ph. Chesny, M. Combet, Ph. Demierre, J. M. Fontaine, G. Gaillard, R. Hess, Z. Janout, B. A. Khachaturov, A. Klett, R. Kunne, F. Lehar, M. C. Lemaire, A. de Lesquen, D. Lopiano, M de Mali, F. Perrot-Kunne, D. Rapin, E. Rössle, J. L. Sans, H. Schmitt, H. Spinka, and Yu. A. Usov, Z. Phys. C61, 53 (1994).

63) M. Beddo, G. Burleson, J. A. Faucett, S. Gardiner, G. Kyle, R. Garnett, D. Grosnick, D. Hill, K. Johnson, D. Lopiano, Y. Ohashi, T. Shima, H. Spinka, R. Stanek, D. Underwood, A. Yokosawa, G. Glass, R. Kenefick, S. Nath, L. Northcliffe, J. J. Jarmer, S. Penttilä, R. Jeppesen, G. Tripard, M. Devereux, and P. Kroll, Phys. Rev. D50, 104 (1994).

64) A. Scotti, and D. Y. Wong, Phys. Rev. 138, B145 (1965).

65) S.-P. Chia, Phys. Rev. D5, 2316 (1972); D7, 1496 (1973); D15, 290 (1977).

66) E. L. Berger, A. C. Irving, and C. Sorensen, Phys. Rev. D17, 2971 (1978).

67) R. D. Ransome, C. L. Hollas, P. J. Riley, B. E. Bonner, W. R. Gibbs, M. W. McNaughton, J. E. Simmons, T. S. Bhatia, G. Glass, J. C. Hiebert, L. C. Northcliffe, and W. B. Tippens, Phys. Rev. Lett. 48, 781 (1982).

TABLE 1

Summary of the input data to compute the adopted values of the spin transfer parameters K_{LL}. The data of Ref. 22 are revised as described in the text. The adopted values at $T_{n,lab}$ = 484, 634, and 788 MeV are weighted averages of Ref. 23 and revised Ref. 22 data. The K_{LL} at 567 MeV is an interpolation of the McNaughton et al. measurements.

$T_{n,lab}$	$T_{p,lab}$	$\langle A_{np} \rangle_{New}$	$\langle A_{np} \rangle_{Ref.\ 22}$	Revised K_{LL} (Ref. 22)	K_{LL} (Ref. 23)	Adopted K_{LL}
484 MeV	497 MeV	-0.270 ± 0.007	-0.316	-0.584 ± 0.019	-0.579 ± 0.011	-0.580 ± 0.010
567 MeV	580 MeV				(-0.643)	-0.643
634 MeV	647 MeV	-0.357 ± 0.014	-0.407	-0.725 ± 0.030	-0.686 ± 0.012	-0.691 ± 0.011
720 MeV	733 MeV				-0.717 ± 0.013	-0.717 ± 0.013
788 MeV	800 MeV	-0.283 ± 0.010	-0.325	-0.693 ± 0.030	-0.720 ± 0.017	-0.713 ± 0.015

TABLE 2

Summary of average proton and neutron beam polarizations, $< P_{B,p} >$ and $<P_{B,n}>$, average target polarization $<P_T>$, number of polarized and background runs and target spin reversals for each spin observable, spectrometer angle, and beam kinetic energy $T_{n,lab}$.

Spin Observable	Spectrometer Angle	Tn,lab MeV	$< P_{B,p} >$	$<P_{B,n}>$	$<P_T>$	# Reversals	# Runs	# Background Runs
$C_{\sigma\sigma}$	10°	484	0.700	0.406	0.707	13	39	17
$C_{\sigma\sigma}$	10°	634	0.747	0.510	0.728	13	46	22
$C_{\sigma\sigma}$	10°	788	0.803	0.537	0.710	6	29	14
$C_{\lambda L}$	35°	634	0.741	0.506	0.692	12	38	15
$C_{\sigma L}$	35°	634	0.709	0.484	0.685	5	19	
$C_{\lambda\sigma}$	35°	484	0.796	0.429	0.708	7	21	17
$C_{\sigma\sigma}$	35°	484	0.751	0.414	0.713	15	47	
$C_{\sigma\sigma}$	35°	634	0.744	0.508	0.724	14	45	15
$C_{\sigma\sigma}$	35°	788	0.826	0.552	0.716	13	48	14
$C_{\lambda\lambda}$	57.5°	484	0.734	0.425	0.717	29	75	20
$C_{\lambda\lambda}$	57.5°	567	0.709	0.453	0.729	11	35	0
$C_{\lambda\lambda}$	57.5°	634	0.798	0.545	0.720	19	59	5
$C_{\lambda\lambda}$	57.5°	720	0.772	0.532	0.728	10	36	14
$C_{\lambda\lambda}$	57.5°	788	0.720	0.482	0.735	18	68	29

TABLE 3

Measured values of the quantities $C_{\sigma L}$ and $C_{\lambda L}$ with the pure L-type polarized target, a beam kinetic energy $T_{n,lab}$ = 634 MeV, and a spectrometer laboratory angle of 35° . The minimum, maximum, and average value of $\theta_{c.m.}$ for each bin are shown in the first three columns. The coefficients of $C_{SL} = C_{LS}$ and C_{LL} are given in the last two columns, respectively, from Eq. 2 in the text.

Kinetic Energy = 634 MeV

θ_{min}	θ_{max}	$\langle\theta_{cm}\rangle$	C_{ij}	ΔC_{ij}	b	e
122.5	127.5	124.4	-0.159	0.221	-0.9463	0.1930
117.5	122.5	120.0	-0.120	0.127	-0.9467	0.1930
112.5	117.5	115.0	-0.124	0.128	-0.9458	0.1930
107.5	112.5	110.0	-0.009	0.183	-0.9515	0.1930
102.5	107.5	105.1	0.183	0.150	-0.9498	0.1930
97.5	102.5	100.2	0.301	0.602	-0.9519	0.1930
92.5	97.5	94.9	0.195	0.145	-0.9551	0.1930
87.5	92.5	90.1	-0.048	0.158	-0.9585	0.1930
82.5	87.5	85.0	0.010	0.142	-0.9595	0.1930
77.5	82.5	80.3	-0.042	0.211	-0.9626	0.1930
122.5	127.5	124.4	0.873	0.263	0.1195	0.9920
117.5	122.5	120.0	0.157	0.234	0.1196	0.9920
112.5	117.5	115.0	0.359	0.200	0.1195	0.9920
107.5	112.5	110.0	0.500	0.251	0.1202	0.9920
102.5	107.5	105.1	0.470	0.206	0.1200	0.9920
97.5	102.5	100.2	0.293	0.480	0.1202	0.9920
92.5	97.5	94.9	0.789	0.235	0.1207	0.9920
87.5	92.5	90.1	0.154	0.240	0.1211	0.9920
82.5	87.5	85.0	0.427	0.265	0.1212	0.9920
77.5	82.5	80.3	1.056	0.324	0.1216	0.9920
122.5	127.5	124.4	0.771	0.126	0.0592	0.9980
117.5	122.5	120.0	0.742	0.089	0.0592	0.9980
112.5	117.5	115.0	0.649	0.092	0.0592	0.9980
107.5	112.5	110.0	0.559	0.110	0.0595	0.9980
102.5	107.5	105.1	0.701	0.090	0.0594	0.9980
97.5	102.5	100.2	0.274	0.214	0.0595	0.9980
92.5	97.5	94.9	0.602	0.101	0.0597	0.9980
87.5	92.5	90.1	0.528	0.098	0.0600	0.9980
82.5	87.5	85.0	0.454	0.106	0.0600	0.9980
77.5	82.5	80.3	0.048	0.173	0.0602	0.9980

TABLE 4

Measured values of the spin-spin observables $C_{\sigma\sigma}$, $C_{\lambda\sigma}$, and $C_{\lambda\lambda}$ at various spectrometer angles and neutron beam kinetic energies. The minimum, maximum, and average value of $\theta_{c.m.}$ for each bin are shown in the first three columns. The coefficients a, b, d, and e of the pure observables C_{SS}, $C_{LS} = C_{SL}$, C_{NN}, and C_{LL}, respectively, are given in the last four columns; see Eq. 2 in the text.

Kinetic Energy = 484 MeV

θ_{min}	θ_{max}	$\langle\theta_{cm}\rangle$	C_{ij}	ΔC_{ij}	a	b	d	e
177.5	180.0	178.4	-0.492	0.083	0.1011	-0.2915	0.4322	0.1801
172.5	177.5	174.7	-0.470	0.054	0.0008	-0.0630	0.5325	0.1801
167.5	172.5	169.8	-0.490	0.066	0.0677	-0.2300	0.4655	0.1801
162.5	167.5	165.0	-0.371	0.048	0.1169	-0.3181	0.4164	0.1801
157.5	162.5	160.3	-0.206	0.045	0.1333	-0.3444	0.4000	0.1801
152.5	157.5	154.9	-0.110	0.101	0.3225	-0.5937	0.2107	0.1801
147.5	152.5	149.9	-0.038	0.079	0.4714	-0.7601	0.0619	0.1801
142.5	147.5	145.1	0.051	0.077	0.4714	-0.7601	0.0619	0.1801
137.5	142.5	140.1	-0.007	0.047	0.4893	-0.7804	0.0440	0.1801
132.5	137.5	135.2	-0.028	0.072	0.4966	-0.7888	0.0367	0.1801
127.5	132.5	130.9	0.182	0.174	0.4751	-0.7643	0.0582	0.1801
122.5	127.5	124.9	0.649	0.201	0.0846	-0.7011	-0.0043	0.7703
117.5	122.5	120.1	0.474	0.163	0.0858	-0.7024	-0.0055	0.7703
112.5	117.5	115.1	0.558	0.127	0.0842	-0.7006	-0.0039	0.7703
107.5	112.5	110.1	0.486	0.142	0.0826	-0.6987	-0.0023	0.7703
102.5	107.5	105.8	0.387	0.162	0.0848	-0.7013	-0.0045	0.7703
97.5	102.5	99.3	0.298	0.346	0.0759	-0.6896	0.0045	0.7703
92.5	97.5	95.0	0.130	0.108	0.0769	-0.6912	0.0034	0.7703
87.5	92.5	90.0	0.229	0.133	0.0759	-0.6896	0.0045	0.7703
82.5	87.5	85.0	0.285	0.118	0.0748	-0.6880	0.0056	0.7703
77.5	82.5	80.1	0.167	0.109	0.0741	-0.6870	0.0063	0.7703
72.5	77.5	75.9	0.539	0.134	0.0763	-0.6903	0.0041	0.7703
122.5	127.5	124.9	0.067	0.063	0.5225	-0.8249	0.0102	0.1872
117.5	122.5	120.1	0.040	0.065	0.5193	-0.8210	0.0134	0.1872
112.5	117.5	115.1	0.025	0.062	0.5235	-0.8262	0.0092	0.1872
107.5	112.5	110.1	-0.086	0.079	0.5275	-0.8312	0.0052	0.1872
102.5	107.5	105.8	-0.239	0.104	0.5219	-0.8243	0.0107	0.1872
97.5	102.5	99.3	-0.077	0.102	0.5414	-0.8497	-0.0088	0.1872
92.5	97.5	95.0	-0.181	0.079	0.5395	-0.8470	-0.0068	0.1872

Kinetic Energy = 484 MeV (Continued)

θ_{min}	θ_{max}	$\langle\theta_{cm}\rangle$	C_{ij}	ΔC_{ij}	a	b	d	e
87.5	92.5	90.0	-0.055	0.068	0.5414	-0.8497	-0.0088	0.1872
82.5	87.5	85.0	0.021	0.074	0.5433	-0.8523	-0.0107	0.1872
77.5	82.5	80.1	0.039	0.070	0.5444	-0.8539	-0.0117	0.1872
72.5	77.5	75.9	-0.028	0.119	0.5407	-0.8486	-0.0080	0.1872
77.5	82.5	78.9	0.209	0.065	0.0040	-0.4197	0.0116	0.8936
72.5	77.5	75.0	0.140	0.055	0.0050	-0.4227	0.0107	0.8936
67.5	72.5	70.1	0.118	0.050	0.0049	-0.4223	0.0108	0.8936
62.5	67.5	65.1	0.126	0.046	0.0036	-0.4185	0.0120	0.8936
57.5	62.5	60.5	0.111	0.063	0.0025	-0.4150	0.0131	0.8936
52.5	57.5	54.6	-0.013	0.075	-0.0046	-0.3888	0.0203	0.8936
47.5	52.5	50.1	-0.063	0.060	-0.0067	-0.3801	0.0223	0.8936
42.5	47.5	45.3	-0.034	0.103	-0.0096	-0.3663	0.0253	0.8936
37.5	42.5	40.6	0.067	0.219	-0.0134	-0.3462	0.0291	0.8936

Kinetic Energy = 567 MeV

θ_{min}	θ_{max}	$\langle\theta_{cm}\rangle$	C_{ij}	ΔC_{ij}	a	b	d	e
77.5	82.5	78.8	0.314	0.117	-0.0142	-0.3797	0.0117	0.8927
72.5	77.5	75.0	0.191	0.064	-0.0132	-0.3832	0.0106	0.8927
67.5	72.5	70.1	0.216	0.060	-0.0129	-0.3839	0.0104	0.8927
62.5	67.5	65.2	0.075	0.057	-0.0138	-0.3813	0.0112	0.8927
57.5	62.5	60.6	0.023	0.094	-0.0145	-0.3789	0.0120	0.8927
52.5	57.5	54.5	0.064	0.119	-0.0208	-0.3558	0.0182	0.8927
47.5	52.5	50.1	0.074	0.084	-0.0223	-0.3489	0.0198	0.8927
42.5	47.5	45.3	-0.327	0.104	-0.0251	-0.3359	0.0225	0.8927
37.5	42.5	40.4	-0.491	0.202	-0.0280	-0.3196	0.0255	0.8927

Kinetic Energy = 634 MeV

θ_{min}	θ_{max}	$\langle\theta_{cm}\rangle$	C_{ij}	ΔC_{ij}	a	b	d	e
177.5	180.0	178.5	-0.469	0.181	0.4272	-0.7429	0.1200	0.2134
172.5	177.5	174.7	-0.511	0.065	0.0916	-0.2986	0.4557	0.2134
167.5	172.5	169.9	-0.505	0.059	0.1072	-0.3272	0.4400	0.2134
162.5	167.5	165.0	-0.353	0.054	0.1841	-0.4491	0.3632	0.2134
157.5	162.5	160.5	-0.171	0.063	0.2117	-0.4877	0.3356	0.2134
152.5	157.5	154.9	-0.004	0.135	0.3603	-0.6693	0.1869	0.2134

Kinetic Energy = 634 MeV (continued)

θ_{min}	θ_{max}	$\langle\theta_{cm}\rangle$	C_{ij}	ΔC_{ij}	a	b	d	e
147.5	152.5	149.9	-0.048	0.113	0.5065	-0.8290	0.0408	0.2134
142.5	147.5	145.3	0.108	0.105	0.4838	-0.8040	0.0635	0.2134
137.5	142.5	140.2	0.063	0.084	0.5077	-0.8304	0.0395	0.2134
132.5	137.5	135.2	-0.002	0.130	0.5178	-0.8417	0.0295	0.2134
127.5	132.5	128.5	-0.111	0.481	0.5469	-0.8765	0.0004	0.2134
122.5	127.5	124.9	-0.052	0.064	0.5401	-0.8680	0.0071	0.2134
117.5	122.5	120.0	-0.199	0.080	0.5389	-0.8664	0.0084	0.2134
112.5	117.5	115.1	-0.233	0.073	0.5406	-0.8685	0.0067	0.2134
107.5	112.5	110.0	-0.185	0.075	0.5450	-0.8741	0.0023	0.2134
102.5	107.5	105.5	-0.169	0.084	0.5410	-0.8690	0.0063	0.2134
97.5	102.5	99.2	-0.116	0.136	0.5530	-0.8847	-0.0057	0.2134
92.5	97.5	94.9	-0.054	0.084	0.5527	-0.8843	-0.0054	0.2134
87.5	92.5	90.0	0.076	0.066	0.5536	-0.8856	-0.0064	0.2134
82.5	87.5	85.0	0.177	0.065	0.5551	-0.8877	-0.0078	0.2134
77.5	82.5	80.0	0.098	0.060	0.5562	-0.8893	-0.0089	0.2134
72.5	77.5	75.6	0.101	0.085	0.5545	-0.8868	-0.0072	0.2134
77.5	82.5	78.6	0.194	0.099	-0.0134	-0.3819	0.0113	0.8927
72.5	77.5	75.0	0.222	0.053	-0.0125	-0.3849	0.0103	0.8927
67.5	72.5	70.0	0.140	0.050	-0.0114	-0.3882	0.0092	0.8927
62.5	67.5	65.1	0.193	0.053	-0.0120	-0.3864	0.0099	0.8927
57.5	62.5	60.6	0.090	0.069	-0.0127	-0.3842	0.0106	0.8927
52.5	57.5	54.5	0.156	0.094	-0.0187	-0.3631	0.0166	0.8927
47.5	52.5	50.1	0.052	0.055	-0.0209	-0.3542	0.0188	0.8927
42.5	47.5	45.2	-0.037	0.068	-0.0240	-0.3400	0.0219	0.8927
37.5	42.5	40.3	0.086	0.082	-0.0273	-0.3218	0.0252	0.8927
32.5	37.5	35.7	0.079	0.211	-0.0306	-0.3001	0.0285	0.8927

Kinetic Energy = 720 MeV

θ_{min}	θ_{max}	$\langle\theta_{cm}\rangle$	C_{ij}	ΔC_{ij}	a	b	d	e
77.5	82.5	78.5	0.233	0.259	0.0046	-0.4237	0.0089	0.8963
72.5	77.5	74.9	0.356	0.126	0.0049	-0.4248	0.0086	0.8963
67.5	72.5	70.0	0.242	0.081	0.0056	-0.4267	0.0079	0.8963
62.5	67.5	65.0	0.086	0.062	0.0051	-0.4254	0.0084	0.8963
57.5	62.5	60.4	-0.070	0.092	0.0040	-0.4220	0.0095	0.8963
52.5	57.5	54.5	-0.021	0.144	-0.0003	-0.4071	0.0139	0.8963
47.5	52.5	50.0	-0.186	0.086	-0.0022	-0.4002	0.0157	0.8963
42.5	47.5	45.2	-0.082	0.093	-0.0046	-0.3903	0.0181	0.8963
37.5	42.5	40.3	-0.269	0.104	-0.0075	-0.3769	0.0211	0.8963
32.5	37.5	35.5	-0.038	0.238	-0.0108	-0.3599	0.0243	0.8963

Kinetic Energy = 788 MeV

θ_{min}	θ_{max}	$\langle\theta_{cm}\rangle$	C_{ij}	ΔC_{ij}	a	b	d	e
177.5	180.0	178.2	-0.464	0.145	0.5630	-0.8604	0.0007	0.1650
172.5	177.5	174.8	-0.517	0.110	0.3479	-0.6299	0.2158	0.1650
167.5	172.5	170.0	-0.563	0.117	0.0593	-0.2172	0.5044	0.1650
162.5	167.5	165.0	-0.249	0.088	0.1646	-0.4018	0.3991	0.1650
157.5	162.5	160.6	0.024	0.112	0.2467	-0.5121	0.3170	0.1650
152.5	157.5	154.7	0.036	0.179	0.4717	-0.7607	0.0920	0.1650
147.5	152.5	150.0	0.142	0.095	0.5338	-0.8262	0.0299	0.1650
142.5	147.5	145.3	0.298	0.197	0.5052	-0.7956	0.0585	0.1650
137.5	142.5	140.2	0.267	0.165	0.5365	-0.8292	0.0272	0.1650
132.5	137.5	135.2	0.267	0.147	0.5428	-0.8362	0.0209	0.1650
127.5	132.5	130.4	-0.173	0.144	0.5428	-0.8362	0.0209	0.1650
122.5	127.5	126.1	-0.041	0.228	0.5316	-0.8238	0.0321	0.1650
122.5	127.5	124.8	-0.056	0.089	0.5595	-0.8558	0.0043	0.1650
117.5	122.5	120.1	-0.008	0.103	0.5571	-0.8530	0.0066	0.1650
112.5	117.5	115.1	0.013	0.084	0.5598	-0.8563	0.0039	0.1650
107.5	112.5	109.8	0.086	0.099	0.5660	-0.8643	-0.0023	0.1650
102.5	107.5	105.2	0.028	0.108	0.5620	-0.8591	0.0017	0.1650
97.5	102.5	100.4	0.157	0.180	0.5567	-0.8525	0.0070	0.1650
92.5	97.5	94.7	0.084	0.137	0.5686	-0.8679	-0.0049	0.1650
87.5	92.5	90.0	0.011	0.096	0.5675	-0.8663	-0.0038	0.1650
82.5	87.5	84.9	0.138	0.118	0.5678	-0.8667	-0.0041	0.1650
77.5	82.5	80.0	0.045	0.088	0.5705	-0.8706	-0.0068	0.1650
72.5	77.5	75.2	0.165	0.097	0.5707	-0.8710	-0.0070	0.1650
77.5	82.5	78.1	-0.200	0.326	-0.0082	-0.3963	0.0086	0.8954
72.5	77.5	74.8	0.242	0.088	-0.0086	-0.3949	0.0090	0.8954
67.5	72.5	70.0	0.141	0.089	-0.0076	-0.3980	0.0080	0.8954
62.5	67.5	65.0	0.108	0.061	-0.0076	-0.3980	0.0080	0.8954
57.5	62.5	60.1	0.008	0.062	-0.0085	-0.3953	0.0089	0.8954
52.5	57.5	55.4	0.020	0.105	-0.0099	-0.3907	0.0104	0.8954
47.5	52.5	49.8	-0.039	0.063	-0.0142	-0.3753	0.0147	0.8954
42.5	47.5	45.2	-0.156	0.070	-0.0162	-0.3674	0.0166	0.8954
37.5	42.5	40.3	-0.180	0.120	-0.0191	-0.3540	0.0195	0.8954
32.5	37.5	35.4	-0.025	0.135	-0.0220	-0.3387	0.0224	0.8954
27.5	32.5	30.8	0.057	0.194	-0.0245	-0.3228	0.0250	0.8954

TABLE 5

Measured values of the spin-spin observable $C_{\sigma\sigma}$ at small laboratory angles and $T_{n,lab}$ = 484, 634 MeV. Each set of data corresponds to a single value in Table 4. However, these data are binned in azimuthal angle ϕ. The minimum, maximum, and average values of $\theta_{c.m.}$ for each point are given in the first three columns. The coefficients a, b, d, and e of the pure spin observables C_{SS}, $C_{LS} = C_{SL}$, C_{NN}, and C_{LL}, respectively are given in the last four columns; see Eq. 2 in the text. There were insufficient data at 788 MeV to determine ϕ distributions at these c.m. angles.

Kinetic Energy = 484 MeV

θ_{min}	θ_{max}	$\langle\theta_{cm}\rangle$	C_{ij}	ΔC_{ij}	a	b	d	e
177.5	180.0	178.4	-0.416	0.258	0.3963	0.8281	0.1370	0.1801
177.5	180.0	178.4	-0.413	0.268	0.1006	0.5421	0.4327	0.1801
177.5	180.0	178.4	-0.031	0.229	-0.0291	0.1108	0.5624	0.1801
177.5	180.0	178.4	-0.311	0.211	0.1370	-0.3502	0.3963	0.1801
177.5	180.0	178.4	-0.544	0.301	0.4327	-0.7173	0.1006	0.1801
172.5	177.5	174.7	-0.605	0.156	0.3963	0.8281	0.1370	0.1801
172.5	177.5	174.7	-0.506	0.101	0.1006	0.5421	0.4327	0.1801
172.5	177.5	174.7	-0.369	0.088	-0.0291	0.1108	0.5624	0.1801
172.5	177.5	174.7	-0.389	0.087	0.1370	-0.3502	0.3963	0.1801
172.5	177.5	174.7	-0.494	0.083	0.4327	-0.7173	0.1006	0.1801
167.5	172.5	169.8	-0.404	0.145	0.1006	0.5421	0.4327	0.1801
167.5	172.5	169.8	-0.360	0.070	-0.0291	0.1108	0.5624	0.1801
167.5	172.5	169.8	-0.512	0.066	0.1370	-0.3502	0.3963	0.1801
167.5	172.5	169.8	-0.723	0.075	0.4327	-0.7173	0.1006	0.1801
167.5	172.5	169.8	-0.619	0.162	0.5624	-0.8992	-0.0291	0.1801
162.5	167.5	165.0	-0.155	0.171	0.1006	0.5421	0.4327	0.1801
162.5	167.5	165.0	-0.258	0.069	-0.0291	0.1108	0.5624	0.1801
162.5	167.5	165.0	-0.309	0.067	0.1370	-0.3502	0.3963	0.1801
162.5	167.5	165.0	-0.446	0.066	0.4327	-0.7173	0.1006	0.1801
162.5	167.5	165.0	-0.447	0.142	0.5624	-0.8992	-0.0291	0.1801
157.5	162.5	160.3	-0.099	0.323	0.1006	0.5421	0.4327	0.1801
157.5	162.5	160.3	-0.059	0.101	-0.0291	0.1108	0.5624	0.1801
157.5	162.5	160.3	-0.151	0.071	0.1370	-0.3502	0.3963	0.1801
157.5	162.5	160.3	-0.243	0.070	0.4327	-0.7173	0.1006	0.1801
157.5	162.5	160.3	-0.498	0.191	0.5624	-0.8992	-0.0291	0.1801
152.5	157.5	154.9	-0.182	0.111	0.1370	-0.3502	0.3963	0.1801
152.5	157.5	154.9	-0.174	0.121	0.4327	-0.7173	0.1006	0.1801
152.5	157.5	154.9	0.011	0.169	0.5624	-0.8922	-0.0291	0.1801

Kinetic Energy = 634 MeV

θ_{min}	θ_{max}	$\langle\theta_{cm}\rangle$	C_{ij}	ΔC_{ij}	a	b	d	e
177.5	180.0	178.5	-0.051	0.248	0.5631	0.9179	-0.0158	0.2134
177.5	180.0	178.5	-0.407	0.205	0.3786	0.8137	0.1686	0.2134
177.5	180.0	178.5	0.025	0.313	0.0892	0.4914	0.4581	0.2134
177.5	180.0	178.5	-0.711	0.230	-0.0158	0.0374	0.5631	0.2134
177.5	180.0	178.5	-0.154	0.280	0.1686	-0.4266	0.3786	0.2134
177.5	180.0	178.5	-0.245	0.319	0.4581	-0.7763	0.0892	0.2134
177.5	180.0	178.5	-0.922	0.334	0.5631	-0.9179	-0.0158	0.2134
177.5	180.0	178.5	-0.330	0.330	0.3786	-0.8137	0.1686	0.2134
177.5	180.0	178.5	-0.519	0.436	0.0892	-0.4914	0.4581	0.2134
177.5	180.0	178.5	-0.621	0.388	-0.0158	-0.0374	0.5631	0.2134
177.5	180.0	178.5	-0.568	0.381	0.1686	0.4266	0.3786	0.2134
177.5	180.0	178.5	-0.318	0.245	0.4581	0.7763	0.0892	0.2134
172.5	177.5	174.7	-0.769	0.249	0.3786	0.8137	0.1686	0.2134
172.5	177.5	174.7	-0.426	0.101	0.0892	0.4914	0.4581	0.2134
172.5	177.5	174.7	-0.299	0.124	-0.0158	0.0374	0.5631	0.2134
172.5	177.5	174.7	-0.337	0.122	0.1686	-0.4266	0.3786	0.2134
172.5	177.5	174.7	-0.594	0.127	0.4581	-0.7763	0.0892	0.2134
172.5	177.5	174.7	-0.694	0.135	0.5631	-0.9179	-0.0158	0.2134
172.5	177.5	174.7	-0.687	0.376	0.3786	-0.8137	0.1686	0.2134
167.5	172.5	169.9	-0.082	0.101	0.0892	0.4914	0.4581	0.2134
167.5	172.5	169.9	-0.492	0.091	-0.0158	0.0374	0.5631	0.2134
167.5	172.5	169.9	-0.515	0.103	0.1686	-0.4266	0.3786	0.2134
167.5	172.5	169.9	-0.622	0.109	0.4581	-0.7763	0.0892	0.2134
167.5	172.5	169.9	-0.749	0.124	0.5631	-0.9179	-0.0158	0.2134
162.5	167.5	165.0	-0.246	0.157	0.0892	0.4914	0.4581	0.2134
162.5	167.5	165.0	-0.239	0.105	-0.0158	0.0374	0.5631	0.2134
162.5	167.5	165.0	-0.366	0.105	0.1686	-0.4266	0.3786	0.2134
162.5	167.5	165.0	-0.355	0.100	0.4581	-0.7763	0.0892	0.2134
162.5	167.5	165.0	-0.354	0.166	0.5631	-0.9179	-0.0158	0.2134
157.5	162.5	160.5	-0.339	0.149	-0.0158	0.0374	0.5631	0.2134
157.5	162.5	160.5	-0.091	0.102	0.1686	-0.4266	0.3786	0.2134
157.5	162.5	160.5	-0.212	0.101	0.4581	-0.7763	0.0892	0.2134
157.5	162.5	160.5	-0.276	0.191	0.5631	-0.9179	-0.0158	0.2134
152.5	157.5	154.9	0.008	0.123	0.1686	-0.4266	0.3786	0.2134
152.5	157.5	154.9	-0.157	0.156	0.4581	-0.7763	0.0892	0.2134
152.5	157.5	154.9	-0.061	0.247	0.5631	-0.9179	-0.0158	0.2134

TABLE 6

Final results of the pure spin parameters C_{SS}, $C_{LS} = C_{SL}$, C_{NN}, and C_{LL} from this experiment (Tables 3-5) and the data in Refs. 16, 17. Corrections to the earlier data for the revised K_{LL} values of Table 1 have been included. The measurements of C_{SS} and C_{NN} in parentheses are uncertain because of the rapid angular dependence and possible errors in the angle $\theta_{c.m.}$, and may be omitted from phase shift analyses if desired. The quoted uncertainties are statistical. In addition, the estimated systematic error from knowledge of the beam and target polarization is ± 4%. Note that in addition to these results, Table 4 contains a mixture of spin observable data at $T_{n,lab} = 567$ MeV which are not included below. The C_{NN} values quoted without errors are from a phase shift analysis of Arndt et al.[3] (FA 92) and were used to derive pure spin observables from the measured data.

Kinetic Energy = 484 MeV

θ_{MIN}	θ_{MAX}	C_{SS} ± ΔC_{SS}	C_{LS} ± ΔC_{LS}	C_{LL} ± ΔC_{LL}	C_{NN} ± ΔC_{NN}	χ^2/d.f.
177.5	180.0	----	----	-0.904 0.099	----	
172.5	177.5	(-0.903 0.180)	-0.102 0.049	-0.762 0.057	(-0.463 0.118)	19.73/25
167.5	172.5	(-1.159 0.169)	0.001 0.049	-0.755 0.041	(-0.491 0.099)	12.04/16
162.5	167.5	-0.799 0.169	-0.047 0.065	-0.456 0.051	-0.324 0.099	4.81/11
157.5	162.5	-0.751 0.198	-0.171 0.087	-0.226 0.068	-0.071 0.131	3.69/7
152.5	157.5	-0.157 0.258	0.053 0.091	0.261 0.080	-0.519 0.296	0.54/1
147.5	152.5	-0.123 0.202	0.058 0.069	0.324 0.058	0.094	
142.5	147.5	-0.316 0.228	-0.106 0.098	0.588 0.086	0.221	
137.5	142.5	-0.366 0.181	-0.084 0.095	0.516 0.079	0.310	
132.5	137.5	-0.436 0.222	-0.106 0.104	0.507 0.088	0.368	
127.5	132.5	0.217 0.429	0.142 0.138	0.910 0.115	0.397	2.76/3
122.5	127.5	-0.156 0.155	0.006 0.062	0.804 0.064	0.400	1.26/4
117.5	122.5	-0.298 0.156	-0.032 0.059	0.844 0.064	0.382	1.31/2
112.5	117.5	-0.051 0.153	0.089 0.061	0.674 0.065	0.346	0.97/2
107.5	112.5	-0.249 0.185	0.083 0.068	0.624 0.071	0.300	0.62/2
102.5	107.5	-0.861 0.240	-0.122 0.082	0.553 0.084	0.250	0.48/2
97.5	102.5	-0.705 0.234	-0.270 0.088	0.401 0.088	0.203	1.60/2
92.5	97.5	-0.630 0.179	-0.078 0.064	0.421 0.064	0.162	4.58/2
87.5	92.5	-0.359 0.168	-0.075 0.071	0.391 0.070	0.130	0.91/2
82.5	87.5	-0.022 0.206	0.038 0.099	0.364 0.091	0.109	0.13/2
77.5	82.5	0.079 0.142	0.057 0.098	0.269 0.082	0.097	0.52/5
72.5	77.5	-0.050 0.090	-0.032 0.091	0.141 0.075	0.093	
67.5	72.5	0.015 0.067	0.004 0.065	0.133 0.064	0.093	
62.5	67.5	0.040 0.053	0.034 0.051	0.156 0.057	0.094	
57.5	62.5	0.124 0.056	-0.058 0.054	0.095 0.075	0.095	
52.5	57.5	0.039 0.074	-0.006 0.071	-0.019 0.089	0.094	
47.5	52.5	0.167 0.059	0.068 0.062	-0.043 0.072	0.092	
42.5	47.5	0.109 0.063	-0.071 0.059	-0.068 0.118	0.088	

Kinetic Energy = 484 MeV (continued)

θ_{MIN}	θ_{MAX}	$C_{SS} \pm \Delta C_{SS}$	$C_{LS} \pm \Delta C_{LS}$	$C_{LL} \pm \Delta C_{LL}$	$C_{NN} \pm \Delta C_{NN}$	χ^2/d.f.
37.5	42.5	0.071 0.074	0.041 0.077	0.089 0.247	0.081	
32.5	37.5	0.019 0.161	0.051 0.193	----	0.070	
27.5	32.5	0.147 0.454	0.296 0.267	----	0.051	
22.5	27.5	-0.011 0.289	-0.132 0.382	----	0.018	

Kinetic Energy = 634 MeV

θ_{MIN}	θ_{MAX}	$C_{SS} \pm \Delta C_{SS}$	$C_{LS} \pm \Delta C_{LS}$	$C_{LL} \pm \Delta C_{LL}$	$C_{NN} \pm \Delta C_{NN}$	χ^2/d.f.
177.5	180.0	----	----	-0.706 0.113	----	
172.5	177.5	(-1.099 0.193)	-0.078 0.053	-0.802 0.084	(-0.247 0.147)	28.42/27
167.5	172.5	(-0.927 0.187)	0.004 0.072	-0.687 0.095	(-0.392 0.123)	36.19/19
162.5	167.5	-0.768 0.210	-0.082 0.069	-0.058 0.067	-0.466 0.147	14.79/12
157.5	162.5	-0.448 0.260	0.000 0.100	0.103 0.099	-0.401 0.202	3.65/6
152.5	157.5	-0.346 0.358	0.031 0.115	0.346 0.153	-0.006 0.370	0.23/1
147.5	152.5	-0.095 0.254	0.121 0.065	0.460 0.073	0.052	
142.5	147.5	-0.012 0.268	0.017 0.086	0.540 0.078	0.187	
137.5	142.5	-0.377 0.224	-0.114 0.082	0.695 0.093	0.286	
132.5	137.5	-0.199 0.300	0.072 0.088	0.709 0.108	0.352	
127.5	132.5	----	0.048 0.104	0.471 0.135	0.390	1.09/2
122.5	127.5	-0.167 0.185	0.126 0.081	0.679 0.088	0.403	3.17/5
117.5	122.5	-0.258 0.188	0.235 0.068	0.655 0.056	0.396	5.69/3
112.5	117.5	-0.680 0.168	0.007 0.057	0.647 0.061	0.373	7.65/3
107.5	112.5	-0.512 0.190	0.050 0.077	0.642 0.068	0.341	2.08/3
102.5	107.5	-0.580 0.199	-0.011 0.074	0.627 0.061	0.303	1.76/3
97.5	102.5	-0.680 0.347	-0.173 0.142	0.507 0.133	0.262	2.20/3
92.5	97.5	-0.397 0.187	-0.038 0.062	0.624 0.074	0.220	0.74/3
87.5	92.5	-0.120 0.171	-0.052 0.070	0.455 0.077	0.178	3.76/3
82.5	87.5	0.059 0.171	-0.050 0.073	0.473 0.072	0.137	1.39/3
77.5	82.5	0.077 0.165	0.031 0.095	0.283 0.083	0.099	14.55/8
72.5	77.5	0.147 0.106	0.080 0.111	0.285 0.077	0.069	1.92/2
67.5	72.5	0.230 0.086	0.057 0.087	0.184 0.068	0.042	0.90/2
62.5	67.5	0.075 0.081	-0.009 0.081	0.213 0.070	0.019	1.93/2
57.5	62.5	0.114 0.059	-0.076 0.058	0.070 0.082	-0.002	4.57/2
52.5	57.5	-0.096 0.140	-0.039 0.143	0.157 0.121	-0.022	6.80/2
47.5	52.5	0.152 0.084	0.038 0.083	0.078 0.070	-0.043	1.11/2
42.5	47.5	0.064 0.071	-0.012 0.070	-0.043 0.081	-0.064	3.81/2
37.5	42.5	0.140 0.100	-0.020 0.087	0.095 0.097	-0.085	3.19/2
32.5	37.5	-0.008 0.094	0.245 0.135	0.174 0.241	-0.106	0.26/2
27.5	32.5	0.030 0.303	-0.038 0.294	----	-0.131	1.52/2

Kinetic Energy = 720 MeV

θ_{MIN}	θ_{MAX}	$C_{SS} \pm \Delta C_{SS}$		$C_{LS} \pm \Delta C_{LS}$		$C_{LL} \pm \Delta C_{LL}$		C_{NN}
77.5	82.5	---		---		0.073	0.486	0.087
72.5	77.5	0.301	0.305	0.005	0.255	0.398	0.186	0.080
67.5	72.5	0.192	0.181	0.044	0.216	0.289	0.137	0.072
62.5	67.5	0.181	0.137	-0.008	0.145	0.091	0.098	0.060
57.5	62.5	0.292	0.107	0.036	0.123	-0.063	0.117	0.042
52.5	57.5	0.326	0.192	-0.025	0.218	-0.035	0.188	0.018
47.5	52.5	-0.038	0.171	-0.329	0.173	-0.354	0.124	-0.011
42.5	47.5	0.144	0.132	0.027	0.150	-0.078	0.122	-0.043
37.5	42.5	-0.098	0.160	0.097	0.107	-0.258	0.124	-0.076
32.5	37.5	0.190	0.207	-0.155	0.154	-0.100	0.272	-0.109
27.5	32.5	-0.075	0.201	-0.023	0.442	---		-0.142

Kinetic Energy = 788 MeV

θ_{MIN}	θ_{MAX}	$C_{SS} \pm \Delta C_{SS}$		$C_{LS} \pm \Delta C_{LS}$		$C_{LL} \pm \Delta C_{LL}$		C_{NN}	χ^2/d.f.
172.5	177.5	-1.237	0.395	-0.274	0.131	-0.589	0.134	-0.748	1.00/3
167.5	172.5	---		-0.034	0.073	-0.347	0.069	-0.716	2.03/3
162.5	167.5	-0.302	0.556	-0.026	0.060	-0.107	0.062	-0.481	0.73/3
157.5	162.5	0.332	0.491	0.068	0.090	0.251	0.080	-0.205	0.60/3
152.5	157.5	-0.136	0.582	-0.004	0.272	0.574	0.204	0.020	1.47/3
147.5	152.5	-0.392	0.275	-0.252	0.136	0.837	0.152	0.186	1.30/3
142.5	147.5	0.534	0.457	0.063	0.153	0.375	0.170	0.288	1.21/3
137.5	142.5	-0.099	0.363	-0.227	0.125	0.747	0.129	0.320	6.66/3
132.5	137.5	0.170	0.325	-0.051	0.118	0.761	0.124	0.286	4.91/3
127.5	132.5	-0.589	0.323	-0.082	0.121	0.448	0.125	0.202	13.54/8
122.5	127.5	-0.353	0.220	-0.070	0.103	0.495	0.067	0.096	7.42/9
117.5	122.5	0.020	0.225	0.106	0.082	0.431	0.058	-0.004	0.81/3
112.5	117.5	0.011	0.196	0.102	0.081	0.573	0.059	-0.084	1.55/3
107.5	112.5	-0.107	0.226	-0.053	0.092	0.612	0.063	-0.134	6.16/3
102.5	107.5	-0.153	0.225	0.017	0.077	0.777	0.067	-0.152	4.18/3
97.5	102.5	0.331	0.437	0.132	0.189	0.521	0.150	-0.136	5.04/3
92.5	97.5	-0.291	0.266	-0.163	0.072	0.655	0.066	-0.090	1.32/3
87.5	92.5	-0.389	0.227	-0.131	0.098	0.714	0.081	-0.028	0.13/3
82.5	87.5	-0.030	0.256	-0.103	0.097	0.397	0.083	0.030	2.22/3
77.5	82.5	0.030	0.156	0.002	0.115	0.194	0.118	0.074	17.31/9
72.5	77.5	0.001	0.150	-0.107	0.131	0.199	0.112	0.103	3.38/9
67.5	72.5	0.166	0.116	0.206	0.185	0.249	0.129	0.119	0.59/3
62.5	67.5	0.085	0.066	0.198	0.084	0.208	0.078	0.121	0.90/3

Kinetic Energy = 788 MeV (continued)

θ_{MIN}	θ_{MAX}	C_{SS}	$\pm \Delta C_{SS}$	C_{LS}	$\pm \Delta C_{LS}$	C_{LL}	$\pm \Delta C_{LL}$	C_{NN}	χ^2/d.f.
57.5	62.5	0.026	0.048	0.263	0.069	0.124	0.076	0.106	1.64/3
52.5	57.5	0.008	0.063	0.193	0.087	0.106	0.123	0.076	0.64/3
47.5	52.5	0.201	0.077	0.211	0.093	0.047	0.080	0.036	0.91/3
42.5	47.5	0.043	0.054	0.380	0.096	-0.017	0.088	-0.009	2.14/3
37.5	42.5	-0.088	0.060	0.079	0.125	-0.170	0.143	-0.056	0.76/3
32.5	37.5	0.071	0.088	0.310	0.160	0.094	0.162	-0.101	0.80/3
27.5	32.5	-0.135	0.132	-0.016	0.189	0.058	0.227	-0.144	0.27/3
22.5	27.5	0.096	0.329	0.424	0.340	----		-0.186	0.18/3

TABLE 7

Consistency of 90° c.m. data. The values of $C_{LL}(np)$ and $C_{SS}(np)$ are calculated using Eqs. 3 and 4 with experimental data given in Table V of Ref. 16. The calculated values are to be compared with measured data from Table 6, which are also given.

	T_n = 484 GeV	634 MeV	788 MeV
$C_{LL,calc}$ (np)	+ 0.34 ± 0.04	+ 0.45 ± 0.04	+ 0.54 ± 0.05
C_{LL} (np)	+ 0.391 ± 0.070	+ 0.455 ± 0.077	+ 0.714 ± 0.081
$C_{SS,calc}$ (np)	- 0.21 ± 0.05	- 0.08 ± 0.05	+ 0.12 ± 0.06
C_{SS} (np)	-0.36 ± 0.17	-0.12 ± 0.17	-0.39 ± 0.23

TABLE 8

Comparison of phase shift and model predictions to the data in Table 6. The chi-squared per degree of freedom is given at each energy for the predictions of the Saclay-Geneva,[4] VPI,[49] Queen Mary College,[7,50] and Kyoto[2] phase shift groups and for the meson-exchange model of Lee et al.[51] At 567 MeV, the predictions are compared to the mixed spin parameter given in Table 4.

T_{lab}	Saclay-Geneva	VPI	Queen Mary College	Kyoto	Lee et al.	d.f.
484 MeV	2.80	1.91	2.05	2.91	2.11	96
567 MeV	10.99	1.77	----	3.08	1.83	9
634 MeV	3.54	1.47	1.62	2.40	2.12	94
720 MeV	3.40	0.99	----	1.62	1.02	30
788 MeV	6.83	1.93	1.84	2.82	3.55	91

TABLE 9

Total cross section differences for longitudinal and transverse beam and target polarizations. These cross sections were obtained using Eq. 5 and Refs. 49, 52, 54, 57, 58, and the data in Table 6, as described in the text.

a) $\Delta\sigma_L$

T_{lab}	484 MeV	634 MeV	788 MeV
Partial $\Delta\sigma_L$ (np, elastic)	-11.03 ± 1.01 mb	-10.40 ± 1.10 mb	-6.66 ± 0.52 mb
c.m. Angle Range	40 - 180°	35 - 180°	30 - 175°
C_{LL} $d\sigma/d\Omega$ (0°)	-1.45 ± 0.35 mb/sr	-2.28 ± 0.38 mb/sr	-1.34 ± 0.59 mb/sr
Estimated $\Delta\sigma_L$ (np, elastic)	-7.6 ± 2.9 mb	-7.6 ± 5.6 mb	-4.3 ± 1.5 mb
Measured $\Delta\sigma_L$ (np, total)	-6.07 ± 1.27 mb	-2.23 ± 1.12 mb	-6.65 ± 0.93 mb
Estimated $\Delta\sigma_L$ (I = 0, elastic)	+2.0 ± 5.9	-1.5 ± 11.2 mb	+5.5 ± 3.2 mb
Measured $\Delta\sigma_L$ (I = 0, total)	-0.35 ± 2.55 mb	+7.40 ± 2.25 mb	+3.91 ± 1.89 mb

b) $\Delta\sigma_T$

T_{lab}	484 MeV	634 MeV	788 MeV
Partial $\Delta\sigma_T$ (np, elastic)	+3.87 ± 1.06 mb	+2.30 ± 0.85 mb	-0.36 ± 1.03 mb
C_{SS} c.m. Angle Range	25 - 175°	30 - 175°	25 - 175°
C_{NN} c.m. Angle Range	70 - 175°	70 - 175°	30 - 150°
C_{NN} $d\sigma/d\Omega$ (0°) = C_{SS} $d\sigma/d\Omega$ (0°)	-2.16 ± 0.27 mb/sr	-3.20 ± 0.58 mb/sr	-3.33 ± 1.24 mb/sr
$-\int C_{NN}\, d\sigma/d\Omega\, d\Omega$	-1.1 ± 7.2 mb	-1.8 ± 13.6 mb	+0.30 ± 0.28 mb
$-\int C_{SS}\, d\sigma/d\Omega\, d\Omega$	+3.03 ± 0.44 mb	+2.04 ± 0.45 mb	+1.58 ± 0.54 mb
Estimated $\Delta\sigma_T$ (np, elastic)	+1.9 ± 7.2 mb	+0.2 ± 13.6 mb	+1.88 ± 0.61 mb
Measured $\Delta\sigma_T$ (np, total)	+ 10.9 ± 1.9 mb	+7.84 ± 4.06 mb	+7.57 ± 0.66 mb
Estimated $\Delta\sigma_T$ (I = 0, elastic)	+3.2 ± 14.4 mb	+1.2 ± 27.2 mb	+4.2 ± 1.2 mb
Measured $\Delta\sigma_T$ (I = 0, total)	+15.0 ± 3.8 mb	+9.36 ± 8.04 mb	+10.18 ± 0.76 mb

Figure Captions

Figure 1 Definition of the spin directions for the beam, target, forward-scattered, and recoil particles for nucleon-nucleon elastic scattering.

Figure 2 Layout of the experimental area. The polarized neutron beam entered from the top of the figure through a collimator and lead plug, and then passed through the front beam-intensity monitor (FMON), spin-precession magnets (Lorraine and Castor), a relative neutron polarimeter (JPAN), and the polarized target (HERA). The magnetic spectrometer consisted of scintillation counters (S_1, S_2), multiwire proportional chambers (P_0, P_2), and drift chambers (P_1, P_3, P_4) attached to a large-aperture magnet (SCM-105). Two other beam-intensity monitors (T_{MON}, B_{MON}) are also shown as well as various equipment associated with the polarized target and magnets.

Figure 3a Values of A_{np} (30° lab) determined by fits to the world's data (Refs. 26-36) in the c.m. angular range 80° - 140°. Statistical errors and combined statistical and systematic errors are shown. Note the spread in the data.

Figure 3b Plot of the computed values of A_{np} weighted by the acceptance and cross section from Ref. 22. The Newsom et al. data (Ref. 32) were normalized as described in the text. The solid line is a fit to these results as a function of laboratory kinetic energy. The dashed line is a similar fit to all the data, but in this case the Ref. 32 results were not normalized.

Figure 4 Schematic diagram of the spin-gated run control logic used for this experiment. The signals are defined in the text.

Figure 5 Histogram of the c.m. scattering angle for the 634 MeV $C_{\sigma\sigma}$ data with the spectrometer centered at a laboratory angle of 35°. The events shown passed cuts on the projected target positions and the missing mass, which included the elastic scattering events.

Figure 6 Distribution of the projected x interaction point in the polarized target for the 634 MeV $C_{\lambda L}$ data. The spectrometer was centered at a laboratory angle of 35°. The target magnet was oriented to give a pure L-type polarization, and the beam was far from any part of the magnet cryostat. The final cuts for the $C_{\lambda L}$ data are shown as lines.

Figure 7 Histogram of the projected x interaction point in the polarized target for the 634 MeV $C_{\sigma\sigma}$ data. The spectrometer was centered at a laboratory angle of 35° (a) and 10° (b); note the comparison to Fig. 6. Interactions from the magnet cryostat can be seen as the events to the sides of the main peak. The final cuts on this quantity for the $C_{\sigma\sigma}$ data are indicated with lines.

Figure 8 Histogram of the projected x interaction point in the polarized target for the 634 MeV $C_{\lambda\lambda}$ data. The spectrometer was centered at a laboratory angle of 57.5°. Multiple scattering and imperfect energy loss corrections and corrections for the effect of the target magnetic field on the slow recoil proton trajectories broadened this distribution compared to Fig. 6. The final cuts on this quantity for the $C_{\lambda\lambda}$ are indicated with lines.

Figure 9 Two dimensional histogram of the x position in chamber P1 and the projected x interaction point in the polarized target. Interactions from the target are located in a horizontal band, mostly contained within the "box cuts" shown for the final data. Interactions from magnet cryostat walls are located in bands with a nonzero slope.

Figure 10 Histograms of the differences, DXTT (a) and DYTT (b), in the position of the straight line projections of tracks from the upstream and downstream chambers to the center of the SCM105 magnet. The data are from the 634 MeV $C_{\lambda\lambda}$ measurements with a spectrometer laboratory angle of 57.5°. The final cuts on these quantities for the $C_{\lambda\lambda}$ data are indicated with lines.

Figure 11 Histograms of the kinematic quantity η for the 720 MeV $C_{\lambda\lambda}$ data with a spectrometer laboratory angle of 57.5°. The polarized target results are given in (a) and (b), and the carbon background data in (c) and (d). The c.m. angular ranges are 47.5° - 52.5° ((a) and (c)) and 72.5° - 77.5° ((b) and (d)).

Figure 12 Histograms of the kinematic quantity η for 484 MeV carbon background data at $\theta_{c.m.}$ = 47.5° - 52.5° (a) and 72.5° - 77.5° (b). Ratios of the boron nitride background to the carbon background are shown at the same c.m. angles ((c) and (d) respectively). Ratios of liquid nitrogen to carbon, also at the same angles, are given in (e) and (f). These ratios are not corrected for the total incident beam, target thickness, empty target background, etc. Note that the ratios are reasonably constant as a function of η.

Figure 13 Measured values of the mixed spin observables (a) $C_{\lambda L}$ and (b) $C_{\sigma L}$ at 634 MeV and a spectrometer laboratory angle of 35°. The curves show phase shift predictions of Arndt et al. (solid line, Ref. 49), Hoshizaki et al. (dot-dashed line, Ref. 2), and Bystricky et al. (dashed line, Ref. 4).

Figure 14 Measured values of mixed spin observables with the polarized target magnetic field rotated at an angle of 37.5° with respect to the beam. The beam kinetic energy and spin observable are: (a) 484 MeV $C_{\sigma\sigma}$ (b) 484 MeV $C_{\lambda\sigma}$, (c) 634 MeV $C_{\sigma\sigma}$, and (d) 788 MeV $C_{\sigma\sigma}$. The curves are the same as Fig. 13.

Figure 15 Measured values of the mixed spin observable $C_{\lambda\lambda}$ at a spectrometer laboratory angle of 57.5°. The laboratory beam kinetic energies were: (a) 484 MeV, (b) 567 MeV, (c) 634 MeV, (d) 720 MeV, and (e) 788 MeV. The curves are the same as Fig. 13.

Figure 16 Derived values of the pure spin-spin parameters (a) C_{LL} and (b) $C_{SL} = C_{LS}$ at 634 MeV from the $C_{\lambda L}$ and $C_{\sigma L}$ data in Table 3 (solid circles). Also shown are the revised C_{LL} and C_{SL} data from Ref. 16 (open circles).

Figure 17 The pure spin-spin observable C_{SS} from this experiment and Refs. 16 and 17 at (a) 484 MeV, (b) 634 MeV, (c) 720 MeV, and (d) 788 MeV. The curves are from phase shift predictions of Arndt et al. (solid, Ref. 49) and Bugg (dashed, Refs. 7, 50). A model prediction by Lee et al. (dot-dashed, Ref. 51) is also shown.

Figure 18 The pure spin-spin observable $C_{SL} = C_{LS}$ from this experiment and Refs. 16 and 17 at (a) 484 MeV, (b) 634 MeV, (c) 720 MeV, and (d) 788 MeV. The curves are described in Fig. 17. The open triangles in (c) and (d) correspond to quasielastic data with a polarized deuteron beam at 744 and 794 MeV equivalent energy from Ref. 31, and the open circles to free np elastic scattering data at 800 MeV from Ref. 52.

Figure 19 The pure spin-spin observable C_{LL} from this experiment and Refs. 16 and 17 at (a) 484 MeV, (b) 634 MeV, (c) 720 MeV, and (d) 788 MeV. The curves are described in Fig. 17. The open circles in (b) and (d) correspond to free np elastic scattering data at 630 MeV (Ref. 53) and 800 MeV (Ref. 52).

Figure 20 The pure spin-spin observable C_{NN} from this experiment at (a) 484 MeV, and (b) 634 MeV. The curves are described in Fig. 17. The open squares in (a) and (b) correspond to free np elastic scattering data at 465 and 665 MeV, respectively (Ref. 54).

Figure 21 Pure I = 0 (a,c,e) and interference of I = 0 and I = 1 (b,d,f) spin-spin observables ($C_{SS} \cdot d\sigma/d\Omega$) derived from data in Table 6 and from VPI phase shift predictions.[49] The energies are 484 (a,b), 634 (c,d), and 788 (e,f) MeV . The curves show phase shift predictions of Arndt et al. (solid line, Ref. 49), Hoshizaki et al. (dot-dashed line, Ref. 2), and Bystricky et al. (dashed line, Ref. 4).

Figure 22 Pure I = 0 (a,c,e) and interference of I = 0 and I = 1 (b,d,f) spin-spin observables ($C_{LL} \cdot d\sigma/d\Omega$) derived from data in Table 6 and from VPI phase shift predictions.[49] The energies are 484 (a,b), 634 (c,d) and 788 (e,f) MeV and the curves are the same as in Fig. 21.

Figure 23 Pure I = 0 (a,c,e) and interference of I = 0 and I = 1 (b,d,f) spin-spin observables ($C_{LS} \cdot d\sigma/d\Omega$) derived from data in Table 6 and from VPI phase shift predictions.[49] The energies are 484 (a,b), 634 (c,d), and 788 (e,f) MeV, and the curves are the same as in Fig. 21.

Figure 24 Total np cross section differences between antiparallel and parallel spin states, a) $\Delta\sigma_L$ (np) and b) $\Delta\sigma_T$ (np), as a function of lab kinetic energy. The total elastic cross sections (solid circles) are from Table 9 and are described in the text. The measured values for $\Delta\sigma_L$ (np, total) and $\Delta\sigma_T$ (np, total) are from PSI (Ref. 61, open squares), LAMPF (Ref. 63, open circles), and Saclay (Refs. 59, 60, 62, open triangles), and the curves are PSA predictions from Arndt et al.[49] The solid lines correspond to the total and the dashed lines to the elastic cross sections.

Figure 25 Total isospin-0 cross section differences between antiparallel and parallel spin states, a) $\Delta\sigma_L$ (I = 0) and b) $\Delta\sigma_T$ (I = 0), as a function of lab kinetic energy. The total elastic cross sections (solid circles) are from Table 9 and are described in the text. The measured values for $\Delta\sigma_L$ (I = 0, total) and $\Delta\sigma_T$ (I = 0, total) are from PSI (Ref. 61, open squares), LAMPF (Ref. 63, open circles), and Saclay (Refs. 59, 60, 62, open triangles), and the curves are PSA predictions from Arndt et al.[49] The solid lines correspond to the total and the dashed lines to the elastic cross sections.

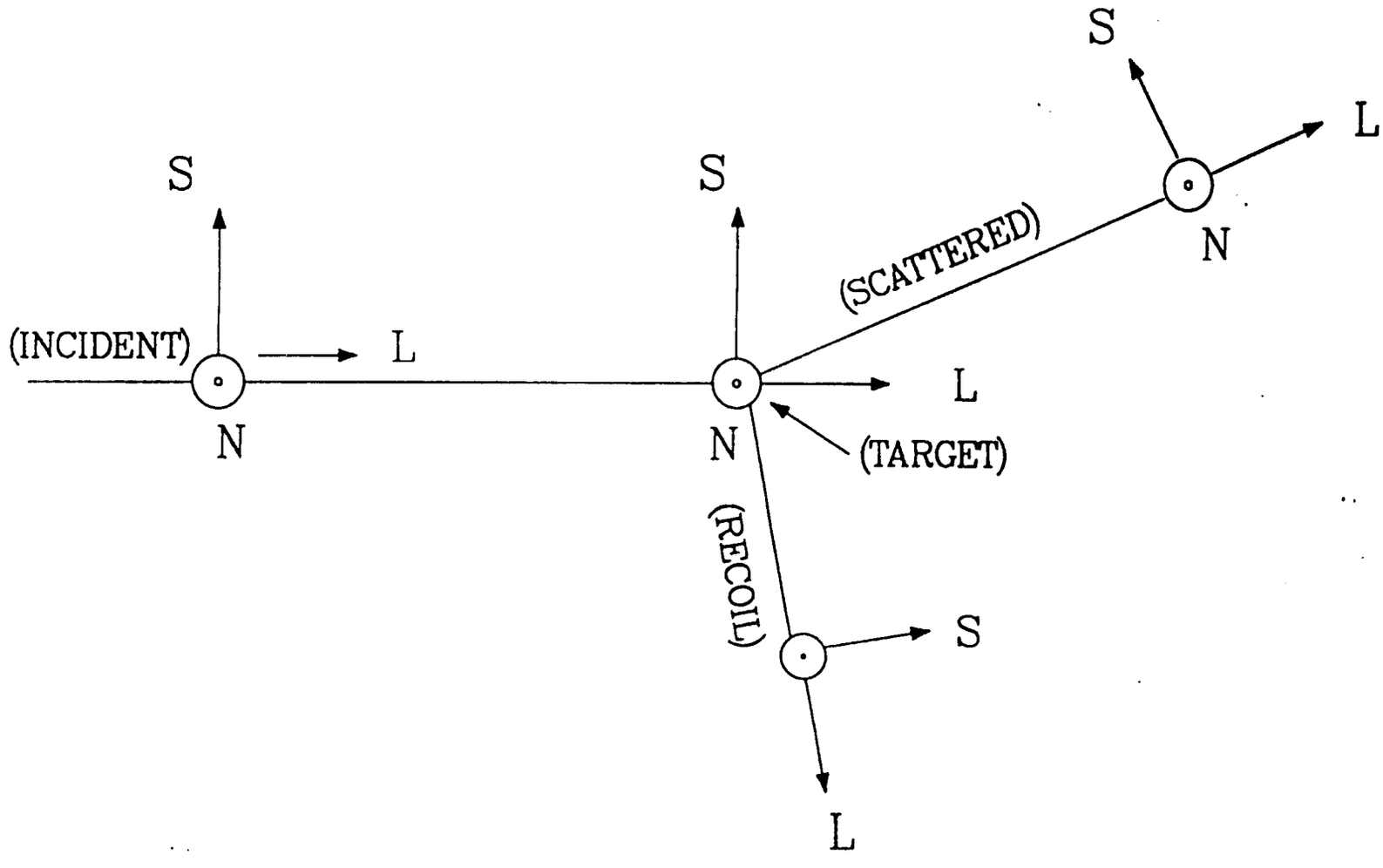

N: NORMAL TO THE SCATTERING PLANE

L: LONGITUDINAL DIRECTION

S= N x L IN THE SCATTERING PLANE

Figure 1

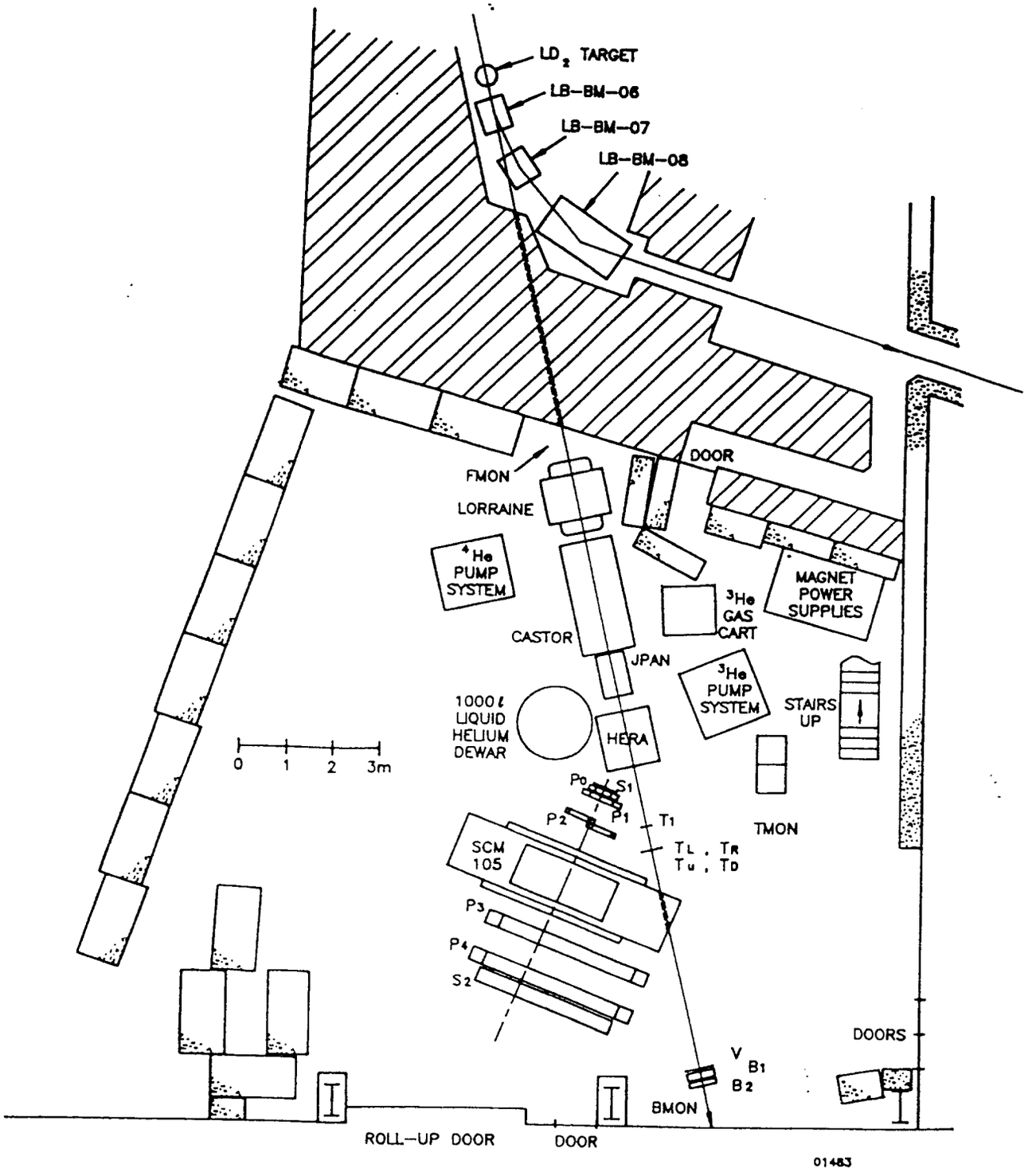
LD2 TARGET
LB–BM–06
LB–BM–07
LB–BM–08
FMON
LORRAINE
DOOR
4He PUMP SYSTEM
MAGNET POWER SUPPLIES
3He GAS CART
CASTOR
JPAN
3He PUMP SYSTEM
STAIRS UP
1000 ℓ LIQUID HELIUM DEWAR
HERA
0 1 2 3m
P0
S1
P2
P1
T1
TMON
SCM 105
TL , TR
TU , TD
P3
P4
S2
V
B1
B2
DOORS
BMON
ROLL–UP DOOR
DOOR
01483

Figure 2

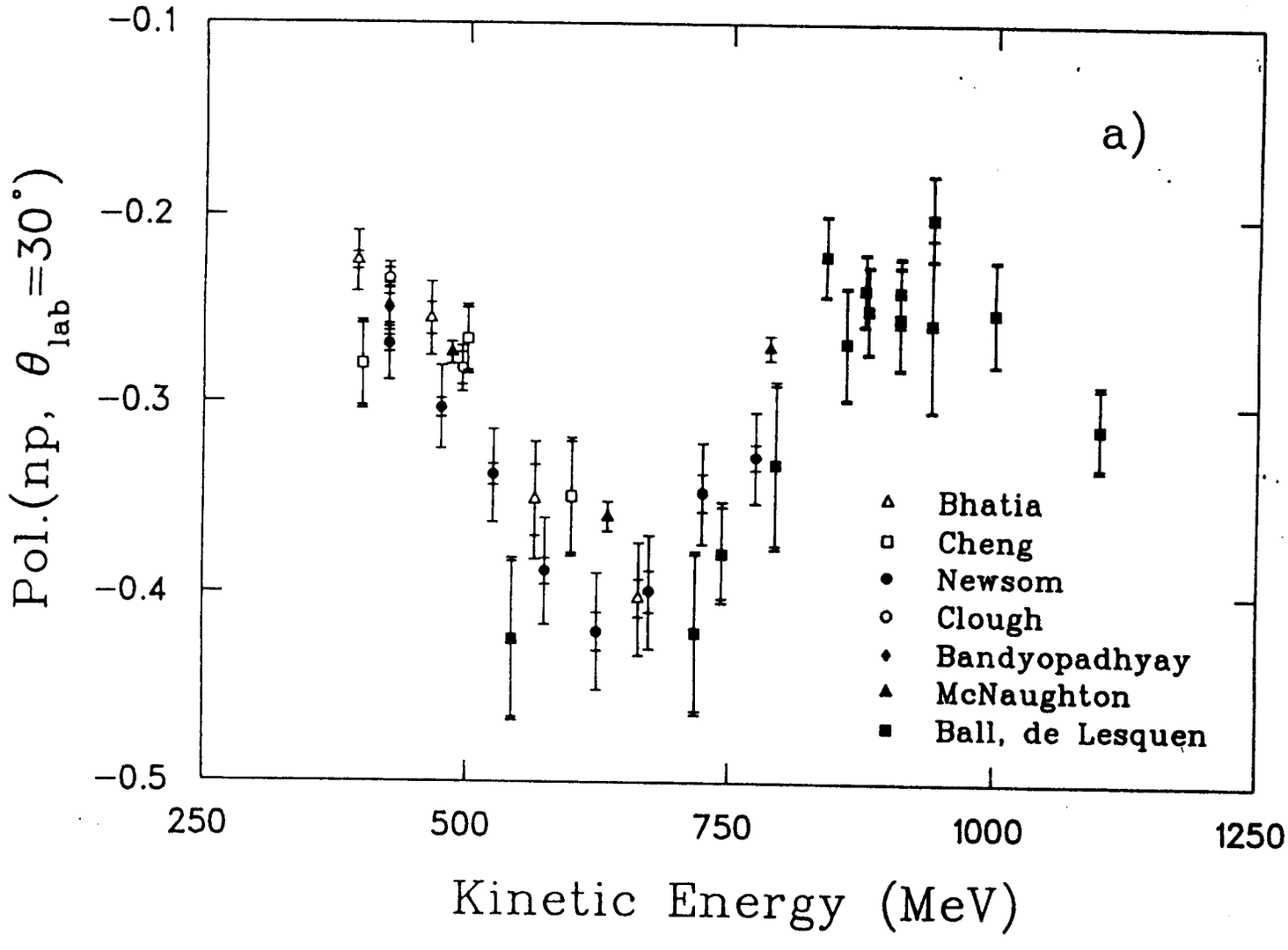
a)
Pol.(np, θ_{lab}=30°)
Kinetic Energy (MeV)
−0.1
−0.2
−0.3
−0.4
−0.5
250
500
750
1000
1250
Bhatia
Cheng
Newsom
Clough
Bandyopadhyay
McNaughton
Ball, de Lesquen

Figure 3a

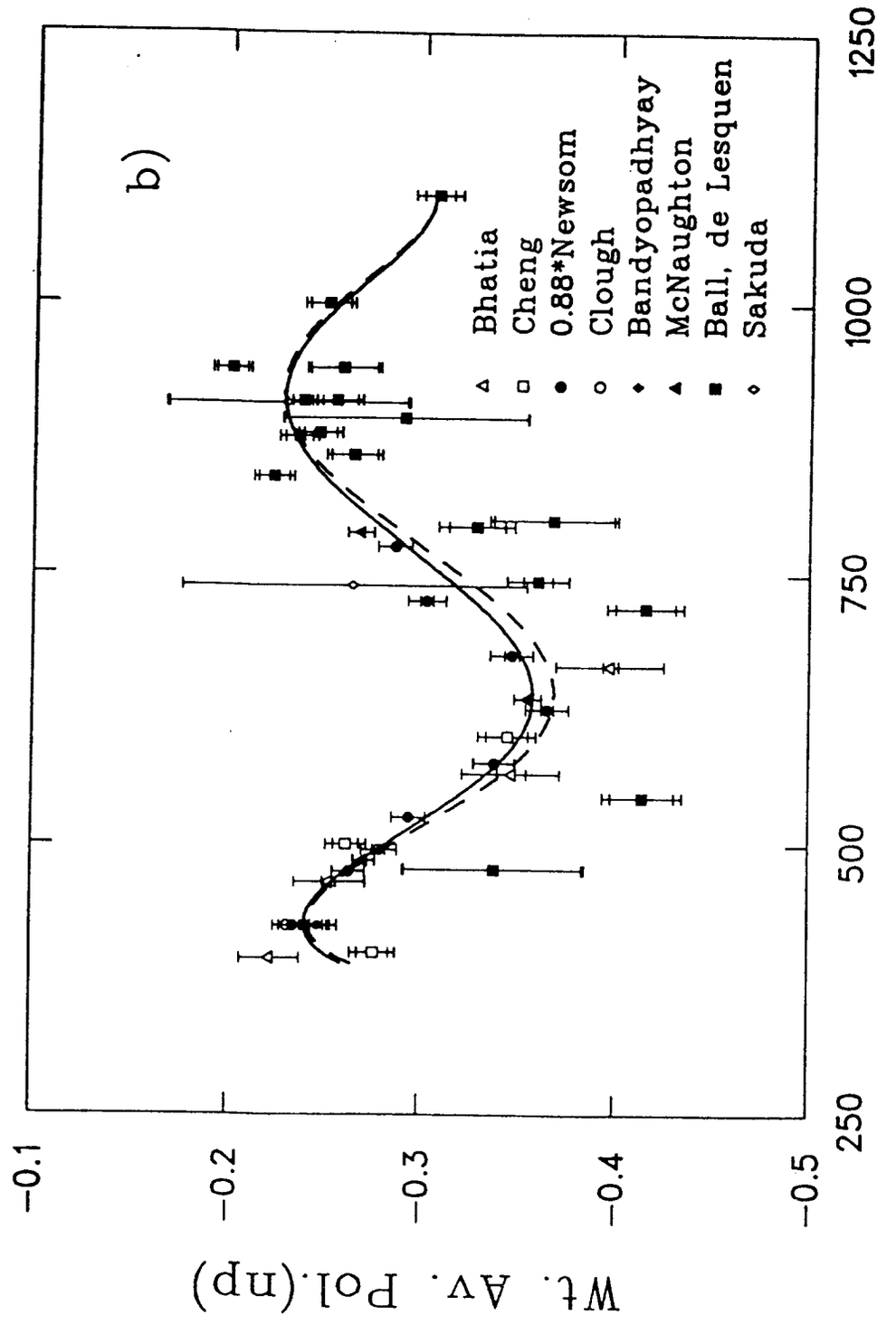
b)
Bhatia
Cheng
0.88*Newsom
Clough
Bandyopadhyay
McNaughton
Ball, de Lesquen
Sakuda
Wt. Av. Pol.(np)
-0.1
-0.2
-0.3
-0.4
-0.5
250
500
750
1000
1250
Kinetic Energy (MeV)

Figure 3b

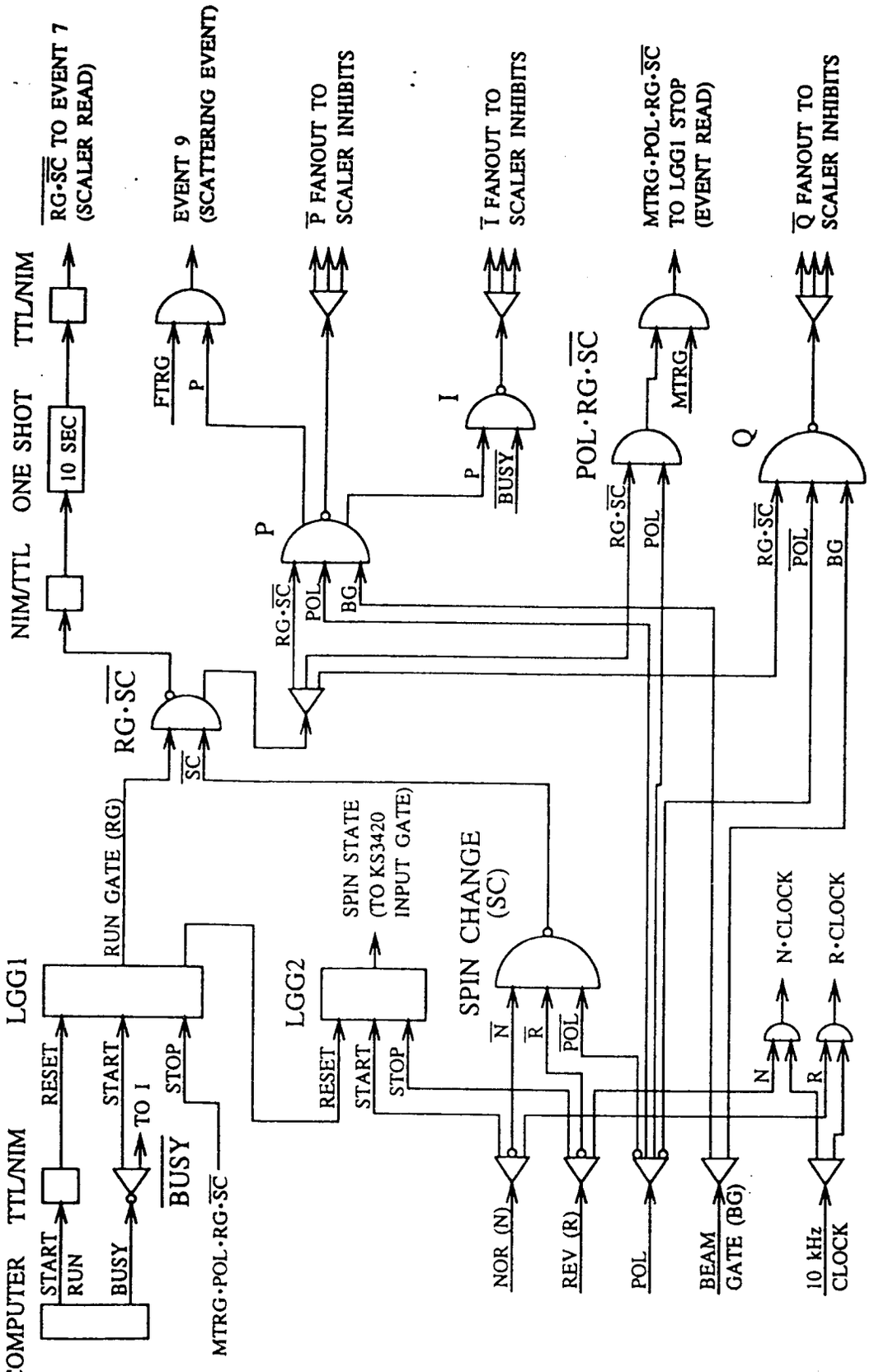
COMPUTER TTL/NIM
START
RUN
BUSY
LGG1
RESET
START
STOP
TO I
BUSY
MTRG·POL·RG·SC
RUN GATE (RG)
NIM/TTL ONE SHOT TTL/NIM
10 SEC
RG·SC TO EVENT 7
(SCALER READ)
RG·SC
SC
FTRG
P
EVENT 9
(SCATTERING EVENT)
P
RG·SC
POL
BG
P FANOUT TO
SCALER INHIBITS
I
P
BUSY
I FANOUT TO
SCALER INHIBITS
LGG2
RESET
START
STOP
SPIN STATE
(TO KS3420
INPUT GATE)
SPIN CHANGE
(SC)
N
R
POL
NOR (N)
REV (R)
POL·RG·SC
RG·SC
POL
MTRG
MTRG·POL·RG·SC
TO LGG1 STOP
(EVENT READ)
POL
BEAM
GATE (BG)
Q
RG·SC
POL
BG
Q FANOUT TO
SCALER INHIBITS
N
R
N·CLOCK
R·CLOCK
10 kHz
CLOCK

Figure 4

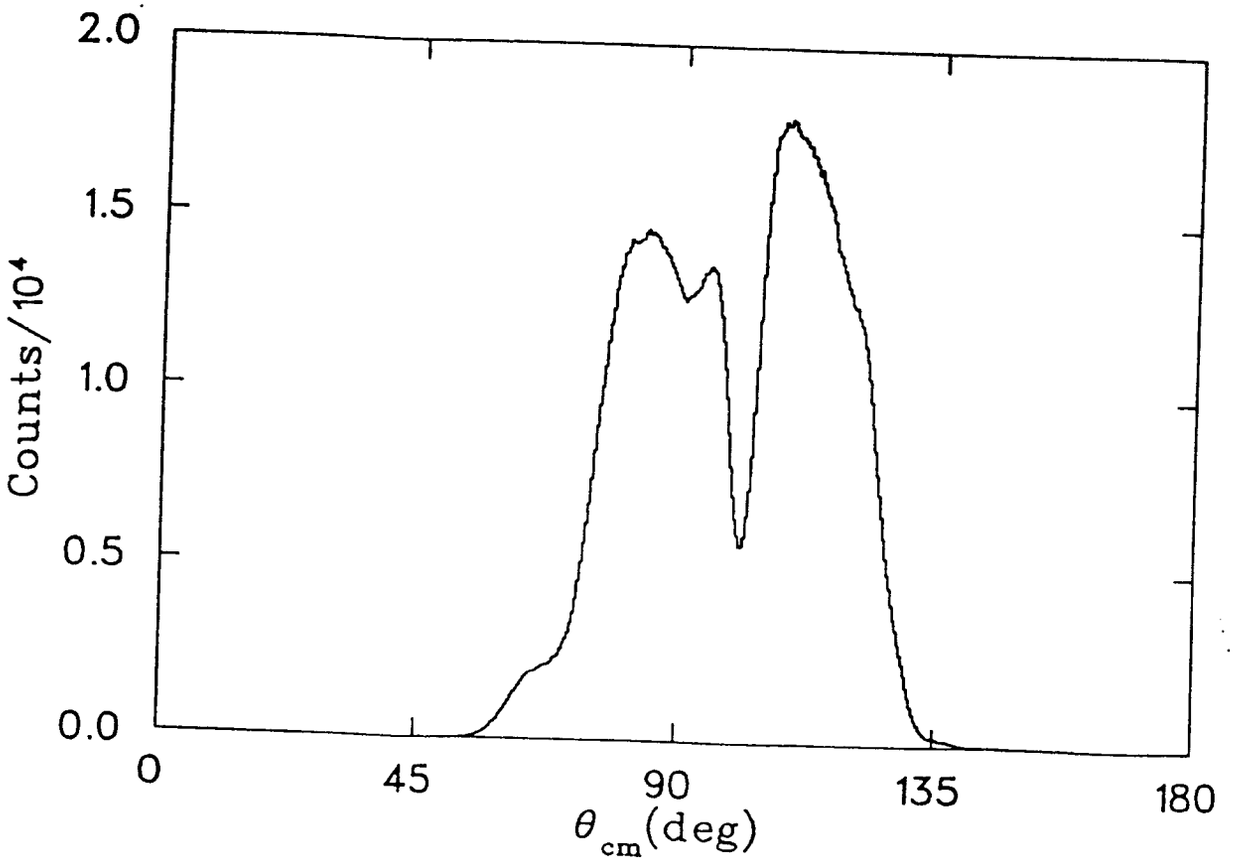

Figure 5

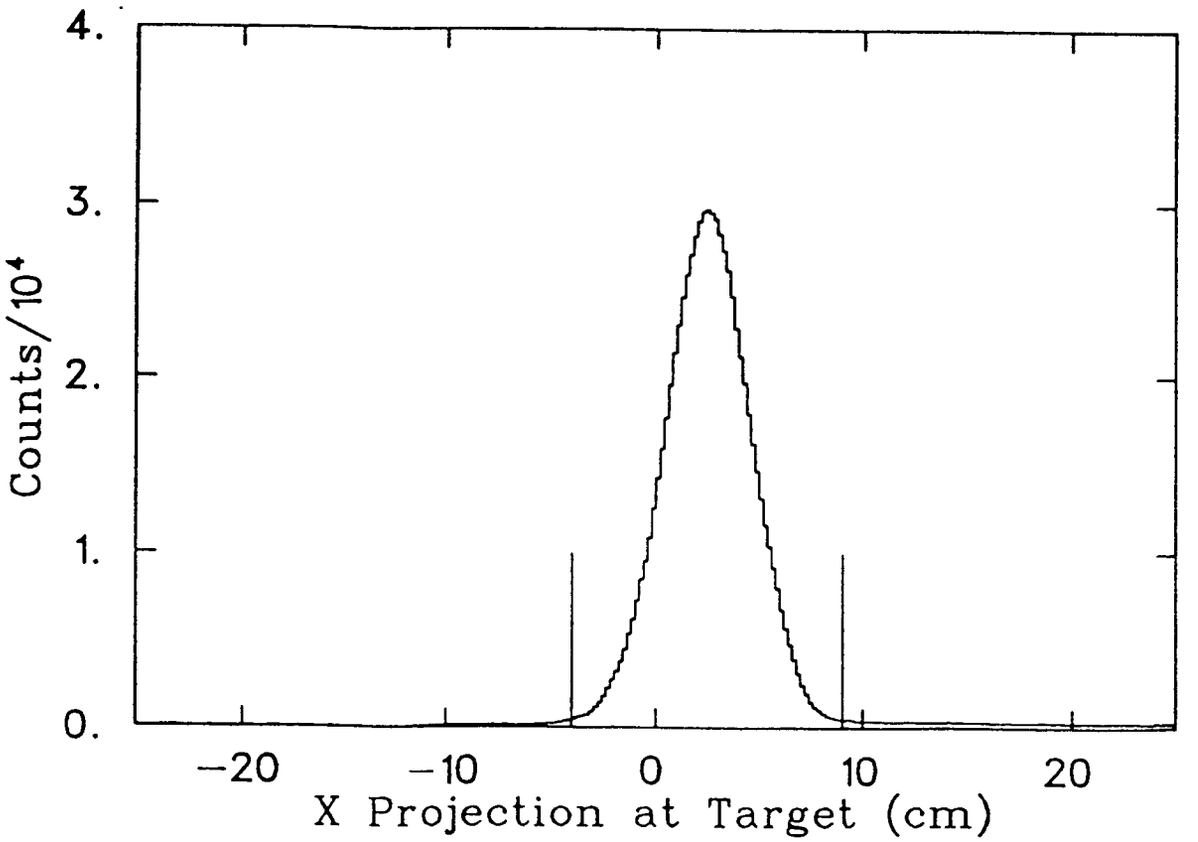

Figure 6

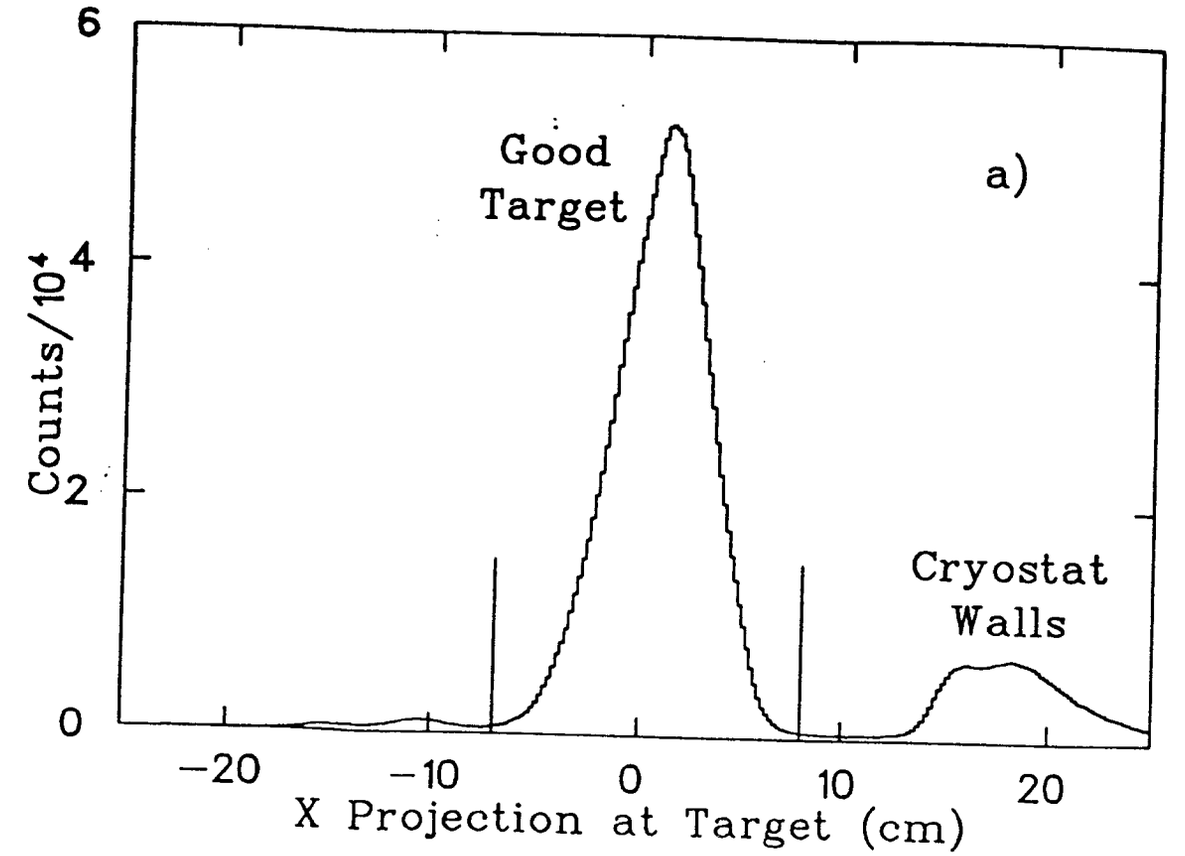
Good
Target
a)
Cryostat
Walls
Counts/10⁴
6
4
2
0
−20
−10
0
10
20
X Projection at Target (cm)

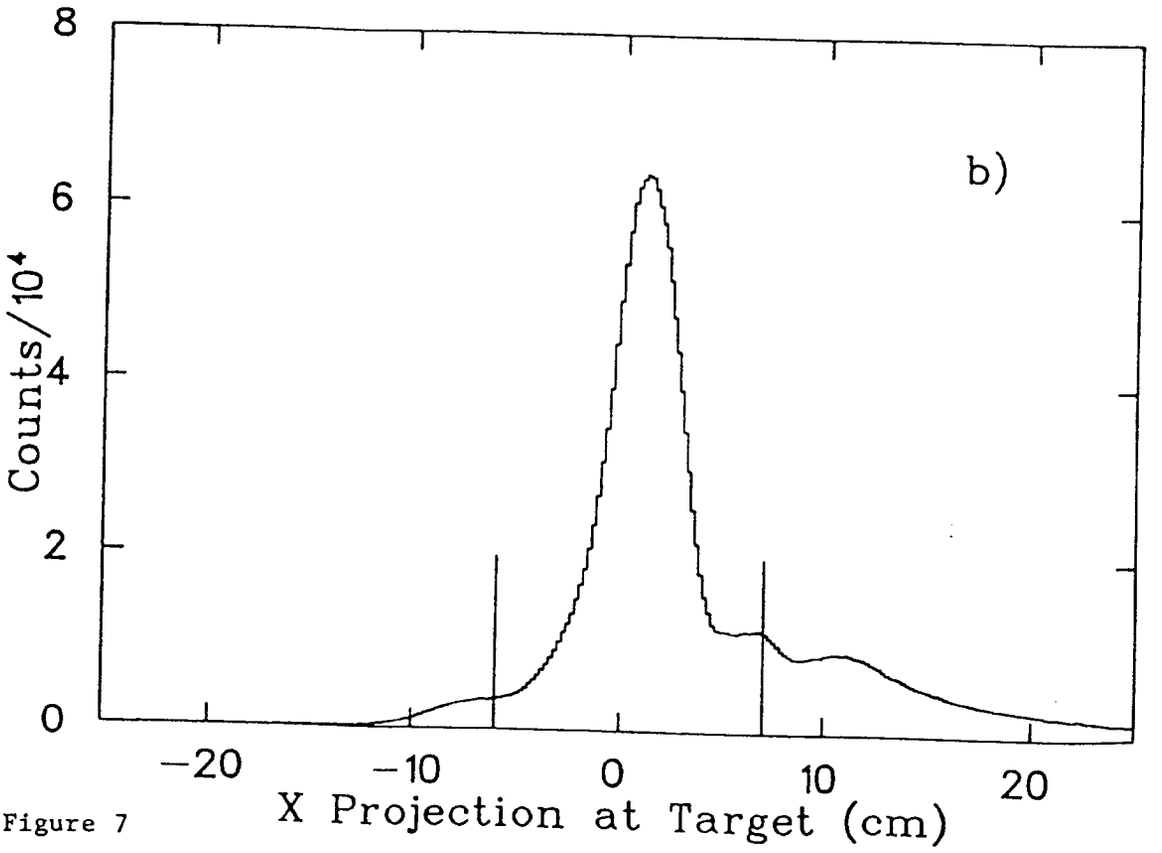
b)
Counts/10⁴
8
6
4
2
0
−20
−10
0
10
20
X Projection at Target (cm)

Figure 7

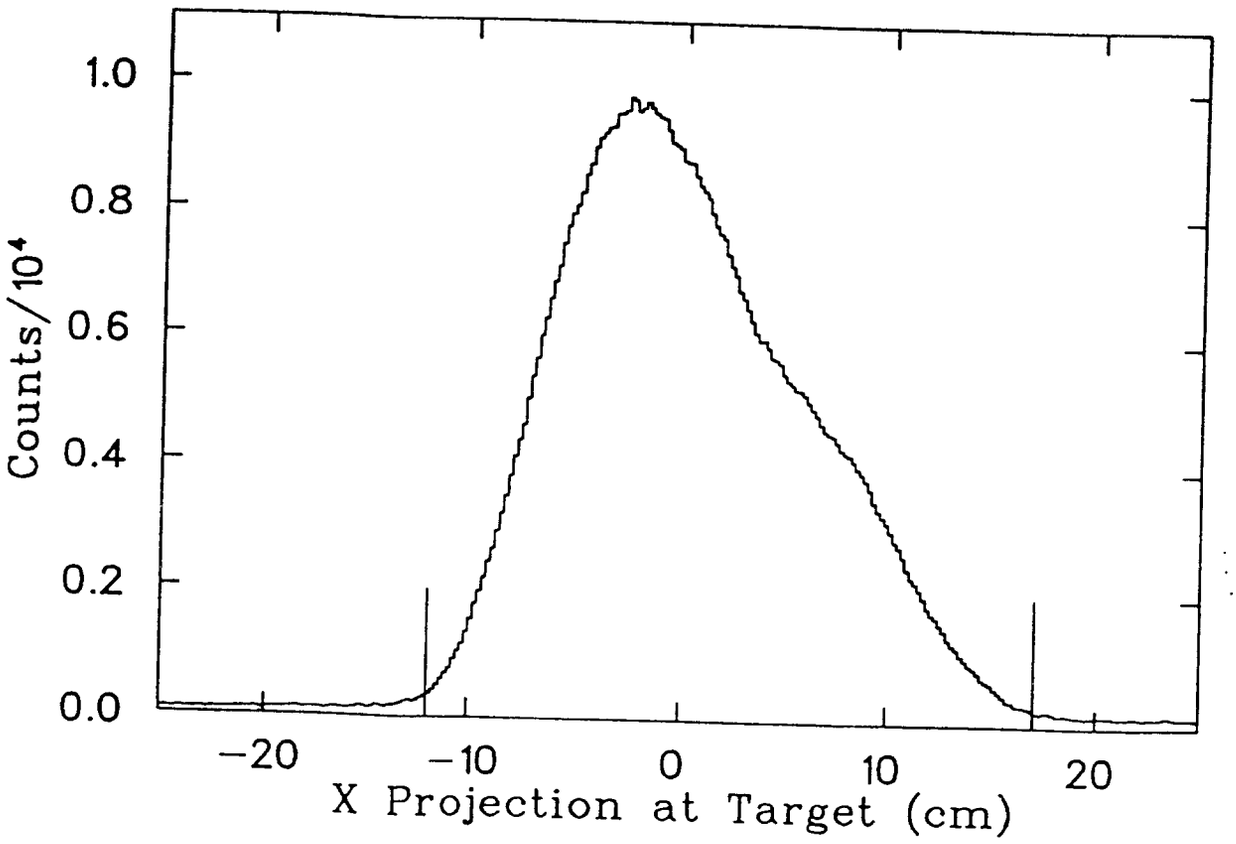
1.0
0.8
0.6
0.4
0.2
0.0
Counts/10⁴
−20
−10
0
10
20
X Projection at Target (cm)

Figure 8

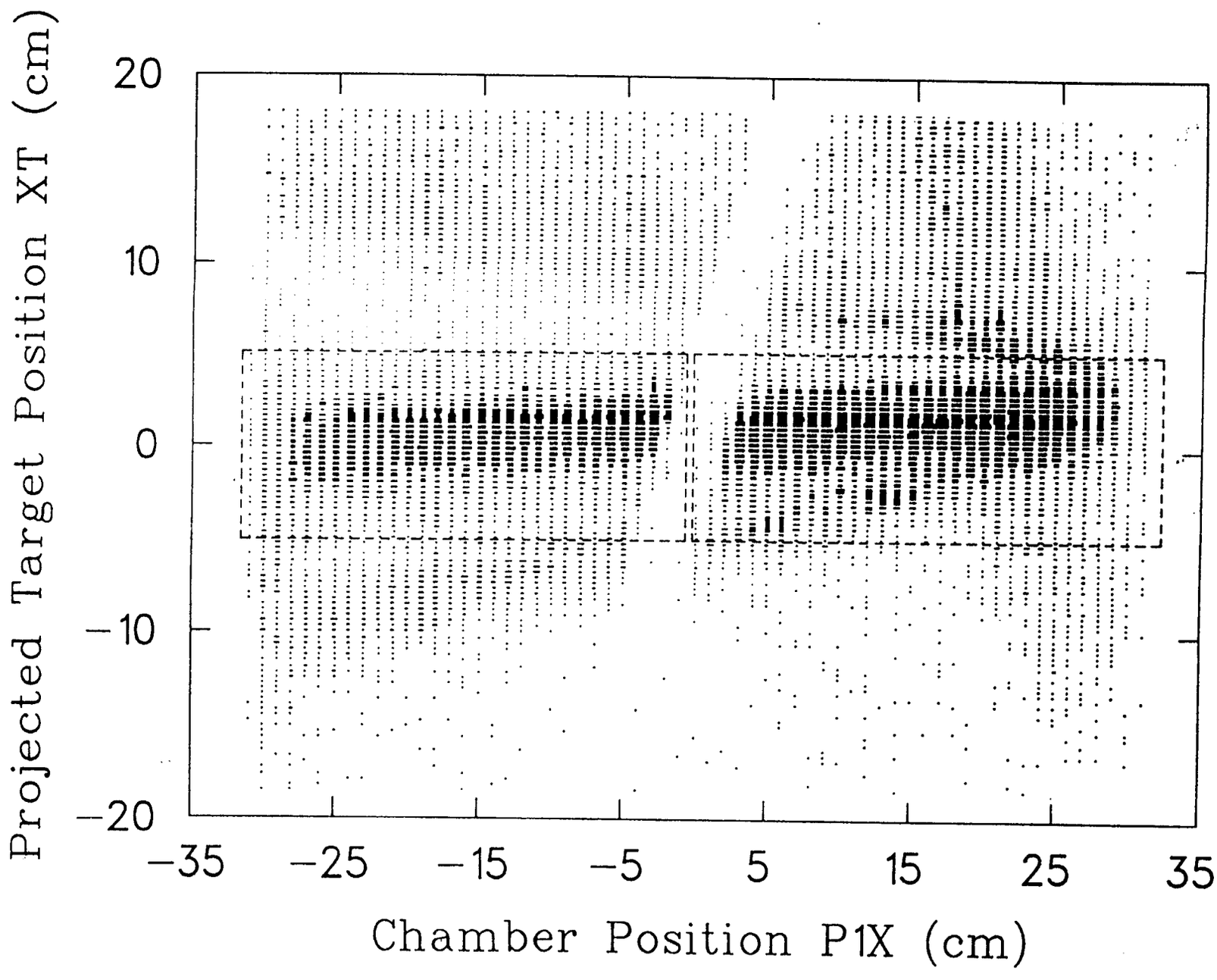
Projected Target Position XT (cm)
20
10
0
−10
−20
−35
−25
−15
−5
5
15
25
35
Chamber Position P1X (cm)

Figure 9

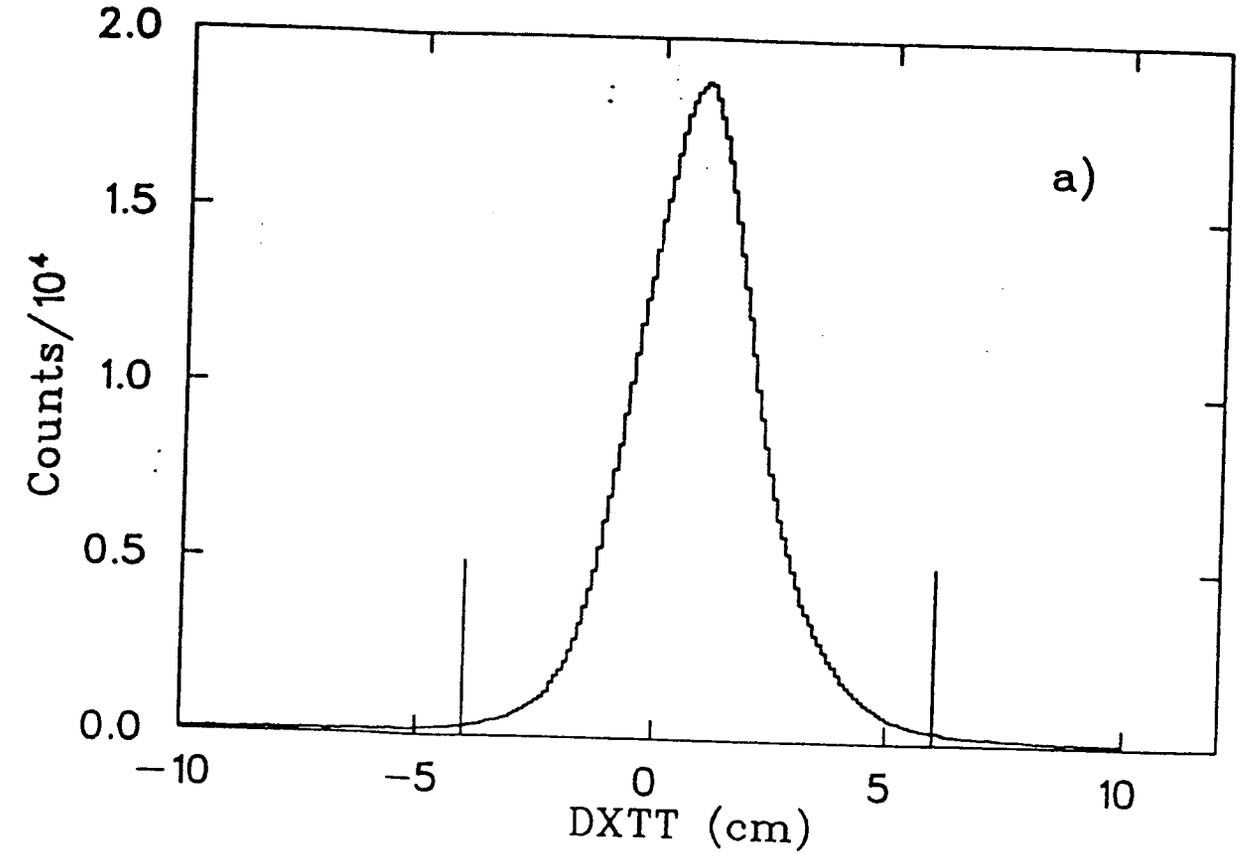
2.0
1.5
1.0
0.5
0.0
Counts/10⁴
a)
−10
−5
0
5
10
DXTT (cm)

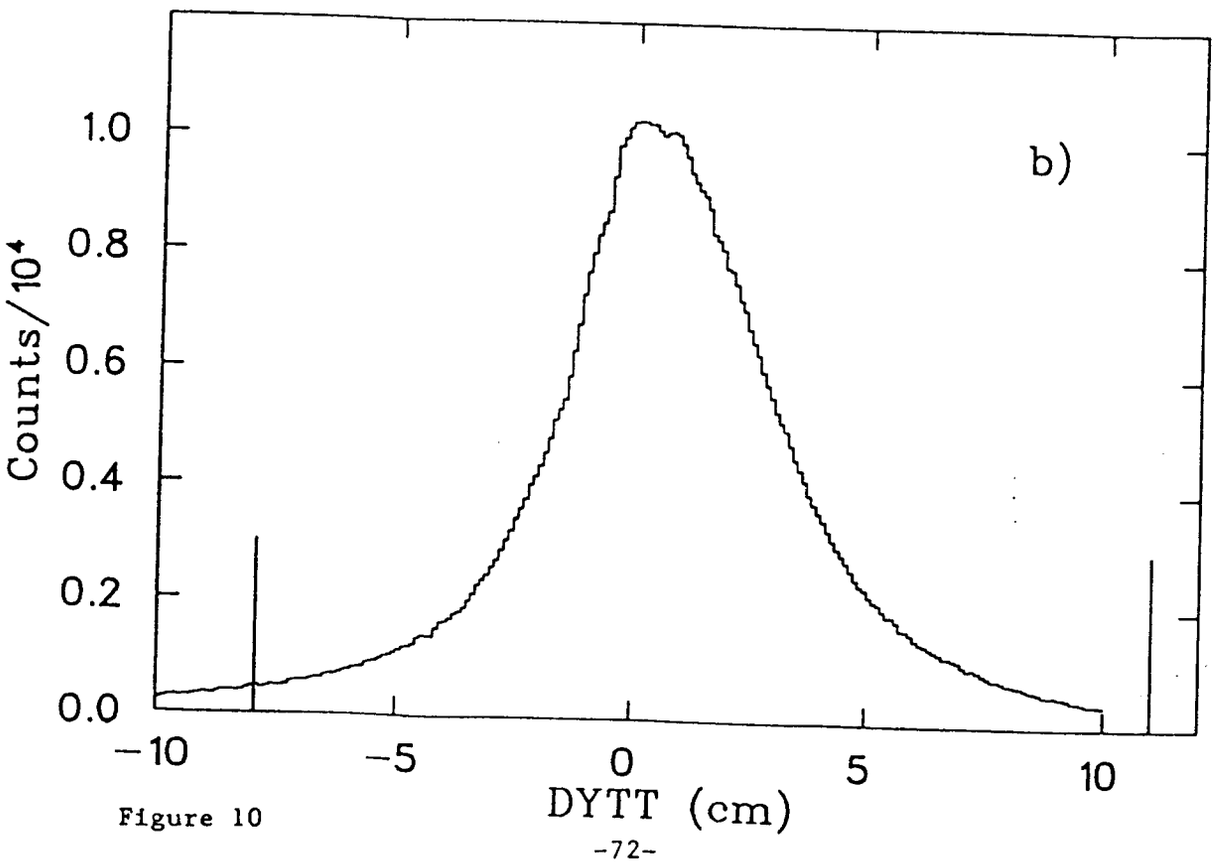
1.0
0.8
0.6
0.4
0.2
0.0
Counts/10⁴
b)
−10
−5
0
5
10
DYTT (cm)

Figure 10

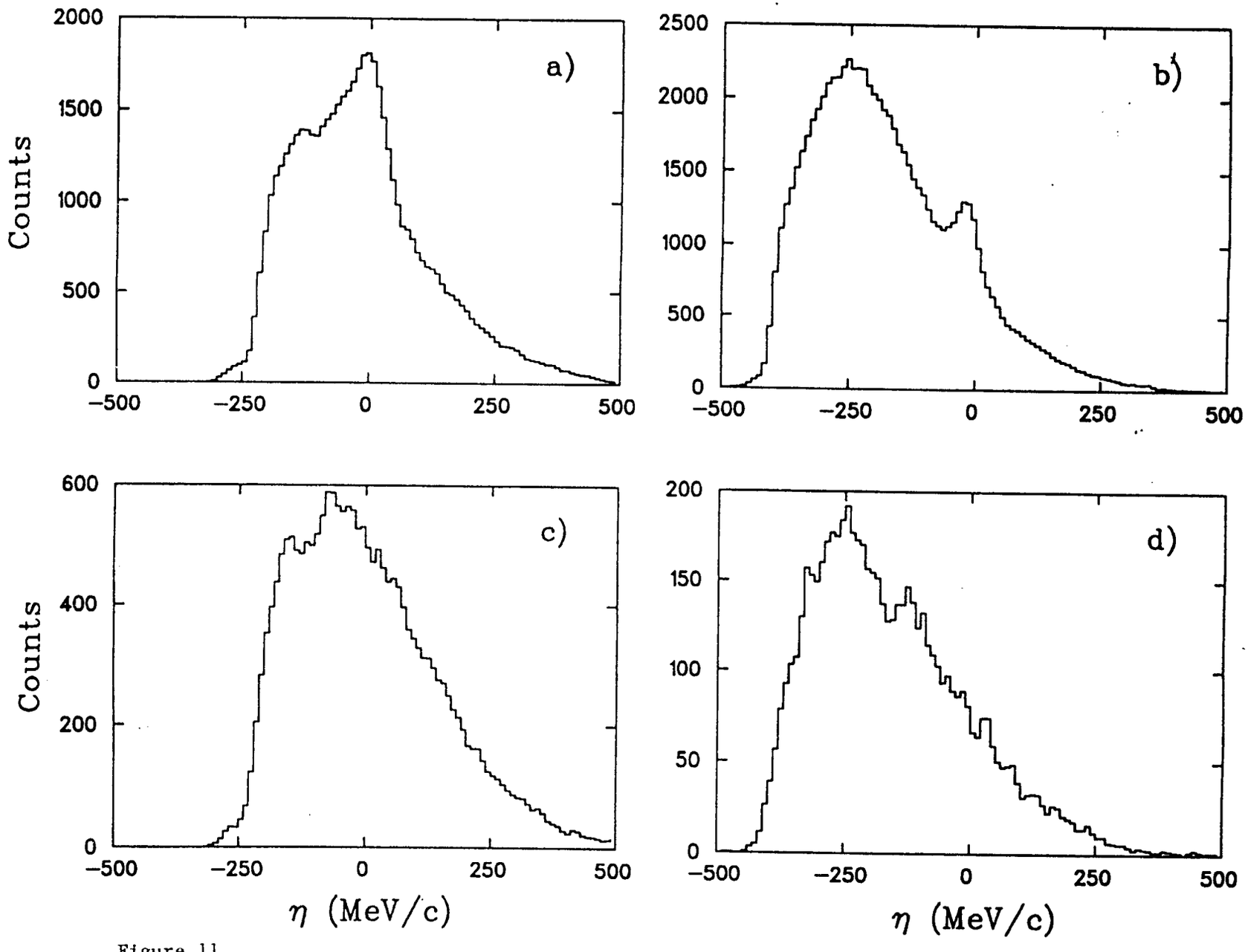
a)
b)
c)
d)
Counts
Counts
η (MeV/c)
η (MeV/c)
2000
1500
1000
500
0
2500
600
400
200
150
100
50
−500
−250
0
250
500

Figure 11

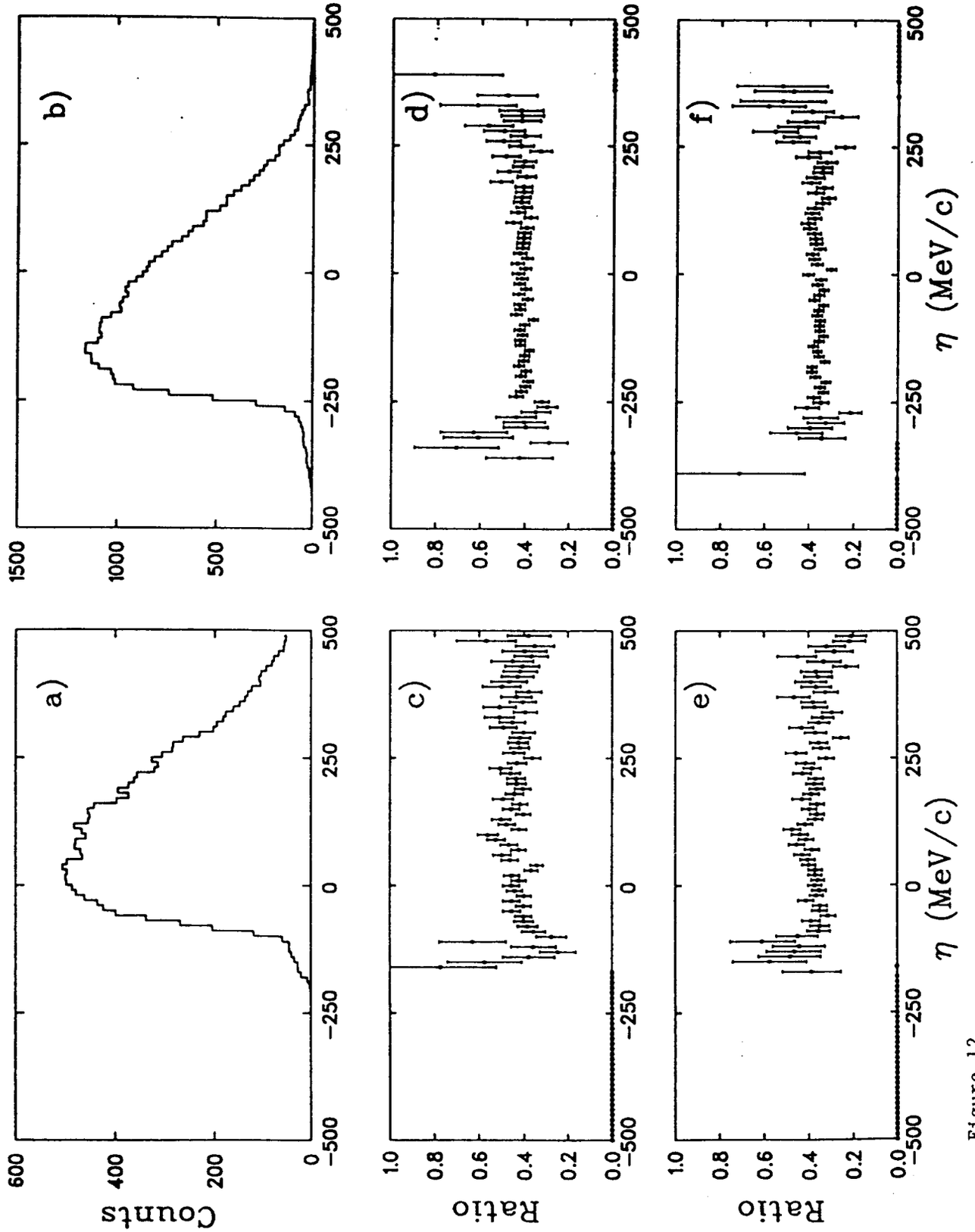

Figure 12

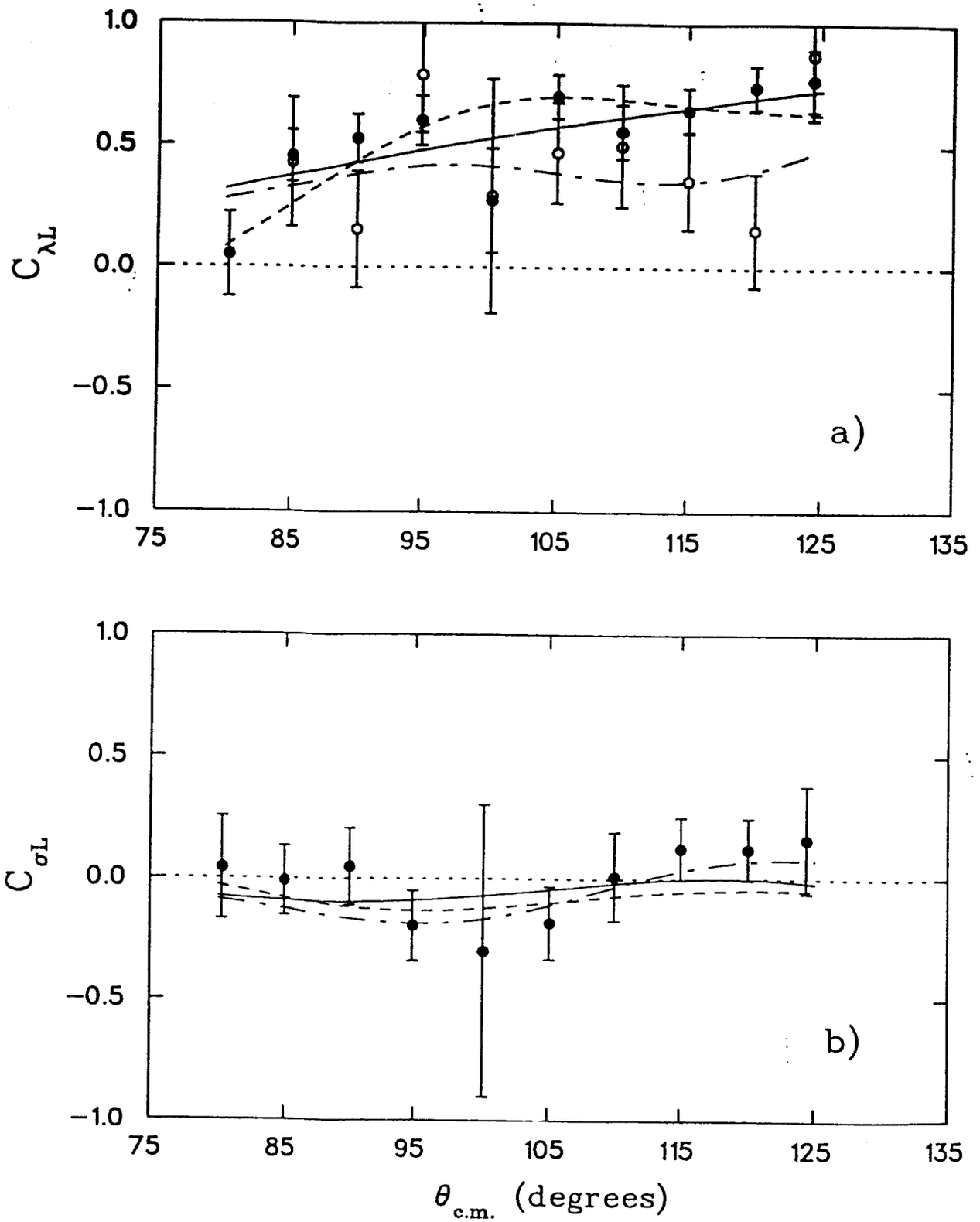
1.0
0.5
0.0
−0.5
−1.0
$C_{\lambda L}$
a)
75
85
95
105
115
125
135
1.0
0.5
0.0
−0.5
−1.0
$C_{\sigma L}$
b)
75
85
95
105
115
125
135
$\theta_{c.m.}$ (degrees)

Figure 13

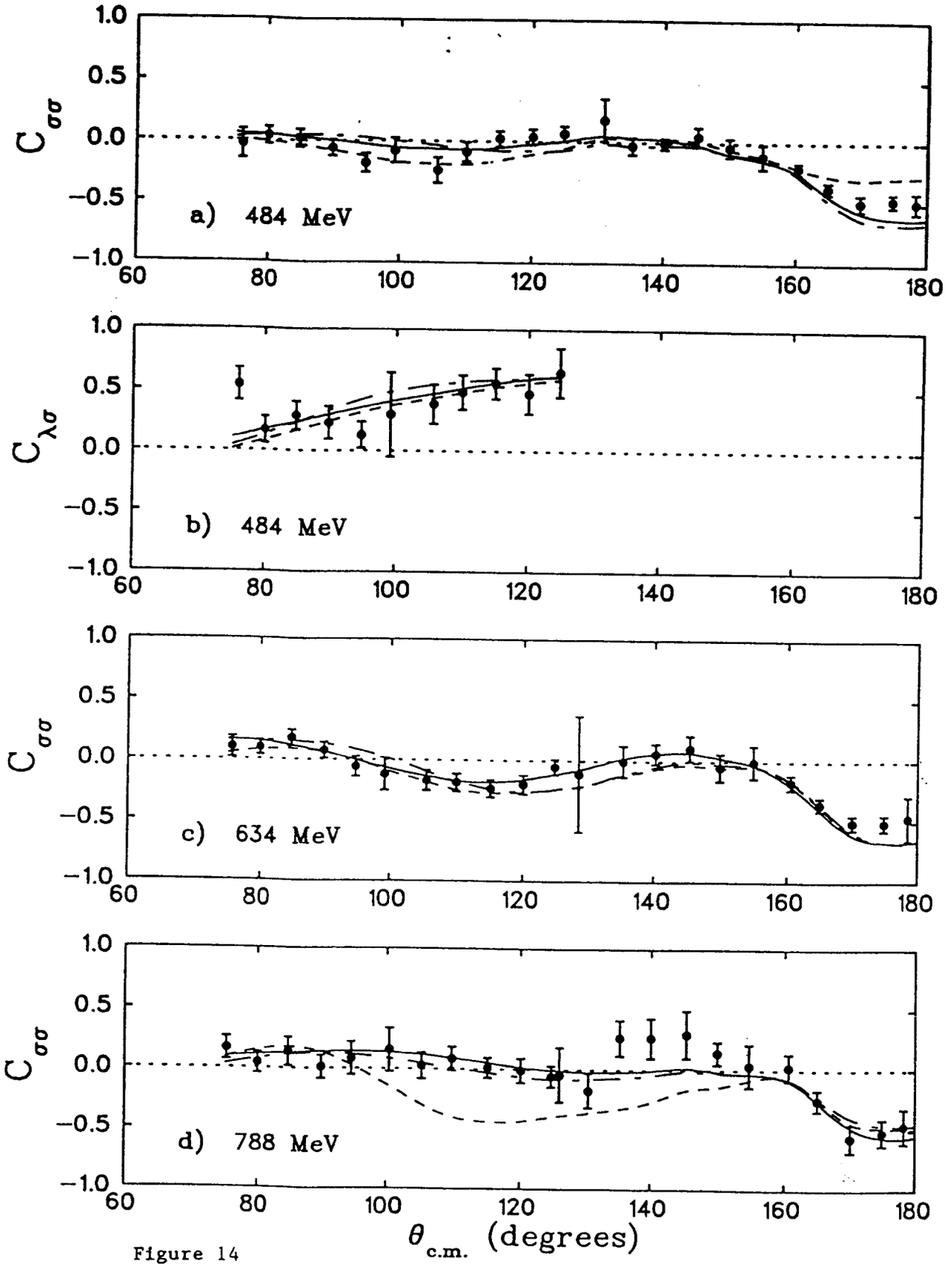
1.0
0.5
0.0
−0.5
−1.0
$C_{\sigma\sigma}$
a) 484 MeV
$C_{\lambda\sigma}$
b) 484 MeV
$C_{\sigma\sigma}$
c) 634 MeV
$C_{\sigma\sigma}$
d) 788 MeV
60
80
100
120
140
160
180
$\theta_{c.m.}$ (degrees)

Figure 14

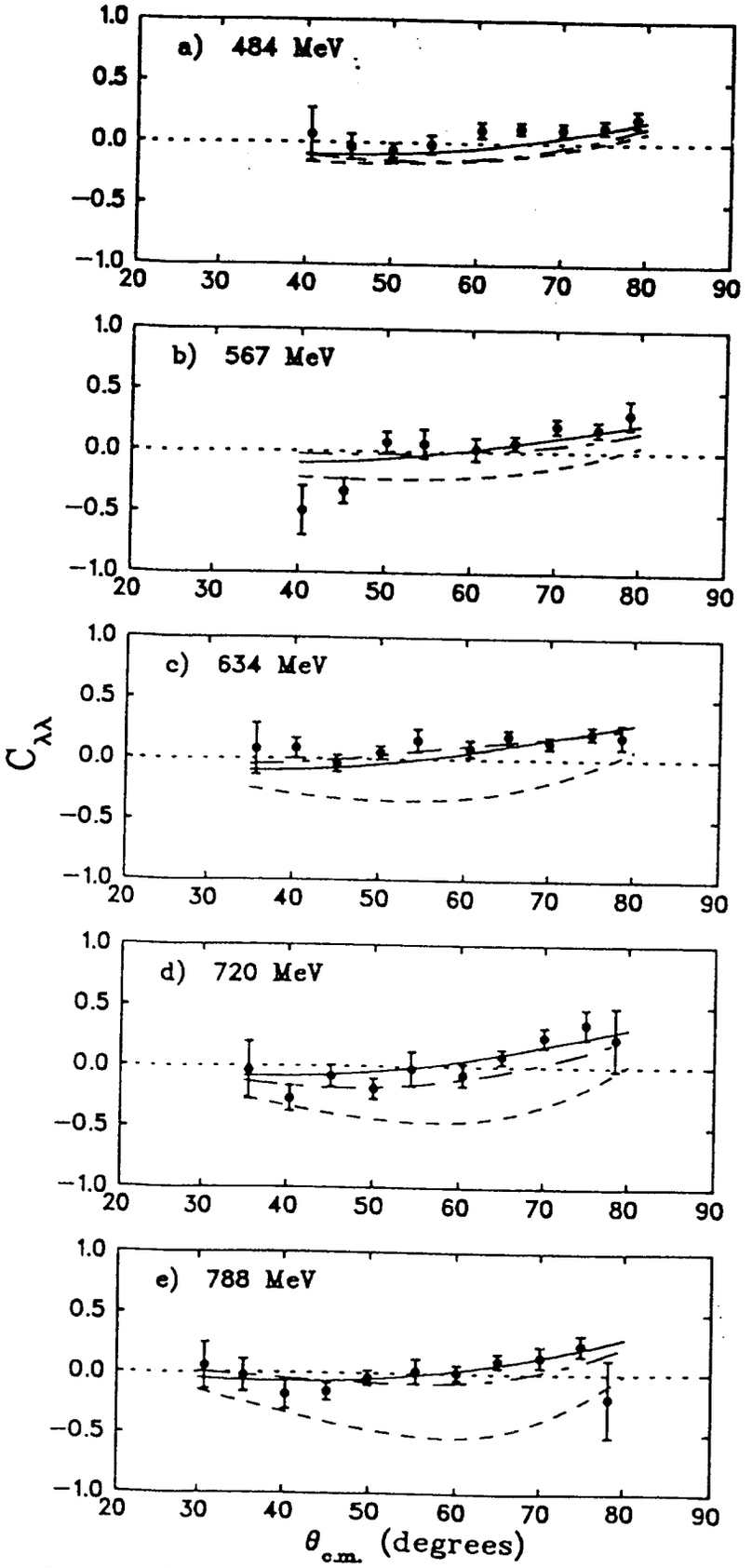
a) 484 MeV
b) 567 MeV
c) 634 MeV
d) 720 MeV
e) 788 MeV
$C_{\lambda\lambda}$
$\theta_{c.m.}$ (degrees)

Figure 15

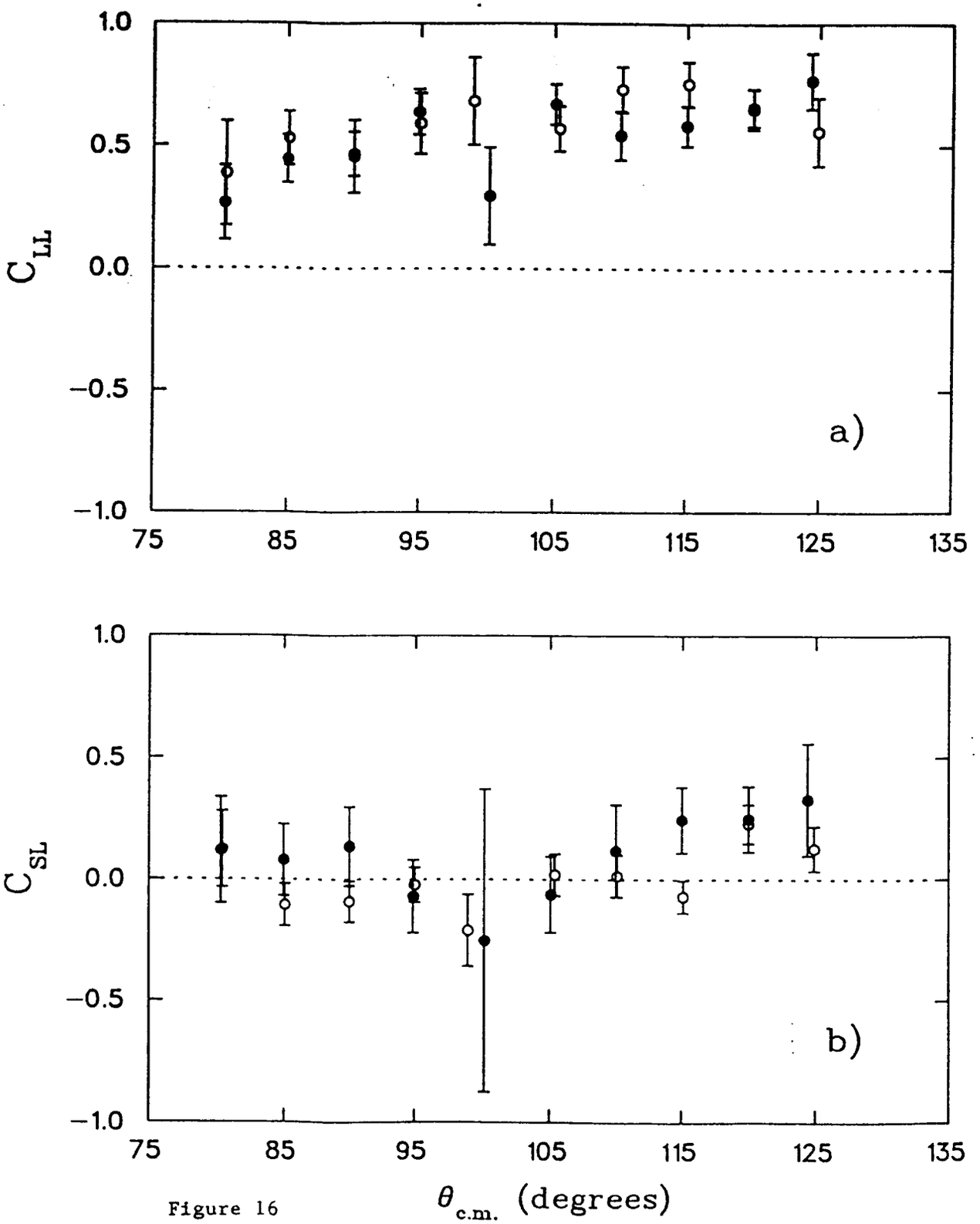
1.0
0.5
0.0
−0.5
−1.0
C_{LL}
a)
75
85
95
105
115
125
135
1.0
0.5
0.0
−0.5
−1.0
C_{SL}
b)
75
85
95
105
115
125
135
$\theta_{c.m.}$ (degrees)

Figure 16

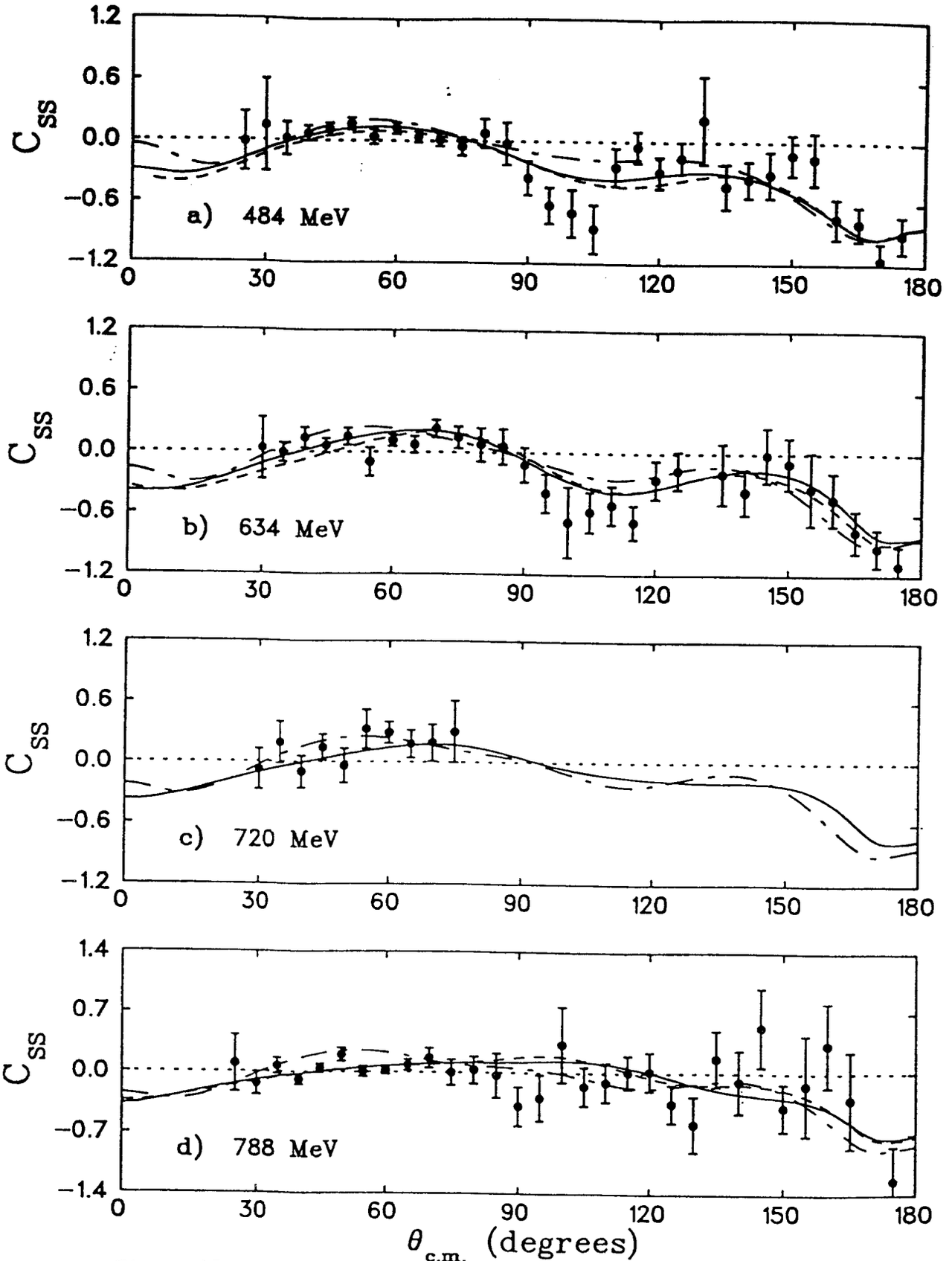
1.2
0.6
0.0
−0.6
−1.2
C_{ss}
a) 484 MeV
b) 634 MeV
c) 720 MeV
1.4
0.7
−0.7
−1.4
d) 788 MeV
0
30
60
90
120
150
180
$\theta_{c.m.}$ (degrees)

Figure 17

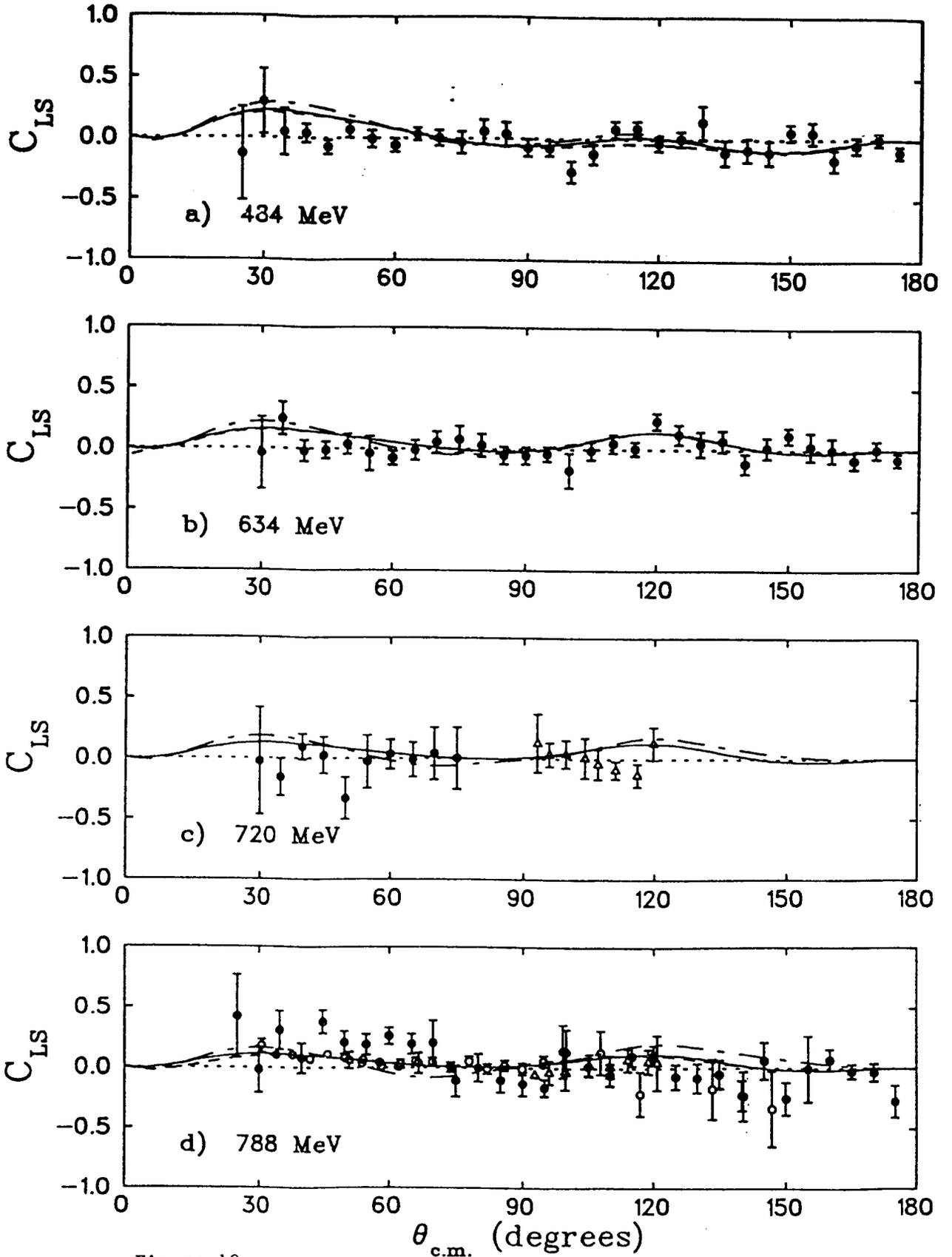
1.0
0.5
0.0
−0.5
−1.0
C_{LS}
a) 434 MeV
b) 634 MeV
c) 720 MeV
d) 788 MeV
0
30
60
90
120
150
180
$\theta_{c.m.}$ (degrees)

Figure 18

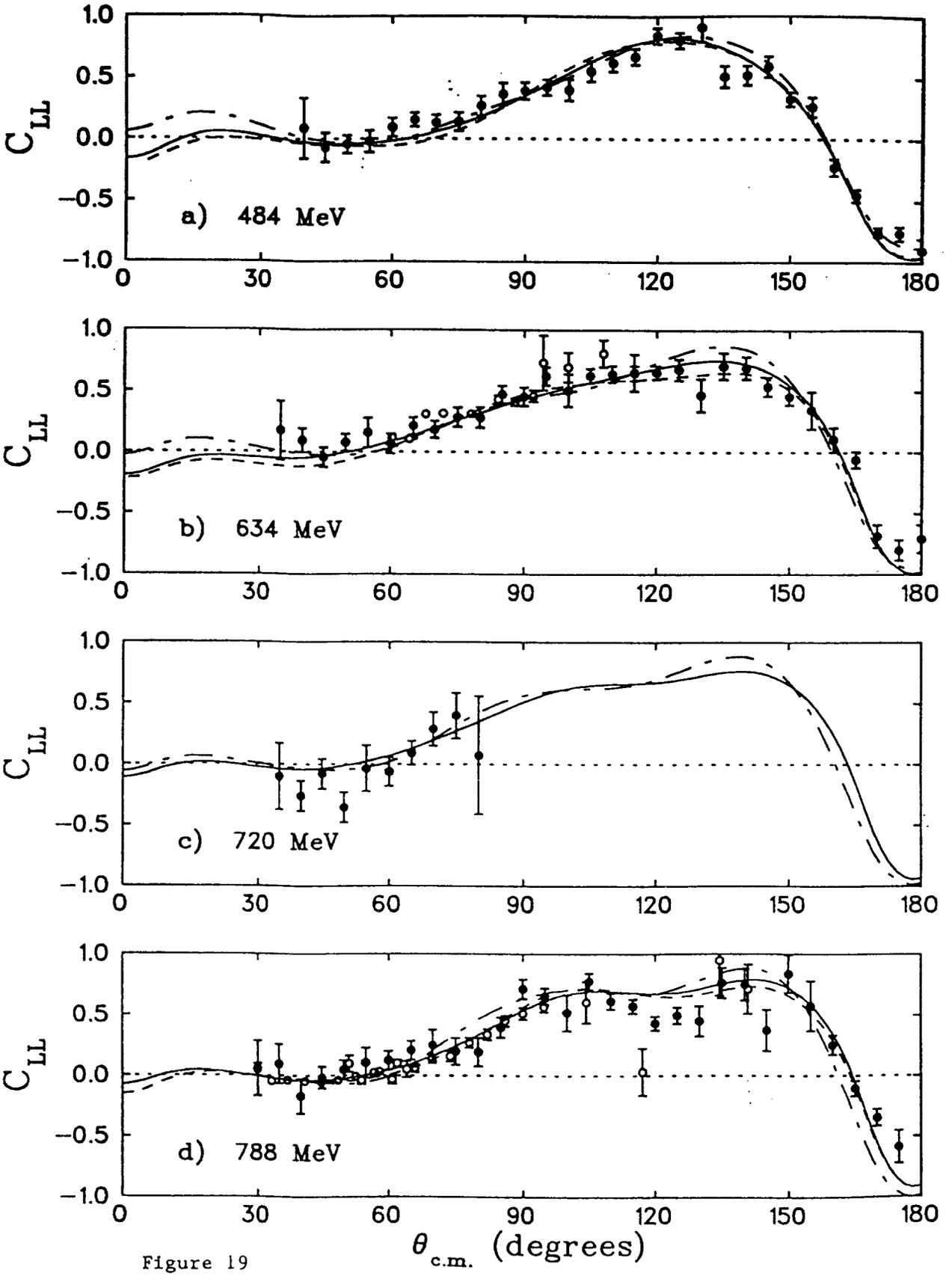
1.0
0.5
0.0
−0.5
−1.0
C_{LL}
a) 484 MeV
b) 634 MeV
c) 720 MeV
d) 788 MeV
0
30
60
90
120
150
180
$\theta_{c.m.}$ (degrees)

Figure 19

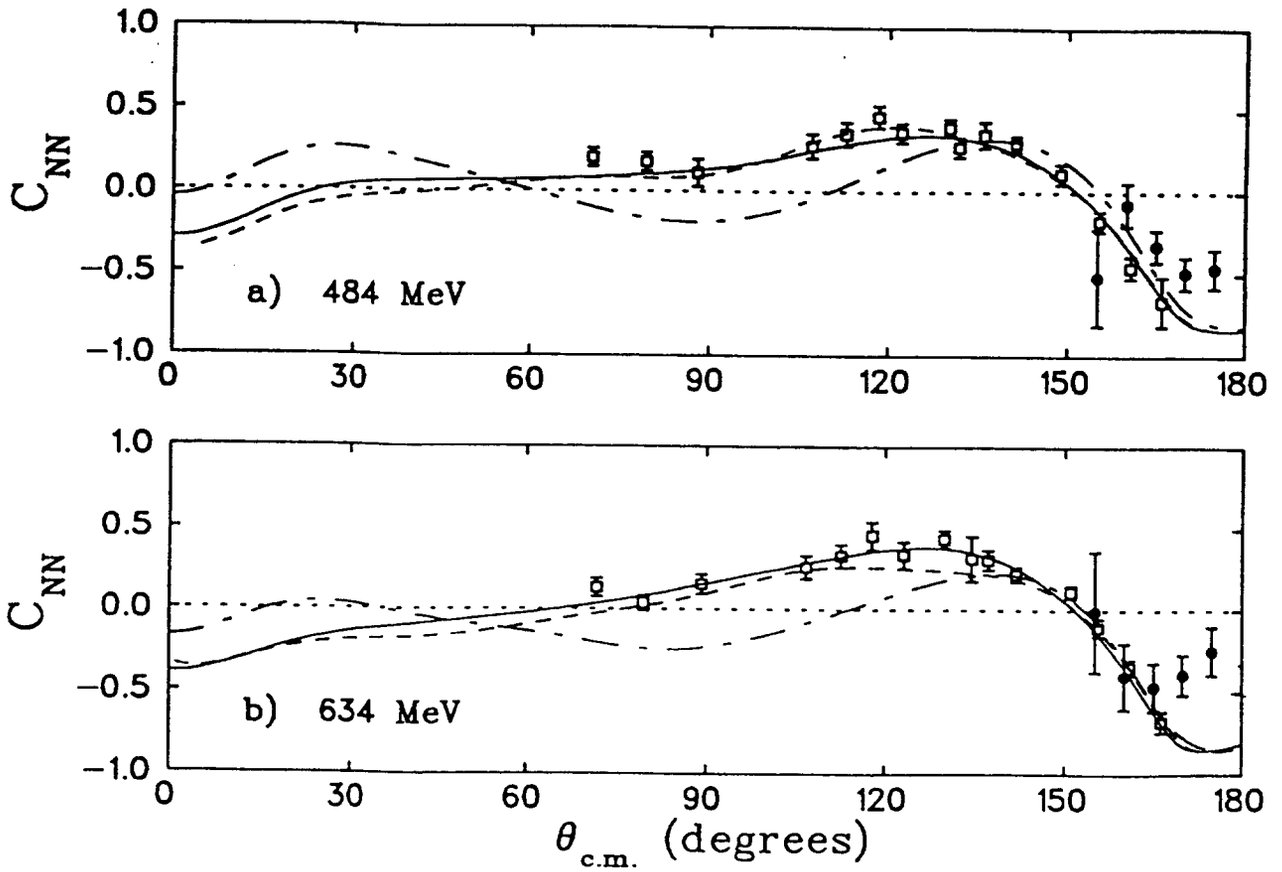
1.0
0.5
0.0
−0.5
−1.0
C_{NN}
a) 484 MeV
0
30
60
90
120
150
180
b) 634 MeV
$\theta_{c.m.}$ (degrees)

Figure 20

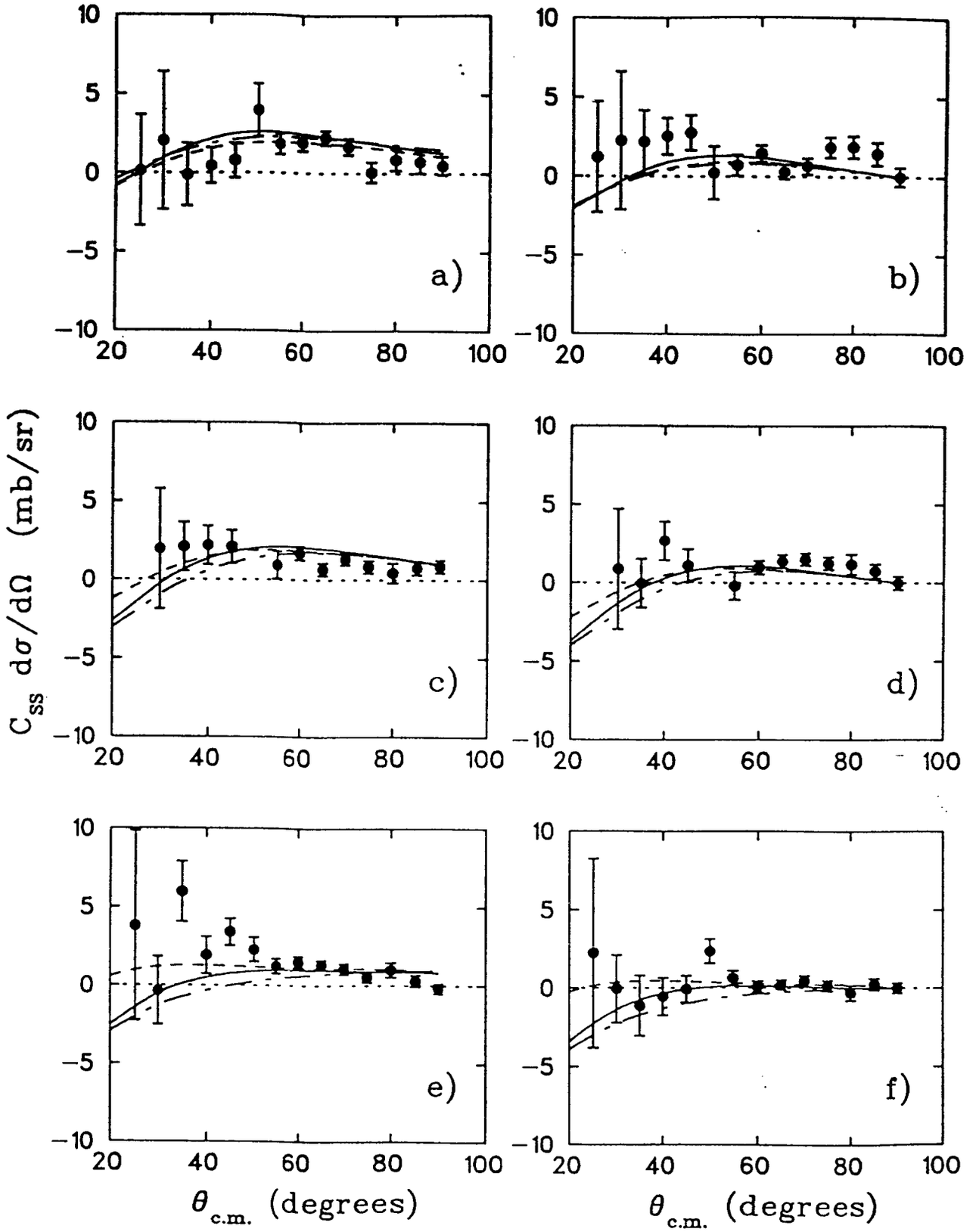
a)
b)
c)
d)
e)
f)
$C_{ss}\ d\sigma/d\Omega$ (mb/sr)
$\theta_{c.m.}$ (degrees)
$\theta_{c.m.}$ (degrees)

Figure 21

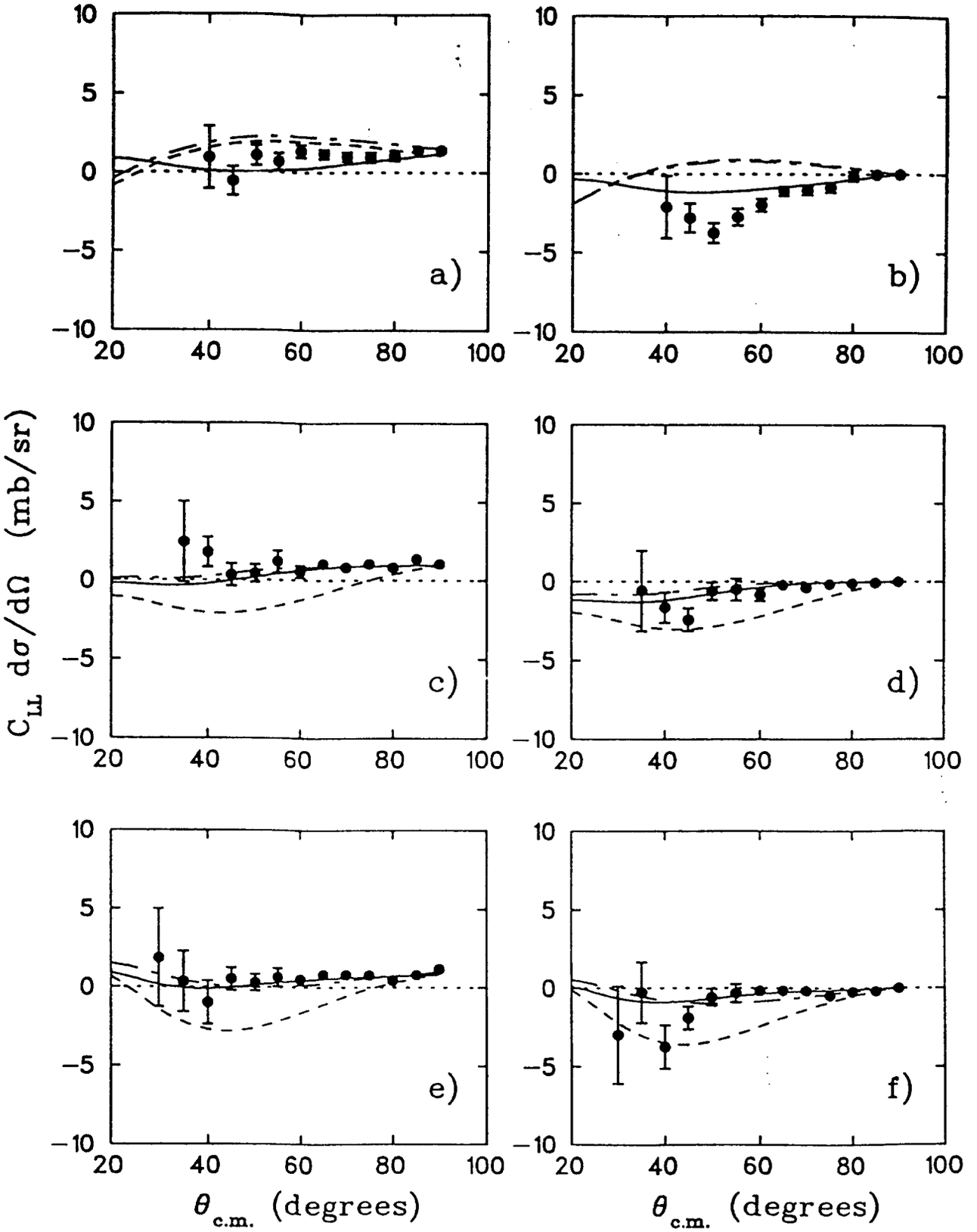

Figure 22

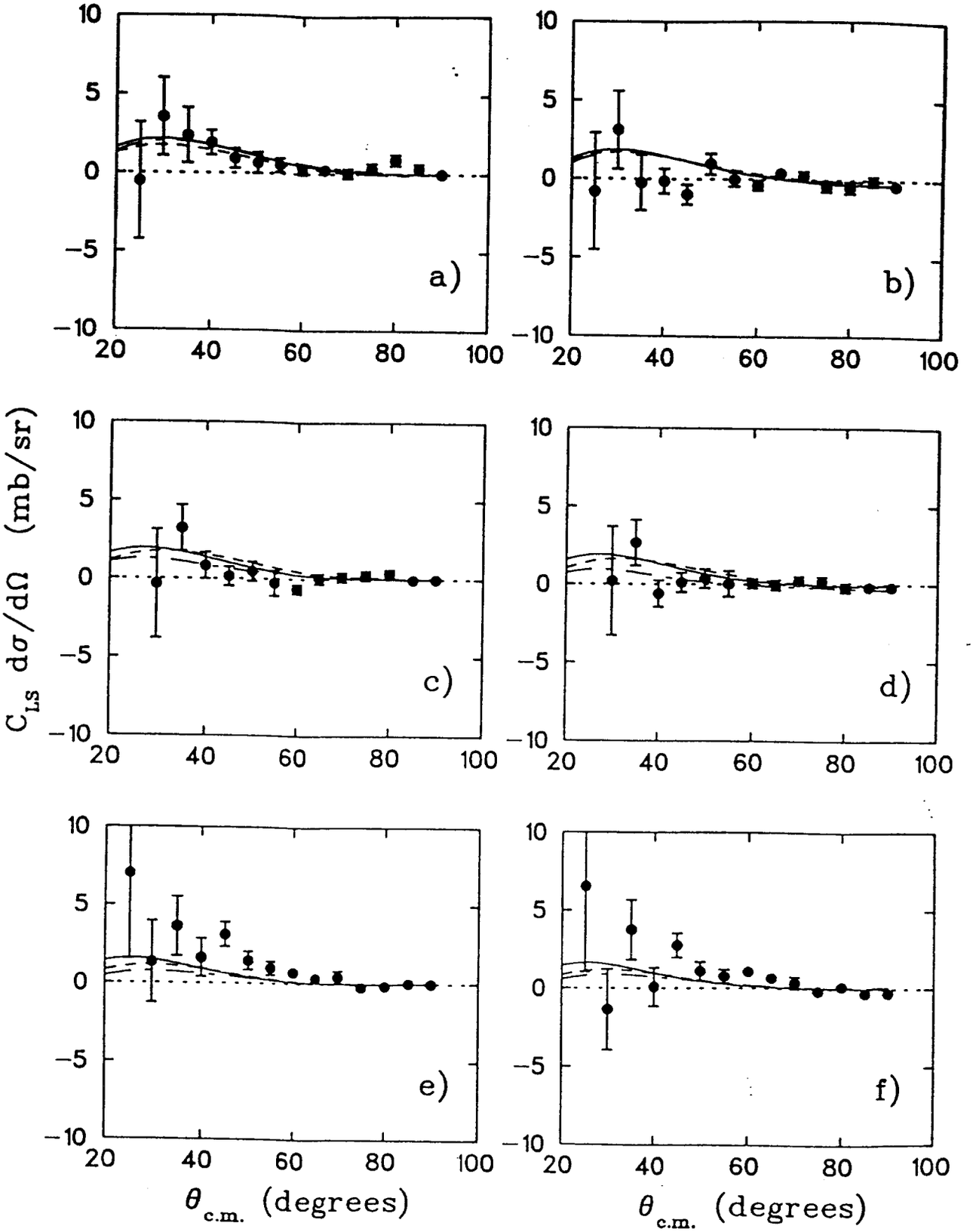
a)
b)
c)
d)
e)
f)
$C_{LS}\ d\sigma/d\Omega$ (mb/sr)
$\theta_{c.m.}$ (degrees)
$\theta_{c.m.}$ (degrees)

Figure 23

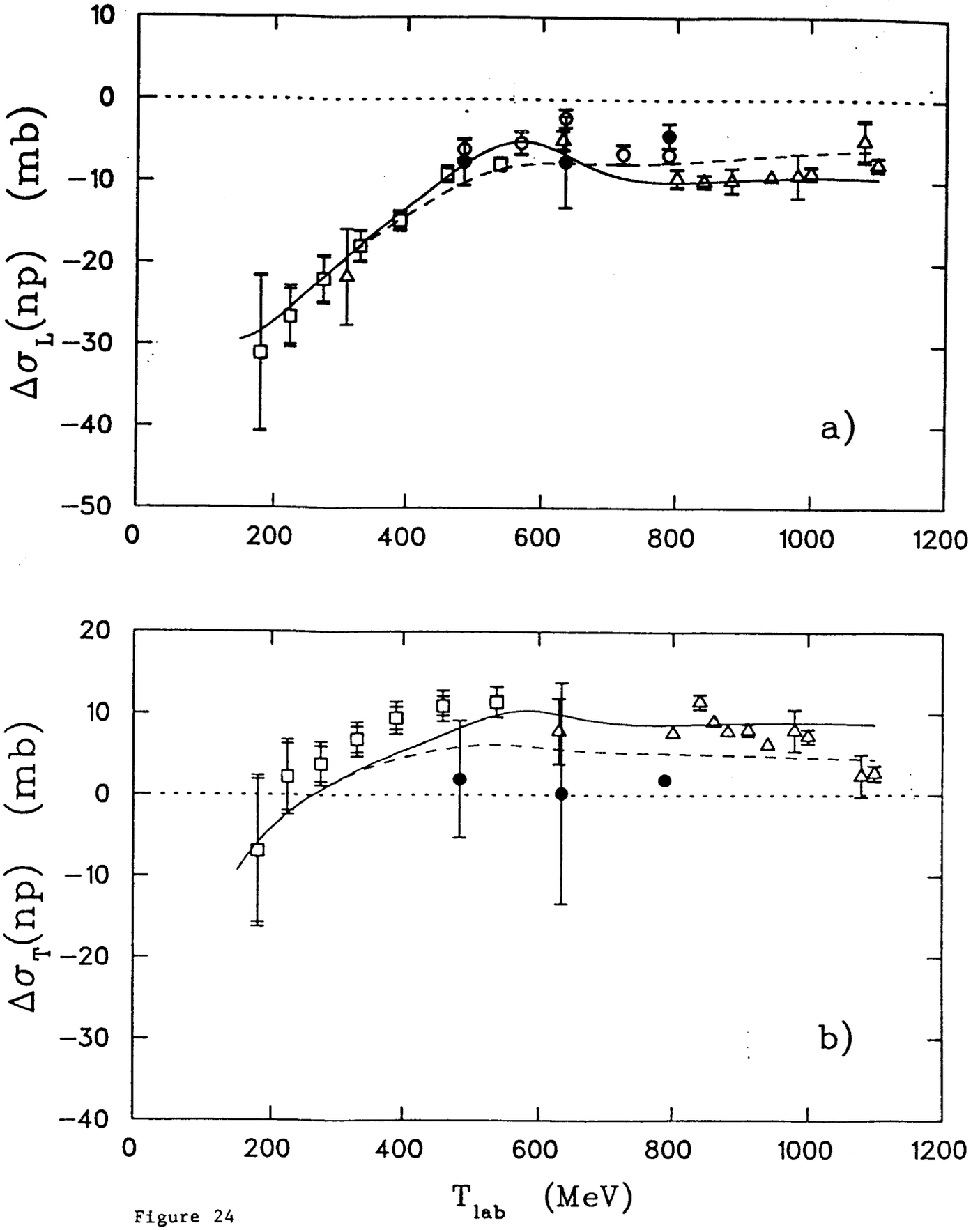
10
0
−10
−20
−30
−40
−50
$\Delta\sigma_L$(np) (mb)
a)
0
200
400
600
800
1000
1200
20
10
0
−10
−20
−30
−40
$\Delta\sigma_T$(np) (mb)
b)
T_{lab} (MeV)

Figure 24

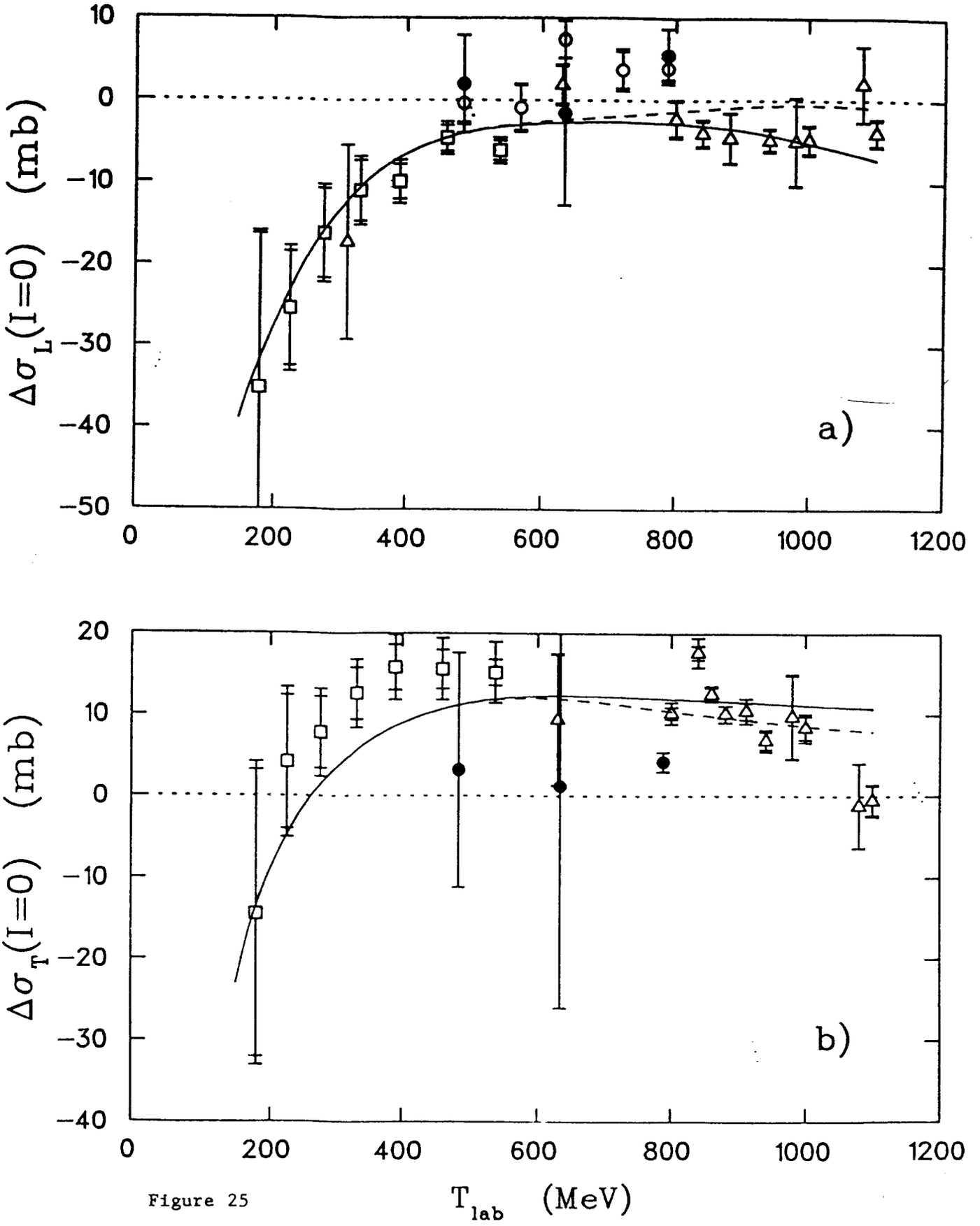
10
0
−10
−20
−30
−40
−50
$\Delta\sigma_L(I=0)$ (mb)
a)
0
200
400
600
800
1000
1200
20
10
0
−10
−20
−30
−40
$\Delta\sigma_T(I=0)$ (mb)
b)
T_{lab} (MeV)

Figure 25